Spring 1-1-2014

Enhancing Phase-Change Heat Transfer with Copper Nanowire-Structured Surfaces

Qian li
University of Colorado at Boulder, qian.li@colorado.edu

Recommended Citation

li, Qian, "Enhancing Phase-Change Heat Transfer with Copper Nanowire-Structured Surfaces" (2014). *Mechanical Engineering Graduate Theses & Dissertations*. 93.
https://scholar.colorado.edu/mcen_gradetds/93

ENHANCING PHASE-CHANGE HEAT TRANSFER WITH COPPER NANOWIRE-STRUCTURED SURFACES

by

QIAN LI

B.S., University of Science and Technology of China, 2006

M.S., Institute of Engineering Thermophysics, Chinese Academy of Sciences, 2009

A thesis submitted to the
Faculty of the Graduate School of the
University of Colorado in partial fulfillment
of the requirement for the degree of
Doctor of Philosophy
Department of Mechanical Engineering
2014

This thesis entitled:

Enhancing Phase-Change Heat Transfer with Copper Nanowire-Structured Surfaces

written by Qian Li

has been approved for the Department of Mechanical Engineering

____

Ronggui Yang

____

Yung-Cheng Lee

Date_______________

The final copy of this thesis has been examined by the signatories, and we
Find that both the content and the form meet acceptable presentation standards
Of scholarly work in the above mentioned discipline.

Qian Li (Ph. D., Mechanical Engineering)

Enhancing Phase-Change Heat Transfer with Copper Nanowire-Structured Surfaces

Thesis directed by Associate Professor Ronggui Yang

As energy consumption drastically increases in the electronics and energy conversion systems, heat dissipation becomes increasingly important for device reliability and system efficiency. Phase change heat transfer, which takes advantage of the latent heat during the phase change process, is the most promising method to efficiently remove high heat fluxes. Nano structures, which provide extended surface areas and enhanced hydrophilicity or hydrophobicity have been widely used in phase change heat transfer enhancement. Copper nanowires are one of the most promising nano structures due to ease of fabrication, controllable structure dimensions, and high thermal conductivity. In this study, the heat transfer performance of pool boiling, dropwise condensation, and evaporation in thermal ground planes (TGP) have been studied experimentally and theoretically on copper nanowire-structured surfaces.

The dropwise condensation heat transfer performance has been greatly enhanced under a subcooling range of ~ 15 K. Delay of Wenzel state droplets, a droplet state that negatively affects heat transfer, was achieved using hydrophobic nanowired surfaces. The solid fraction has been identified as the key factor to delay the occurrence of Wenzel state droplets. Surface energy conservation has been employed to explain the effect of the solid fraction on the coalescence induced jumping behavior and suggest the optimum structure for extended performance enhancement.

A critical heat flux (CHF) of 250 W/cm^2 has been realized on a hierarchical micropillar-nanowire structured surface under pool boiling. A force analysis on the liquid-vapor interface of a bubble incorporating the effect of liquid spreading has been used to illustrate how the liquid spreading helped to stabilize the bubble interface against the moment resulted from the vaporization process, so as to improve the CHF on structured surfaces.

A 200W/cm^2 maximum heat flux was realized in a TGP equipped with a patterned Cu nanowire array wicking structure. The ratio between the permeability and the effective pore radius of the wicking structures has been obtained and used to predict the maximum heat flux. The well agreement between the experimental and predicted data shows that the superior wicking performance is important for high maximum heat flux and the patterned nanowire array has the potential to further improve the maximum heat flux.

Five video files are provided as supplementary materials to this dissertation. Video1 is the dropwise condensation on smooth surface while Video2, Video3, Video4, and Video5 are dropwise condensation under different subcoolings on nanowired surfaces.

Acknowledgements

Firstly, I want to thank my advisor Prof. Ronggui Yang who makes my study here possible.

I must thank Prof. YC Lee for his help to my PhD life in Boulder. I learnt a lot from the discussions we had on my study and my situation.

I also thank the rest of my committee members: Prof. Yifu Ding, Prof. Julie Steinbrenner, and Prof. Kurt Maute.

Many thanks to my former and current group members who have helped me a lot to my study and my life. I want to thank Dr. Wei Wang, Dr. Miao Tian, and Dr. Dan Li. Without your help I couldn’t fabricate copper nanowire which is the key to my study. I also want to thank Dr. Jiafeng Wu for the countless minutes we talked through telephone on the condensation study.

Finally, thank you my family, especially my fiancée. Thank you for your company for the last couple of years. Thank you for sharing my happiness and my bitterness.

Contents

Tables

Figures

Chapter 1 Introduction

As energy consumption increases fast in the electronic and energy conversion industries, heat dissipation becomes a bottleneck of safe operation and further performance improvement. Enhanced heat transfer thus becomes important and receives world-wide interests. Phase change heat transfer which takes advantage of the high latent heat during the phase change process is the most promising method to remove high heat fluxes. Surface structures are effective to enhance the heat transfer performance in different phase change process such as pool boiling and condensation.

Surface structures provide more surface area for nucleation sites in the phase change process and enhance the hydrophilicity or hydrophobicity of the surfaces. What’s more important, the surface structures provide more methods to manipulate the movements of the three phase contact line such as the spreading speed of liquid on a heated surface and the shrinking of the contact line of a droplet on a cooled surface. Micro scale structures have been proved to be effective to enhance boiling heat transfer and inefficient to enhance condensation heat transfer. The liquid feeding to the nucleation sites is more effective with micro scale surface structures in pool boiling heat transfer than that on a smooth surface. On the other hand, the existence of micro scale structures can’t provide fast liquid removal from the surface in condensation heat transfer and keep the droplets staying longer on the surfaces so that the heat transfer performance degrades. With the advance of the nanotechnology, a variety of nano scale structures on silicon and copper surfaces has been realized. The nano structures on the surfaces provide orders of magnitude more surface area than that on the micro structured surfaces. Therefore, more nucleate sites could exist on nano structured surfaces. The liquid feeding could be further improved with the nano structures on the surfaces due to the large capillary force generated by the nano spacing. Surfaces thus become superhydrophilic with contact angle close to zero. The nano structures on the surfaces make it possible for the droplets to stay in highly mobile Cassie state since the surface becomes superhydrophobic. The easy removal of the Cassie state droplets might enhance the condensation heat transfer. Copper nanowires are one of the most attractive nano structures in the field of enhanced heat transfer due to the easy fabrication process and the controllable surface parameters such as roughness and structure coverage. The high thermal conductivity reduces the thermal resistance resulted from the copper nanowires so that the extra temperature difference resulted from the nanowires can be neglected. Based on the nanowire structured surfaces, the heat transfer performance of pool boiling and dropwise condensation has been studied experimentally and theoretically in this research. Nanowire based wicking structures used in thermal ground planes have been studied as well in this research after studying the heat transfer performance of nanowired surfaces in pool boiling and dropwise condensation.

1.1 Dropwise condensation heat transfer enhancement

Vapor condensation on solid surfaces is a common phenomenon in the nature and widely used in the industries. When vapor condensation occurs on the solid surfaces, the condensate forms either a thin layer of liquid (filmwise condensation) or liquid droplets (dropwise condensation) depending on the wettability of the solid surfaces. Due to the high thermal resistance resulted from the liquid film in filmwise condensation, dropwise condensation is preferred in the industries. Dropwise condensation is realized by applying hydrophobic coatings to surfaces to lower the surface energy. The heat transfer performance is enhanced with refreshed surface area for re-nucleation by removing the liquid droplets at length scale comparable to the capillary length which is ~2.7 mm.[1] Traditional dropwise condensation relies heavily on gravity, which limits the applications of dropwise condensation. Enhanced dropwise condensation heat transfer is highly demanded in many areas such as power plant,[2] desalination,[3,4] refrigeration[5] and thermal management of electronics[6] for maintaining the temperature level, protecting thermal device, optimizing spaces and materials of condenser, or minimizing the waste in energy transfer. Solid-liquid interfaces need to be designed elaborately for dropwise condensation enhancement, on which the structural consideration has been put into nanoscale. Nanoscale structured surfaces exhibit many superior properties, such as enhanced hydrophobicity, increased nucleation site density, and extended surface area, which may benefit for condensation heat transfer enhancement. For this reason, researches of condensation on hydrophobic surfaces with nanotube, nanowire,[7,8,9,10,11] nanoparticle,[12,13,14]or micro/nano hybrid (two-tier) structures[15, 16, 17, 18] are widespread studied nowadays.

A droplet sitting on a hydrophobic nanostructured surface presents two kinds of wetting states, i.e. Cassie[19] state and Wenzel[20] state. A Cassie state droplet stands on the tip of nanostructures while the Wenzel state droplet totally infiltrates the nanostructured area. There exists a critical contact angle[21]

$$\cos\theta_c = \frac{\varphi - 1}{r - \varphi} \tag{1.1}$$

where, φ and r are the solid fraction and roughness factor of nanostructured surface. If the intrinsic contact angle θ is greater than θ_c, the droplet appears in Cassie state. Otherwise, it appears in Wenzel state. A droplet has a steady wetting state, Cassie or Wenzel, on a certain hydrophobic material surface with nanostructures under non-condensation condition, which keeps the droplet in minimum surface energy. Although both of the wetting states can increase the droplet apparent contact angle compared with that on the smooth surface with the same hydrophobic coating,[22,23] Cassie state droplet always has a smaller contact area for droplet removal, which might be more beneficial for condensation heat transfer.

Chen *et al*.[15] observed that condensate can jump off from a two-tire-roughness hydrophobic surface after the coalescence of two Cassie state droplets. The scale of the two Cassie state droplets can be as small as 10 μm which is more than two orders of magnitude smaller than the capillary length at 2.7 mm. If this spontaneous condensate removal could be stably realized, it will greatly benefit the dropwise condensation heat transfer enhancement due to the fast condensate removal and the newly exposed dry area for re-nucleation.

Wang *et al.*[24] enhanced the heat transfer performance with the coalescence induced jumping condensation on the outer surface of a copper oxide nanostructured copper tube. They also pointed out that other than Wenzel and Cassie states there was a third wetting state of the droplets which is the partially-wetting Cassie state.[11] The nanostructures under the droplets were not fully wetted. What's more important is that the heat transfer rate of partially-wetting Cassie state droplets is much better than that of the Cassie droplets and droplets on the smooth surface.

Although the coalescence induced jumping droplet removal has been realized, most of the nano/hierarchical structured surfaces still present worse dropwise condensation heat transfer performance than that on the smooth surface[13] or just enhance the heat transfer performance under limited subcooling range[24] due to the immersion of the nanostructures by the condensate under condensation condition.

Since the immersion of the structures or the appearance of Wenzel state droplets has been identified as the reason for the failure of the dropwise condensation heat transfer enhancement, the study of the droplet state change is needed to guide the design of the nanostructures. Exploration of the nanowire structured surfaces for dropwise condensation heat transfer enhancement is the purpose of this research. With the help of a high speed camera, the droplet states and the droplet removal manners have been recorded during the heat transfer experiments. The recording of the condensation process together with the heat transfer performance shows that carefully chosen nanowire structures can provide and reserve partially-wetting Cassie state under condensation conditions, so as to facilitate the droplet removal and enhance condensation heat transfer under extended subcooling range.

1.2 Pool boiling heat transfer enhancement

Pool boiling phase change heat transfer plays a critical role in a wide variety of applications including energy conversion and thermal management of data centers, electrical vehicles, and electronics.[25,26,27,28,29] Many techniques have been employed to improve the heat transfer coefficient (HTC) and the critical heat flux (CHF), the two key parameters that characterize the boiling heat transfer performance on a surface by modifying surface energy state through coatings [30,31] and changing the surface topology with nano-,[32,33,34,35] micro-,[36,37,38] and even larger-scale structures. The CHF is determined by fluid replenishment of vapor nucleation sites, which depends on the contact angle of the working fluid on the surface and the vapor-liquid counter flow above the heating surface,[39,40,41,42,43,] whereas the HTC is controlled by bubble dynamics.[44,45] Due to the capillary force generated by the structures on the surfaces, the vapor-liquid counter flow is no longer a limit.[46] Dhir and Liaw [40] illustrated that the CHF increases with the decrease of the contact angle. Kandlikar[47] developed a quantitative CHF model to describe this relation between contact angle and CHF. However, neither work could explain the fast CHF increase in the superhydrophilic regime (contact angle < 20°) nor the different CHFs on different surfaces whose contact angles are the same. Therefore, other factors influencing the CHF must exist. The heat flux in pool boiling heat transfer is closely related to the active nucleate site density [45,46, 48] and the heat transfer conditions at one active nucleate site.[49, 50] Although CHF is directly relate to the liquid replenishment to the nucleate site while HTC is directly related to liquid heating and evaporation process at the active nucleate site, most studies didn't study the influence of the liquid spreading speed on the surfaces, which is defined as how fast liquid can propagate due to the capillary force generated by the surface structures, on CHF and HTC, especially when artificial structures existed.

On one hand, the CHF is directly related to the liquid spreading within the surface structures since the CHF is determined by the replenishment of the active nucleate site, which is confirmed by the recent study from Ahn *et al.*[51] The liquid spreading within the surface structures in addition to the contact angle becomes important to determine the CHF. However, the fundamental effect of the liquid spreading on CHF has been explained. Besides, the CHF predicted by the model matched the experiment data well only when the contact angles were smaller than 10°. On the other hand, the HTC is also directly related to the liquid spreading within the surface structures since the evaporation rate and the liquid heating process is directly related to the liquid spreading on the surface.[49, 50, 52] In this study, the pool boiling heat transfer performance of a series of samples with contact angle ranging from ~ 0° to ~ 20° was tested to figure out the effect of liquid spreading speed on CHF and HTC. The CHF model based on the force analysis on the vapor-liquid interface of a bubble and heat flux-superheat relation including liquid spreading effect were built to compare with the experiment data.

1.3 Thermal ground plane heat transfer enhancement

Various strategies have been employed and developed to remove this high heat flux including: heat spreading materials, refrigeration, solid-state cooling, and liquid cooling.[53] Heat pipe which is a phase change device has been regarded as an excellent heat removal solution and used in cooling electronic devices.

Conventional heat pipe is a sealed tube with wicking structures on the inner wall and working liquid inside. When heated at the evaporator, the working liquid will vaporize and extract heat from the heat source and then the vapor will transfer to the condenser. After rejecting heat and returning to liquid state at the condenser, the working liquid is drawn back to the evaporator by the capillary force generated by the wicking structure. Although heat pipes have wide applications in energy conversion, aerospace, electronics and so on,[54] connector between the heat pipes and the heating components is needed due to the tubular shape. Flat shaped heat pipe is therefore desired. Thermal ground plane (TGP) is such kind of flat shaped heat pipe. The flat shape makes it compatible to manufacture with IC process, easy to integrate into the electronic systems and effective to reduce contact thermal resistance.

The number of transistors on the chip doubles every 18 month[55] and the power consumed by the LED increases fast. Heat generated from a high performance CPU and an array of LED illustrator exceed 100W/cm^2 [56,57] and 1000W/cm^2 [58,59] while the temperature of the electronic devices needed to be controlled under 85 ^{0}C [99] and 120 ^{0}C, [58, 99] respectively. The miniaturization of the electronic devices drives the development of compact TGPs. [60] The thickness of nowadays' TGP falls into a range of sub millimeter to several millimeters.[61,62,63,64] Thus, there is a great need for developing small size TGPs with ultrahigh heat flux removal capability.

The TGPs work the same way as heat pipes and the performance is limited by the wicking structure. Great effort has been devoted. Peterson and his co-workers[65] comprehensively studied micro-grooved wicking structures. This type of wicking structure provides high total heat transport capability and low temperature difference across the heat pipe. However, the one-dimensional liquid flow which increases the pressure loss limits the maximum heat flux. Porous media including sintered metal powder and metal meshes are also popular wicking structures[63,66,67] that provide high capillary force to overcome the pressure loss during vapor and liquid transport. Therefore, TGPs with this type of wicking structures can reach very high heat flux before dry-out.

But since the powder or the mesh is of 100 μm size and the wicking structures are usually made of multi-layer, the total thickness of the wicking structure is large. This limits the use of porous media in very compact systems. To realize ultrahigh heat flux removal capability with a compact device, a new type of wicking structure needs to be developed.

Due to the advance of nanotechnology nano-structures have been employed in making wicking structures. Li[33] and Chen[35] investigated pool boiling performance on uniform Cu nanorods and Cu/Si nanowires coated surfaces and found that the phase change heat transfer was greatly enhanced. However, the flow resistance within the uniform nanowire arrays is too large to be used as wicking structure. Cai[68] studied evaporation on patterned CNT arrays and reached extremely high maximum heat flux in large vapor chamber. But the one-dimensional pattern limits its application. Nam[69,70] studied the wicking and heat transfer performance on superhydrophilic nano-structured Cu micro-posts wicking structure. This two-dimensional wicking structure reached 1000 W/cm^2 heat flux when dry-out occurred in large vapor chamber. However, the solid micro-posts provide limited evaporation enhancement.

A novel patterned Cu nanowire array wicking structure with square nanowire bundles and micro-scale gaps will be fabricated and tested in the present study. The square nanowire bundles will generate large capillary force and provide numerous surface areas while the micro-scale gaps will lower the flow resistance on the structure.

Chapter 2 Sample Fabrications

The structures studied in this research include copper micro-pillars, uniform copper nanowires with and without hydrophobic self-assembled-monolayer (SAM) coating, copper micropillar/nanowire hierarchical structure, and copper patterned nanowire arrays.

2. 1 Fabrication of the copper micropillars

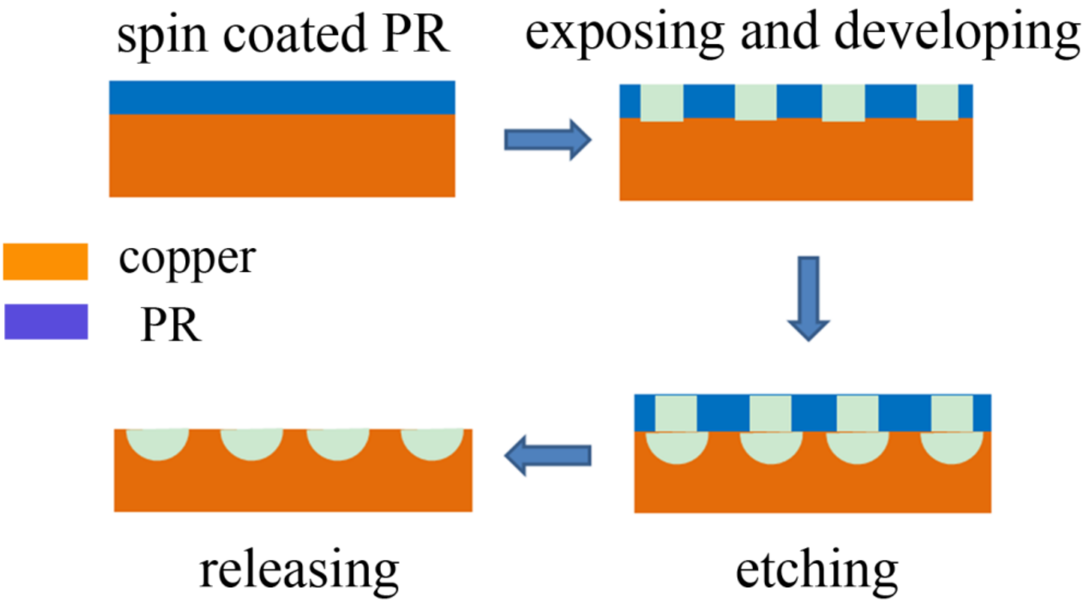

Figure 2. 1 Fabrication process of micropillars

The copper micropillars are fabricated by a standard photolithography and wet-etching process. A 0.8mm thick oxygen free Cu sheet (99.99% copper) was firstly wet polished by 1200/2000 grit sandpapers which results in a roughness of 450 nm. The majority of the scratches were removed although some dents might be left. After cleaning the surface with DI water and 2 % H_2SO_4 solution, photoresist (AZP4620) was then spin coated onto the Cu sheets and prebaked at 110 °C for 85 seconds on a precise hot plate. Two different 4 in × 4 in × 0.06 in Chrome on Sodalime Lithography masks were used to define the periodic pattern of the micropillars. The first mask has quadratically arranged squares with a size of 50 μm × 50 μm and a pitch of 100 μm. The second mask has quadratically arranged squares with a size of 100 μm × 100 μm and a pitch of 200 μm. The pillar coverage of both masks is 25%. After exposure under a mercury lamp for 60 seconds, the Cu sheets were immersed into AZ400K developing solution to remove the exposed photoresist. Then, the Cu sheets were dipped into the etchant (CE100) for 2 ~ 3 min to etch off the Cu. Due to the isotropic nature of wet etching the fabricated micropillared Cu surface using the mask with 50 μm × 50 μm squares at a pitch of 100 μm had a real micropillar dimension of 20 μm × 20 μm, while micropillared Cu surface using the mask with 100 μm × 100 μm squares at a pitch of 200 μm had a micropillar dimension of 45 μm × 45 μm. After releasing the photoresist with acetone, the micropillared surfaces were ready to be cut into 8 mm × 8 mm square to fit the heating bar. The process flow for fabricating the Cu micropillared surfaces is illustrated in Figure 2.1.

2.2 Fabrication of the uniform copper nanowires and the hydrophobic coating

Figure 2.2 shows the fabrication process for Cu surfaces with uniform Cu nanowires. The Cu surfaces with uniform Cu nanowires were fabricated using PAA template-assisted electroplating method.[71, 72] No matter copper bar or copper sheet was used, the surface had to be polished by 1200/2000 grit sandpapers first to guarantee a similar surface roughness as that of the smooth surface. Commercial PAA templates (Whatman, 6809-5522) whose porosity is ~25% - 50% were used as received, and the electrolyte solution for Cu electroplating consisted of 60 g/L cupric pyrophosphate ($Cu_2P_2O_7.xH_2O$; Sigma-Aldrich 34469-9), 250 g/L Potassium pyrophosphate ($K_4P_2O_7$; Sigma-Aldrich 322431-500G) and 20 g/L Ammonium citrate ($C_6H_{17}N_3O_7$, Fluka 09831). A two-step process was developed for the nanowire fabrication. The first step was to bond the PAA template onto the Cu substrate. As shown in Figure 2.2 (a), a sandwich structure was constructed by stacking the Cu substrate (target surface), a PAA template wetted by the electrolyte solution, a filter paper saturated with electrolyte solution and a counter electrode Cu sheet (oxygen free 99.99% copper) in sequence. Electrolyte solution was absorbed into the filter paper for Cu^{2+} ions supply during the electrodeposition process, and uniform pressure was provided continuously by a wide clamp bench vice to make the PAA template adhere tightly onto the Cu substrate. A constant voltage of -0.8 V was applied between the counter electrode (Cu substrate) and the Cu counter electrode for 15 minutes. During this process, Cu nanorods were grown on the Cu substrate into the nano holes in the PAA template to serve as screws that bond the PAA template to the Cu substrate. The Cu substrate together with the PAA template was then released from the sandwich structure after the bonding step. For the second electrodeposition process in Figure 2.2 (b), the Cu substrate with PAA template on top was placed in a 3-electrode electroplating cell in the electrolyte solution. Here, a constant voltage of -1 V compared with a reference electrode (Ag/AgCl) was applied to deposit the Cu nanowire arrays in the PAA templates. The length of the nanowires was controlled by the electroplating time. Then, the as-obtained Cu nanowire arrays were released from the PAA template by immersing the samples in 2 Mol/L NaOH for 2hours, and the final samples were washed by 2% H_2SO_4 and DI water several times and dried in a vacuum chamber to avoid oxidization. Since the uniform nanowire sample will be coated with hydrophobic coating for the dropwise condensation study, the sample needs to be kept facing down and being wet throughout the fabrication process to reduce the capillary force effect on nanowire direction that occurs during the drying process. The hydrophobic coating was finished by immersing the sample into the 2.5 mMol/L n-octadecanethiol (96% n-octadecylmercaptan, Acros Organics, 354980250) ethanol solution for 1 h.[25, 26] The temperature of the solution is controlled to be 70 ℃ in a water bath, and the chemical process during the coating process can be described as

$$C_{18}H_{37}SH+Cu \rightarrow C_{18}H_{37}SCu+1/2H_2 \qquad (2.1)$$

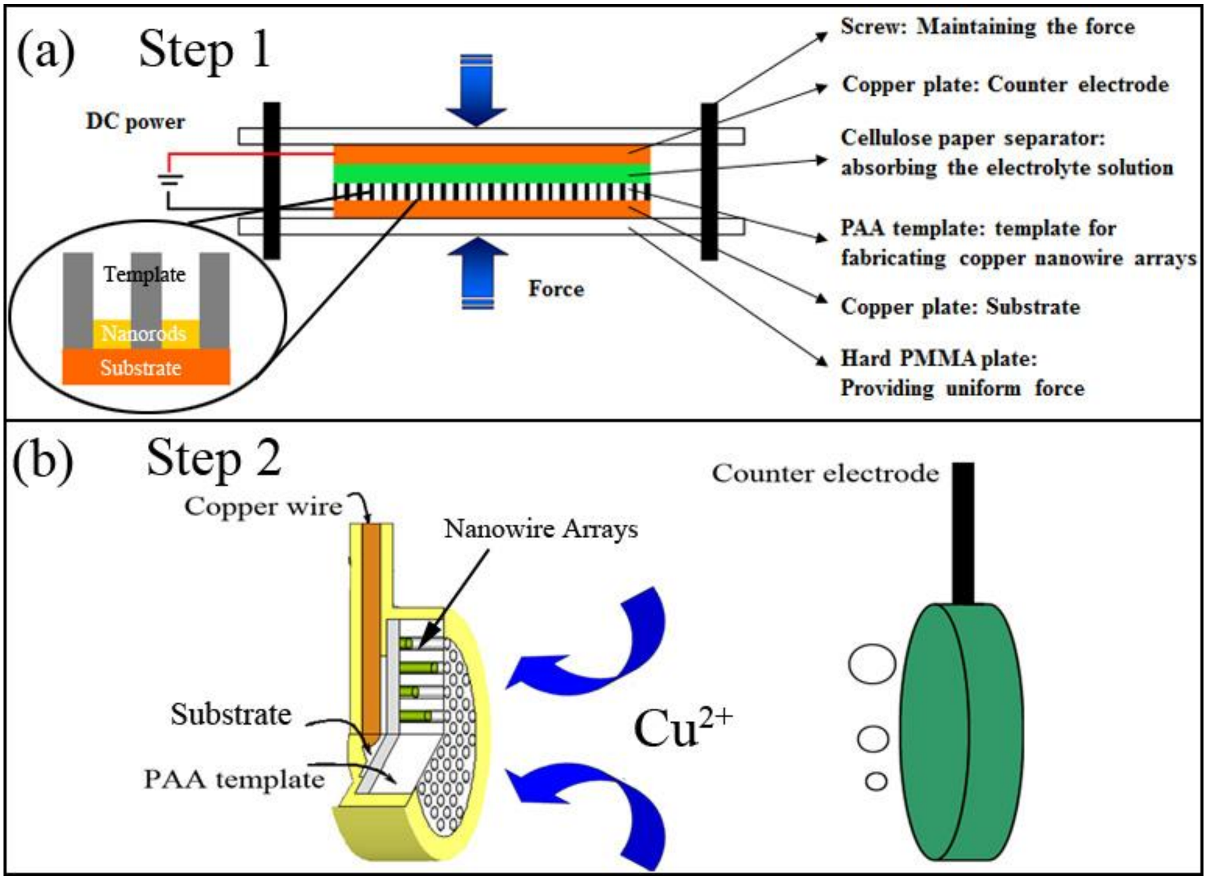

Figure 2. 2 Fabrication processes of uniform nanowires. (a) bonding step. (b) growing step.

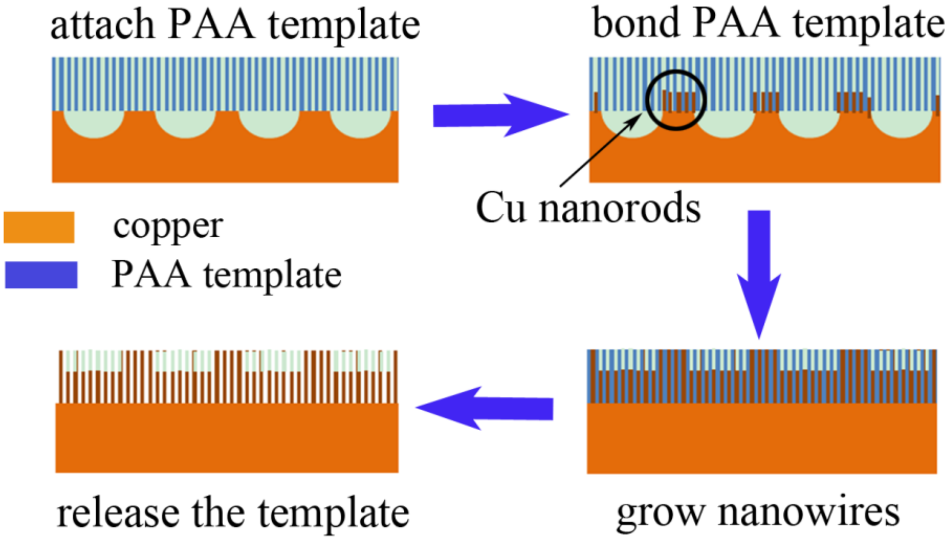

Figure 2. 3 Process flow of the fabrication of the micro-/nano- hierarchical structure

After the coating process, the sample was pulled out from the solution and kept facing down in a ventilation hood to guarantee uniform drying.

2.3 Fabrication of the copper nanowire/micropillar hierarchical structure

The fabrication process of the nanowire/micropillar hierarchical structured surface was the same as that for the uniform nanowired surfaces except that the substrate used here was the micropillared Cu sheet as shown in Figure 2.3. During the growing process, nanowires were first formed on top of the micropillars that were in contact with the PAA template. The channels between micropillars were filled with solid copper as what happened in a regular electrodeposition process. After the solid copper had contacted with the PAA template, nanowires started to grow at where the channels used to be along the nano holes in the PAA template. So the lengths of nanowires on top of the micropillars were larger than those in the channels. In this work, the nanowires on top of the micropillars are about 33 μm long while the nanowires in the channels were about 16 μm long.

2.4 Fabrication of the patterned copper nanowire array wicking structures

The fabrication process of the patterned copper nanowire array wicking structure consists of two steps, which are the fabrications of the patterned porous-anodic-alumina (PAA) template and the patterned nanowire arrays.

2.4.1 Fabrication of the patterned porous-anodic-alumina (PAA) template

The fabrication process flow is shown in Figure 2.4 (a). A 200 μm thick 99.999% purity aluminum sheet was first cleaned with acetone to remove the organic protection layer. The aluminum sheet with protection of scotch tape (3M Corp.) on one side was oxidized in -3 °C 0.3 Mol/L H_3PO_4 solution (85% H_3PO_4 : H_2O : 100% Ethanol = 3:160:40) to obtain 60 μm thick oxidization layer under 0.08A DC current for 72 h. The oxidization voltage was kept around 165V.

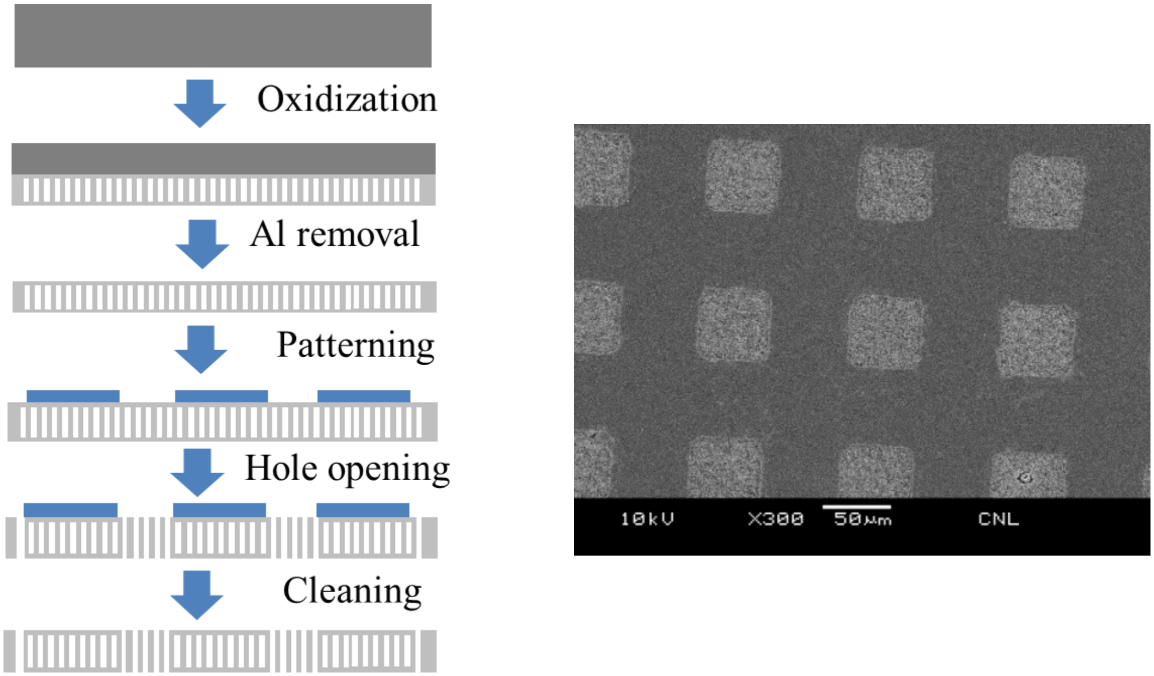

a b

Figure 2. 4 (a) Fabrication process flow and the (b) Top view SEM image of the patterned PAA template

A raw PAA sheet was obtained after removing the aluminum residue (~140 µm thick) from the protected side with 2 Mol/L $CuCl_2$ solution by replacement reaction. The PAA template was then cleaned by DI water and immersed in 3% H_3PO_4 for 30 min to remove any possible contamination. The PAA sheet contains uniformly aligned nano-holes inside. Up to this point, the nano-holes were not open on both sides of the template. The PAA sheet was dried by high purity N_2 and coated with 7 nm thick chromium as the adhesion layer by thermal evaporation method and then spin-coated with AZ9260 photoresist (PR) with a thickness of ~ 10 µm. The masks with square arrays were used to expose the PR on the PAA sheet in a maskaligner. After removing the exposed PR with AZ400K developer solution (AZ400K : H_2O = 8:10), the PAA sheet was processed in plasma reactive ion ether (RIE) with CF_4 and O_2 (CF_4 : O_2 = 1:4) gases to etch off the chromium not covered by PR and the alumina within the patterns exposed on the PAA sheet. The PAA sheet was then immersed in 45°C 3% H_3PO_4 solution for 3 h to open the nano-holes only within the patterns. The final step was to wash away the left PR and remove the chromium residue with CF_4 and O_2 plasma. A patterned PAA template was obtained with through nano-holes only in the predefined square arrays as shown in Figure 2.4 (b). The template was cleaned by oxygen plasma for 30 s to make it hydrophilic.

2.4.2 Fabrication of the patterned copper nanowire array wicking structures

The fabrication process flow is almost the same as that of the uniform nanowire structures except that the template used was the patterned PAA template obtained from the previous step and the solution to bond and grow nanowires was the $CuSO_4$ solution. Since the growth rate in the $CuSO_4$ solution was fast and not uniform, the length control of the nanowires couldn't depend on the control of the growing time any more. Thus the nanowires were grown out of the patterned PAA template and then the copper deposit outside the template was removed by a blade. To improve the uniformity of the lengths of the nanowires, the sample was put back to the $CuSO_4$ solution again for another round of electrodeposition until the nanowires grow out of the template. The length of the nanowires was thus controlled by the thickness of the patterned PAA template.

Chapter 3 Dropwise Condensation Heat Transfer Enhancement

3.1 Sample characterizations

Figure 3.1 (a) is the schematic diagram of the nanowire surface while the morphologies of the nanowired surfaces with SAM coating are shown in Figure 3.2, which are similar to those before coating despite some coating material residues. The average diameter (*D*), center-to-center spacing (*a*) and distribution of the nanowire are measured to be 213 nm, 382 nm and the triangular distribution, respectively. Based on the nanowire distribution and geometry, the solid fraction (φ) and the roughness factor (*r*) of the surfaces are calculated by

$$\varphi = \frac{\pi D^2}{2\sqrt{3}a^2} \tag{3.1}$$

$$r = 1 + \frac{2\pi D h}{\sqrt{3}a^2} \tag{3.2}$$

where φ is calculated to be 0.282.

The apparent contact angles of the nanowired surfaces after SAM coating are measured by the sessile drop method. The images are obtained using a high-speed camera (Photron FASTCAM SA4) with 5 μL DI water at atmospheric pressure and 20 ℃ and software (Analytical technologies, Fta32) is used in images analysis. The apparent contact angles are listed in Table 1. The contact angle on the smooth surface (θ) which is also the intrinsic contact angle is 114.6±2.6° with the same coating and under the same measuring conditions. Apparent contact angle on rough surfaces can be calculated according to[73]

$$cos\theta^* = -1 + \varphi(1 + cos\theta_{intrinsic}) \tag{3.3}$$

where θ^* is the calculated apparent contact angle. The measured apparent contact angles (139.2°, 143.6° and 144.3°) agree well with the calculated apparent contact angle (141.1°).

The roughness factors (*r*), which is the ratio between the total surface area and the projected area, are 27.5, 54.0, and 80.5 as shown in Table 3.1, respectively.

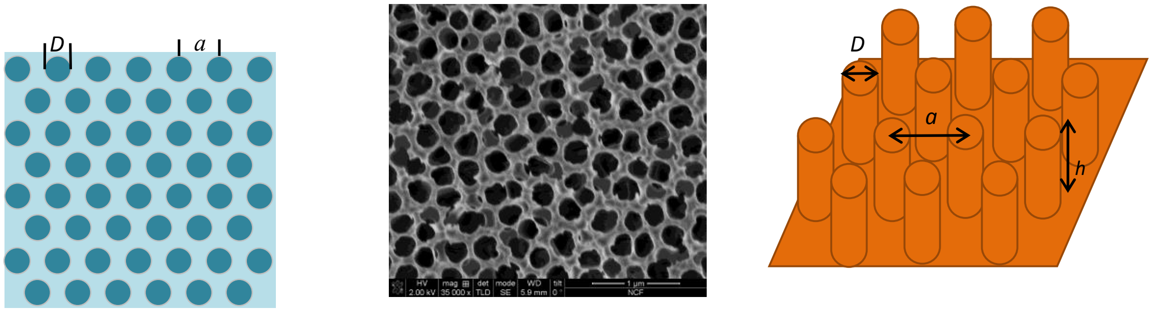

a b c

Figure 3. 1 (a) Schematic diagram of the PAA template. The light blue area shows the framework of the alumina, while the dark blue areas are the holes. (b) Scanning electron micrograph (SEM) of the PAA template. The gray area is the framework of the alumina, while the dark areas are the holes. (c) Schematic diagram of the nanowire surface.

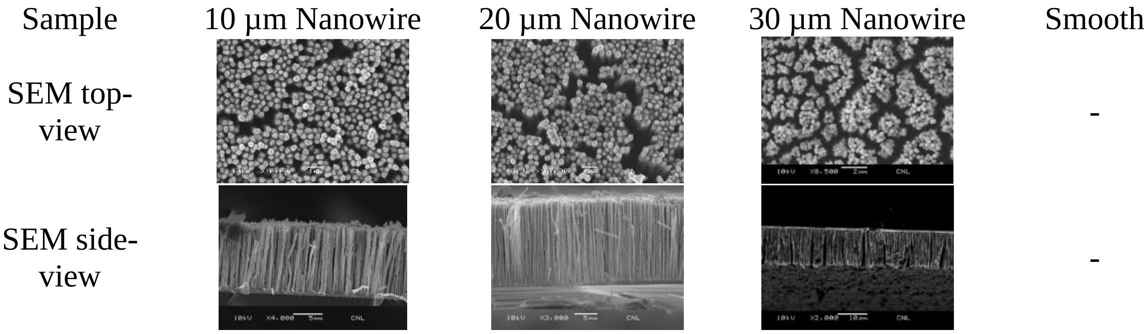

Figure 3. 2 Scanning electron micrograph (SEM) of copper nanowire arrays. The top-view, the side-view, and the droplet contact angles on the nanowired and smooth surfaces are displayed.

Table 3.1 Contact angles and roughness factors of the samples

Sample	10 µm Nanowire	20 µm Nanowire	30 µm Nanowire	Smooth
Contact angle	144.3±1.7°	139.2±3.5°	143.6±1.3°	114.6±2.6°
Calculated roughness factor (r)	27.5	54.0	80.5	-

The criterion to judge the state of the droplet on a structured surface is[24]

$$E^* = \frac{-1}{r\cos\theta_a} < 1 \tag{3.4}$$

where θ_a is the advancing contact angle on the smooth Cu surface with the same SAM coating.

Although the advancing contact angles on the nanowired surfaces haven't been measured, based on the roughness factor r on the nanowired surfaces and the contact angle on the smooth surface, θ_a has to be smaller than 92° to make $E^* \geq 1$. Thus, droplets on all the nanowired hydrophobic surfaces can stay in Cassie or partially-wetting Cassie state under the non-condensation condition.[23]

3.2 Testing system and data reduction

3.2.1 Testing system

Referenced the condensation experiment in literatures, [74, 75] an experimental setup is designed and built to conduct the simultaneous heat transfer measurement and condensate pattern visualization, as shown in Figure 3.3 (a) and (b). The experimental setup consists of the vapor generator, testing chamber, the refrigeration and data acquisition systems. The evaporator is a Φ76 mm × 900 mm vertical cylinder, with electric heaters inside the chamber. The heater is non-uniform designed, where the heating power under water level (see Figure 3.3 (b)) is much larger than that of the upper part to boiling the water, while the upper part of the heater functions as a super heater. The heating power can be adjusted by a direct-current regulator (Agilent, N5771A). The steam temperature is measured by a thermocouple at the outlet of the evaporator, which is always 0.2 to 0.3 K higher than the saturation temperature in the testing chamber. After the steam leaves the evaporator, it enters the testing chamber through a ¾ inch inner diameter connecting pipe. In order to keep the steam superheated, the connecting pipe is heated by an adjustable heating tape (Omega, HTWC 101-004) and covered with insulation materials outside.

Condensation occurs in the testing chamber, which is a stainless steel cylinder with the inner dimensions of Φ263 mm × 50 mm, as shown in Figure 3.3 (a) and (b). Flanges are used for sealing the end faces of the testing chamber. The steam connection pipe is installed on the cover flange and the testing sample is located vertically below the connection pipe. The copper sample is designed to have two platforms as shown in Figure 3.3 (c). The larger platform (with 90 mm diameter) of the copper sample can keep good thermal contact with the copper cooler with thermal grease (Arctic, MX-4) during experiment, and the smaller platform is the test surface with the diameter of 40 mm. Figure 3.3 (d) is the photo of the test surface with nanowire arrays and the SAM coating.

The flange with a 100 mm diameter glass seals the other end face of the testing chamber. The distance from the testing sample to the glass is about 50 mm to meet the requirement of the microscope. The condensation patterns on the test surface can be captured by the high speed camera (Photron FASTCAM SA4) through a transparent window simultaneously with the heat transfer measurement of condensation. At the bottom of the test section, a backflow pipe can lead the condensate to the bottom of the evaporator.

A cooling water loop removes the heat due to condensation on the test surface. A constant temperature water circulator (Thermo Electron Corporation, HAAKE Phoenix II), a flow meter (Proteus Industries, 08004SN1, with the accuracy of ±3%), a copper cooler, linking pipes and temperature sensors (Omega, T type, with the accuracy of ±0.15 K) are embedded in the cooling

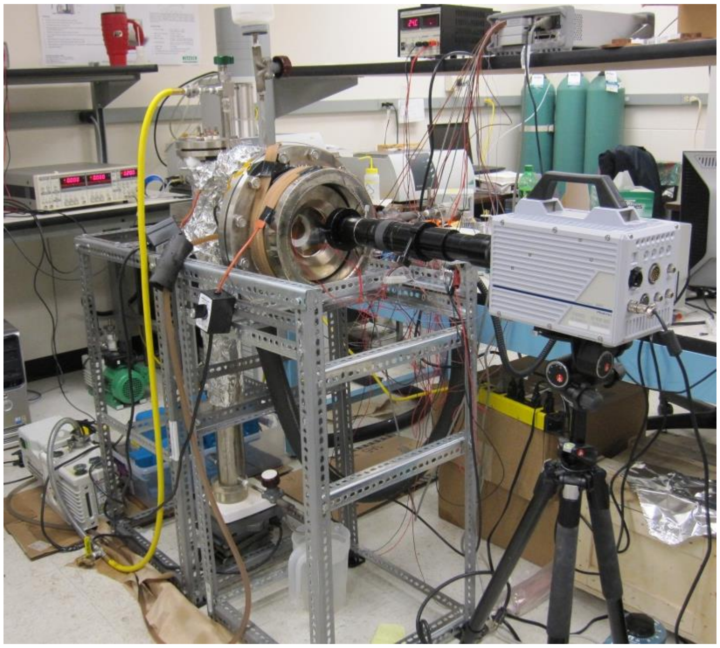

(a)

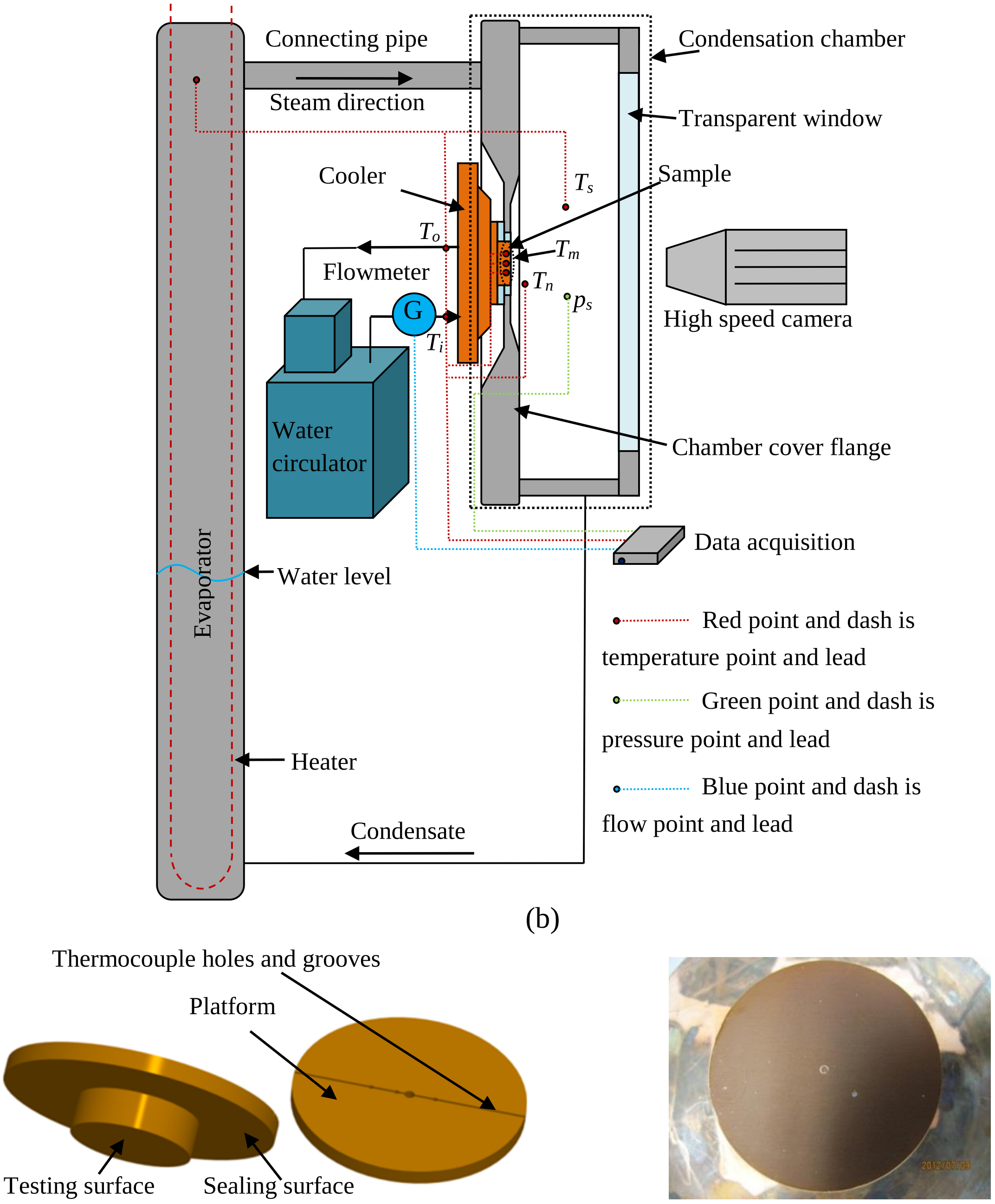

(b)

(c) (d)

Figure 3. 3 (a) Photo of experimental setup. (b) Schematic of experimental setup. (c) Schematic of copper sample. (d) Photo of the nanowire surface.

water loop, as shown in Figure 3.3 (b). Based on a heat balance, the heat transfer rate on the test surface is calculated from the heat absorption on the cooling water side.

3.2.2 Data reduction

The cooling water inlet and outlet temperatures (T_i, T_o) and the mass flow rate (G) are measured by the thermocouples and the flow meter, respectively. The heat flux (q) of the test surface is calculated by,

$$q = \frac{cG\left(T_o - T_i\right)}{A} \tag{3.5}$$

where c is the specific heat capacity of cooling water and A is the area of the test surface, which is 12.57 cm^2 for the 40 mm diameter round plate. In order to keep the steady condition, the inlet cooling water temperature (T_i) is controlled by the water circulator with the fluctuation less than ±0.1 K. For the heat flux (q) measurements, steady state is maintained for more than 40 min for each data point. The resulting data acquired from the time average over 10 min and the fluctuations are seldom larger than ±2.5 kW/m^2 under equilibrium conditions. Insulation material and washer are adopted to insulate the copper cooler and sample from the surroundings and testing chamber. The system error caused by heat leakage is estimated to be -1.88 to 4.78 W/m^2 as subcooling increase from 0 K to 60 K. Based on the error propagation, the maximum error for the heat flux measurement can be calculated as:

$$\sigma_{max}(q) = \frac{c(T_o - T_i)}{A}\sigma(G) + \frac{cG}{A}\sigma(T_o) + \frac{cG}{A}\sigma(T_i) + \frac{cG(T_o - T_i)}{A^2}\sigma(A) \tag{3.6}$$

Considering the instrumentation accuracy and error accumulation, the absolute errors for the heat fluxes are estimated to be around 9.77 to 14.1 kW/m^2, which are the error bars shown in Figure 3.5 (a).

The subcooling (ΔT) is the temperature difference between the steam temperature (T_s) and wall temperature (T_w),

$$\Delta T = T_s - T_w \tag{3.7}$$

The measurement of T_s and T_w are carefully designed in the experiment. The steam temperature (T_s) is measured by the thermocouple (Omega T type ±0.15 K) in the testing chamber. As shown in Figure 3.3 (b), two temperature points are set in the testing chamber. One point (T_n) is near the lower end of the sample with the distance to the sample at about 5 mm, another point (T_s) is located at the side of the sample with the distance to the sample of about 80 mm. In addition, the steam pressure (p_s) is also measured by pressure sensor (Omega, PX409-050AI, ±0.08% accuracy) in the testing chamber and is controlled at 60 kPa with fluctuation amplitude of ±0.05 kPa. The deviations of the temperature data and the steam pressure are calculated as

$$W_s = \frac{p_s - p_s\left(T_s\right)}{p_s} \times 100\% \tag{3.8}$$

$$W_n = \frac{p_s - p_s\left(T_n\right)}{p_s} \times 100\% \tag{3.9}$$

where, $p_s(T_s)$ and $p_s(T_n)$ are the saturation pressure calculated by the T_s and T_n, respectively. When experiment, $p_s(T_s)$ has a good agreement with the steam pressure (p_s), W_s is always within the range of ±0.3% and never exceed the range of ±0.5% . For this reason, T_s reflects the saturation temperature of the steam in the testing chamber and is selected in calculating the subcooling in Eq. (3.7).

T_n is usually smaller than T_s in the experiments. This is mainly caused by the concentration of NCG, so W_n is the mole fraction of NCG near the condensation surface. W_n will increase with the increase of the subcooling, as shown in Figure 3.4 (a). Large errors may occur at small subcooling, but the data for ΔT>0.5 K is precise enough. Because the steam velocity in our experiments is negligible, W_n can reach about 6% at large subcooling conditions, which is about 2.4 K lower than the saturation temperature. Therefore, the main function of temperature point T_n is to estimate the NCG level near the condensation surface.

In addition, although NCG is allowed and inevitable in the system, good sealing is required. Otherwise, not only T_s and T_n but also the heat flux (q) cannot keep steady during condensation. In order to verify the sealing condition, tests should be performed before the experiments. The absolute pressure inside the system is vacuumed to 1 Pa measured by the (MKS 722B11TFE2FJ) pressure sensor using a vacuum pump (Edwards, RV8) at dry condition, and the absolute pressure is kept to less than 25 Pa for 24 hours.

The wall temperature (T_w) is calculated based on the readings of thermocouples (Omega, T type ±0.15 K) inserted into the copper sample. Three holes and a groove are located at the backside of the copper sample (see Figure 3.3 (c)) for thermocouple pigtails. The holes are 2 mm in diameter and have the distance of 5 mm, 10 mm and 15 mm, respectively, to the center of the sample. All thermocouple holes have the same depth, and distances of these holes' bottoms to test surface (δ) is 3.5 mm considering the thermocouple head size. Assuming one-dimensional heat conduction from the thermocouples and the test surface, the wall temperature could be calculated by

$$T_w = T_m + \frac{q\delta}{k} \tag{3.10}$$

where, T_m is the mean value of the thermocouple readings, and k is the thermal conductivity of copper, which is 398 W/(mK) with the relative error within ±1% considering the changing temperature. During the condensation process, the tested surface temperatures are not uniform. The maximum differences in the thermocouple readings are less than 0.5 K in our experiment. The relative error of δ is estimated to be ±25%, in which three error sources, the mechanical processing error (±0.25 mm), thermocouple size (±0.13 mm) and the installation error (±0.5 mm), are considered. Thus the maximum error for the subcooling can be calculated as:

$$\sigma_{max}(\Delta T) = \sigma(T_s) + \sigma(T_m) + \frac{\delta}{k}\sigma(q) + \frac{q}{k}\sigma(\delta) + \frac{q\delta}{k^2}\sigma(k) \tag{3.11}$$

In the experiment, all values of the temperature, pressure and flow rate are collected by the data acquisition (Agilent, 34970A) simultaneously with the video capturing, while the heat transfer data and images are saved separately.

Heat transfer performance was studied on the hydrophobic nanowired surfaces with reference to that on the hydrophobic smooth surface at a subcooling ranged from ~ 0 K to ~ 30 K. W_n increased with subcooling, which is the result of the zero-velocity of the water vapor steam and the residue air in the water. The similar slopes of the NCG curves show that the sealing of the system is working well and consistent. The testing system was first calibrated with filmwise condensation on a clean copper surface under a face-down direction and a 100 kPa pressure condition. The testing result matches the theoretical models and Chung's[74] experimental data well as shown in Figure 3.4 (b). The system thus can deliver reasonably accurate temperature and heat flux measurements and can be used for further dropwise condensation studies.

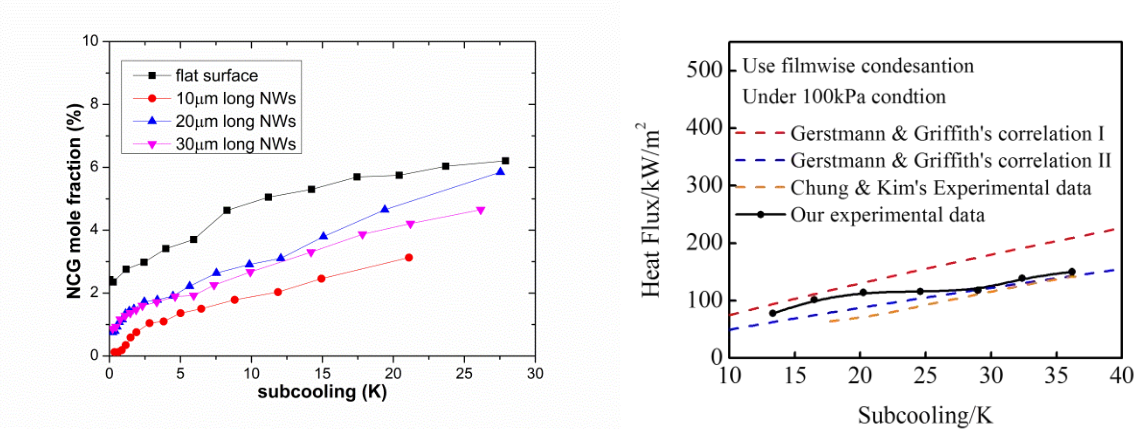

(a) (b)

Figure 3. 4 (a) Non-condensable gas (NCG) mole fraction near surfaces. (b) Comparison of filmwise condensation performance of the theoretical models, experiment data in the literature, and experiment data from our testing system

3.3 Testing results

The condensation heat transfer curve is shown as the relation between the subcooling and the heat flux. Figure 3.5 (a) presents the condensation heat transfer performance on nanowired and smooth surfaces. The heat transfer curve on the smooth Cu surface has the trend that the heat flux increases monotonically as the subcooling increases. The slope of the heat transfer curve monotonically decreases as shown in Figure 3.5 (b). The heat transfer curves on 10, 20, and 30 μm long nanowired surfaces have a trend which is different from that on the smooth surface. The heat flux first increases with the increase of the subcooling in 0 K to ~8 K range. The heat flux decreases as the subcooling increases from ~8 K to ~15 K. After the end of the transition at ~15 K, the heat flux increases again with the increase of the subcooling and the heat transfer curves overlap with that on the smooth Cu surface. The heat transfer coefficient (HTC), which is the ratio between the heat flux and the corresponding subcooling, on the smooth surface is better than those on the nanowired surfaces when the heat flux is smaller than 30 kW/m^2 and decreases as the heat flux increases throughout the entire heat flux range. In contrary, the HTCs on the nanowired surfaces increase first and then decrease with the increase of the heat flux. When the heat flux is ~45 kW/m^2, the HTC on the 20 μm long nanowired surface is ~ four times that of the HTC on the smooth surface. A clear transition occurs which is identified by a change in slope in the HTC curves on the nanowired surfaces. After the transition, the HTCs on all the surfaces are the same, which indicates a similar heat transfer performance on all the surfaces. The heat transfer curve of the 10 μm long nanowired surface is similar to that of the 30 μm long nanowired surface, and lower than that of the 20 μm long nanowired surface.

When the nanowires were fabricated through electrodeposition method, the coverage of the nanowires was not constant. The longer the deposition time was, the better the coverage was. However, when the nanowires are long enough, the agglomeration of the nanowires became

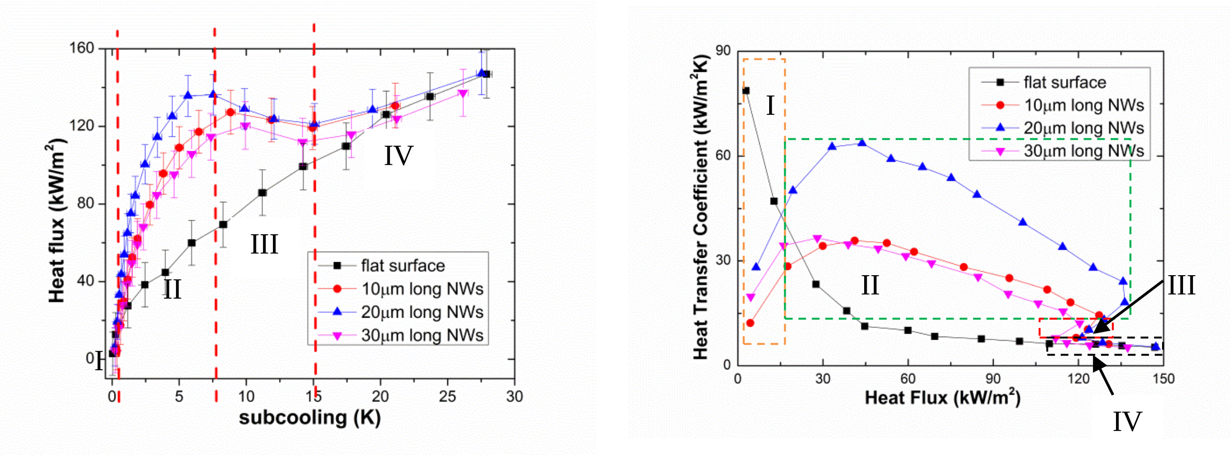

(a) (b)

Figure 3. 5 (a) Condensation heat transfer performance (heat flux vs subcooling) on nanowired and smooth surfaces. (b) The relation between heat flux and heat transfer coefficient (HTC) on all the surfaces

severe and resulted in very small space in the nanowire bundles for coating solution to penetrate. Thus, there were a lot of defects on the 10 μm and 30 μm long nanowired surfaces that may result in trapping of the condensate within the nanowires and degrade the heat transfer performance of the structures. One thing worth noting is that the HTCs on the nanowired surfaces reach their maximum value and start to decrease when the heat flux is ~45kW/m^2 which corresponds to a subcooling of ~2 K.

In order to study the influence of the subcooling or heat flux on the condensation heat transfer performance of the nanowired surfaces, the condensation process was recorded by a high-speed camera simultaneously with the heat transfer measurement on all nanowired and smooth surfaces. The droplets' coalescence and removal are the important processes of dropwise condensation.[75,76,77] Comparison of the videos and the heat transfer results shows that the heat transfer performance of the nanowired surface is closely associated with the droplet states and the droplet removal modes under different subcoolings. The state of the droplets can be distinguished by the brightness of the droplet.[14] Due to the different reflections of the incoming

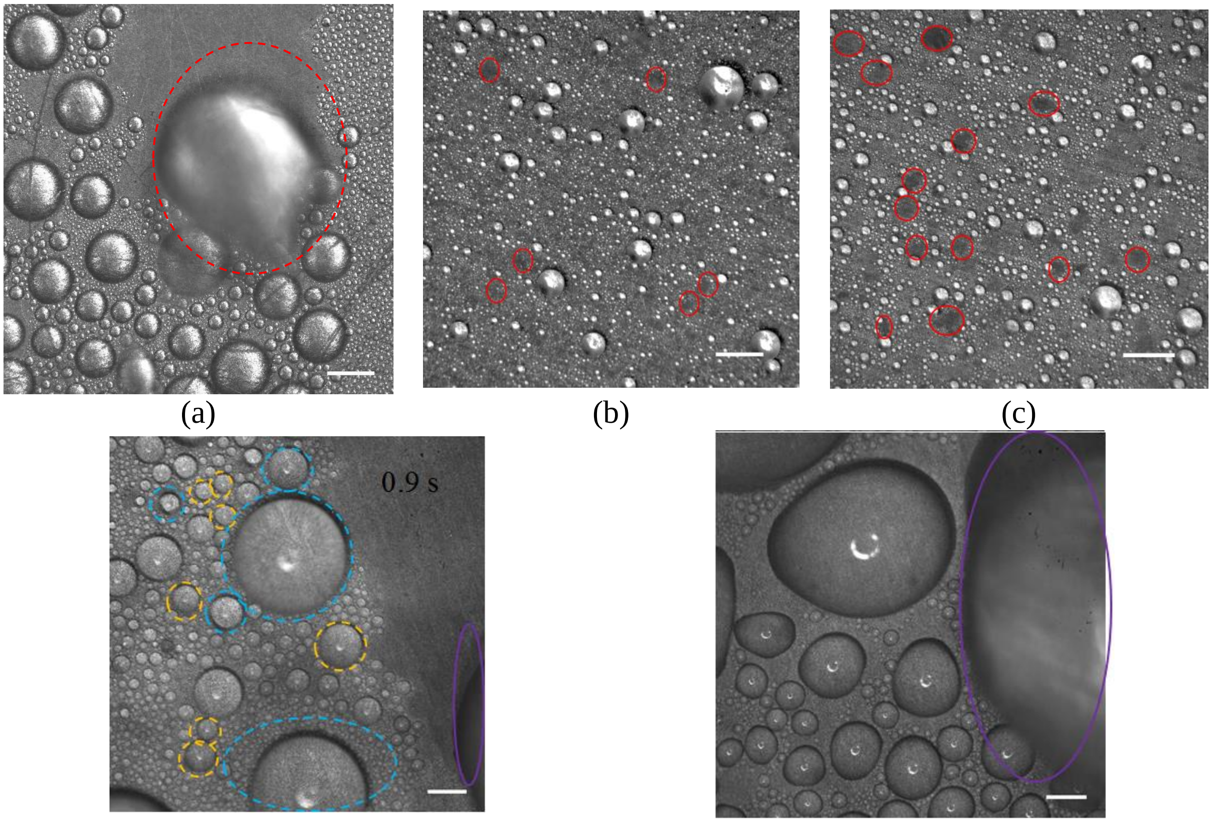

(a) (b) (c)

(d) (e)

Figure 3. 6 (a) Image of condensation on smooth surface. The read dash circle presents a droplet sweeping the surface under gravity. (b) Image of the typical condensation patterns on 20 µm long nanowired surface under ΔT=0.23 K. The red circles point out some spots after the jumping of the coalesced droplets. (c) Image of the typical condensation patterns on 20 µm long nanowired surface under ΔT=4.5 K. The red circles point out some spots after the jumping of the coalesced droplets. (d) Image of the typical condensation patterns on 20 µm long nanowired surface under ΔT=10 K. Droplets in the yellow dash circles, blue dash circles, and purple solid circles are the droplets in Wenzel and Cassie state and the sweeping droplet. (e) Image of the typical condensation pattern on 20 µm long nanowired surface under ΔT=30 K. The purple circle presents a droplet sweeping the surface. The scale bar is 500 µm for all these images.

light, light color and dark color show the pure/partially-wetting Cassie and Wenzel states, respectively.

Figure 3.6 shows the droplet states and droplet removal modes on the nanowired and smooth samples. Figure 3.6 (a) is a typical image for the droplet coalescence and removal on the smooth surface. The bottom of the droplets are in full contact with the surface and the removal mode, which is sweeping, is almost the same throughout the entire subcooling range except for the density and the diameters of the droplets and the sweeping cycle (the sweeping removal mode is provided in Video 1 in the supporting information). In contrast, the droplet states and the removal modes on nanowired surfaces are different under different subcoolings. Four typical droplet states and droplet removal modes can be found on all of the nanowired surfaces under different subcooling conditions despite the different lengths of the nanowires, as shown in Figure 3.6 (b), (c), (d) and (e) (the videos for droplet behaviors on 20 μm long nanowired surface are in the supporting information). For the ΔT<~8 K and ΔT>~15 K conditions, the droplet states are in pure/partially-wetting Cassie and Wenzel state and the droplets are removed only by coalescence induced jumping and sweeping mode respectively as shown in Video 2, Video 3, and Video 5 in the supporting information. For ~8 K <ΔT <~15 K conditions, partially-wetting Cassie and Wenzel state droplets coexist on the surface and the wetting states change from partially wetting Cassie state to Wenzel state with the coalescence and condensation processes. The droplets can be removed by both coalescence induced jumping and sweeping modes and Video 4 in the supporting information records the process.

3.4 Discussions

Based on the condensation heat transfer performance on nanowired surfaces compared with that on a smooth surface, the entire condensation heat transfer process can be divided into four regions as shown in Figure 3.5 (a) and (b).

In the first region, the heat transfer coefficient on the smooth surface is even better than those on the 10 μm, 20 μm, and 30 μm long nanowired surfaces when the heat flux is smaller than 30 kW/m^2 corresponding to a subcooling at ~0.3 K. The relatively large size of the smallest viable droplet[77] is the reason for the unexpected heat transfer performance. The smallest or the critical viable droplet radius is

$$R_c = \frac{2\sigma_{lv} T_{sat}}{\rho_w H_{fg} \Delta T} \tag{3.12}$$

where σ_{lv} and ρ_w are the surface tension and density of water, respectively, T_{sat} is the saturation temperature of water under experiment pressure condition, and H_{fg} is the latent heat of evaporation of water. The diameter of the smallest viable droplet when ΔT=0.3 K is $D_c=2\times R_c$~100 nm which is comparable to the gap size (a-D) between the nanowires. Thus, once a droplet is able to form and keep growing, it can only form and stay at the defect on the top of the nanowire tips as a pure Cassie state droplet. The heat transfer rate of pure Cassie state droplets is the worst among partially-wetting Cassie, Cassie state droplets, and droplets on the smooth surface.[11] Thus, the heat transfer performance on 10, 20, and 30 μm long nanowired surfaces is even worse than that on the smooth surface.

When it's in the second region, the subcooling is large enough to form droplets at the defects in the gaps of the nanowires. Figure 3.6 (c) is the image for the typical condensation patterns on 20 μm long nanowired surface at $\Delta T\approx 4.5$K. The most remarkable feature under $\Delta T<\sim 8$ K condition is that the droplets' coalescence and jumping is the only way to remove the condensate. The red circles in Figure 3.6 (c) are some of the spots after the jumping off of the coalesced droplets. As calculated with Eq. (3.4), the nanowired surfaces with hydrophobic coating in this study are all Cassie stable surfaces. Furthermore, the ratio between the diameter (d) and the distance (l) between the nanowires, which is $d/l\approx 0.56$, indicates that there is a water bridge between the droplet on top of the nanowire tips and the substrate.[78] Droplets in this state are the partially-wetting Cassie state droplets and present the best heat transfer rate. Based on the solid fraction of the nanowire surfaces and the contact angle on the hydrophobic smooth Cu surface, a characteristic energy barrier which limits the wetting behavior of the condensate when it first grows out of the gap between the nanowires can be defined as:[79]

$$\Delta E_u^* = \frac{\Delta E_t}{\Delta E_s} \tag{3.13}$$

where ΔE_t and ΔE_s are the energy barriers at the side and the top of the nanowires, respectively. ΔE_u^* on all the hydrophobic nanowired surfaces in this study is ~0.96 < 1, which means that once the condensate grows out of the gap the droplet will continue growing on the tips until it reaches the adjacent gaps as shown in Figure 3.7 (a) to (b). The droplets will continue growing on the tips of the hydrophobic structures, as shown in Figure 3.7(c).[80] Based on the analysis above, the width of the water bridge is about the size of one to several gaps between the nanowires so that the contact line is short compared with the dimensions of the droplet. Extra surface energy is released after the droplets' coalescence and this energy is high enough to overcome the resistance at the contact line and push the coalesced droplet away from the hydrophobic surface as shown in Figure 3.7 (d) to (e).[16] The partially-wetting Cassie state droplets and the fast coalescence induced jumping removal mode together result in the enhanced condensation heat transfer performance on the hydrophobic nanowired surfaces.

As subcooling or heat flux increases, more and more nucleate sites are activated, which results in faster droplet removal due to the reduced droplet size and droplet-droplet distance. The jumping removal manner of the droplets guarantees enough dry area for the fast formation of new nucleate sites. The HTCs on the nanowired surfaces thus increases as the increase of the subcooling.

However, as the liquid is going to wet the surface at ΔT≈2 K,[24] there was no Wenzel state droplets appearing on our testing surfaces and coalescence-induced jumping was still the only way to remove liquid from the surface. Whether the liquid can wet down from the tips of the nanowires to the substrate depends on the angle between the liquid-vapor interface and the

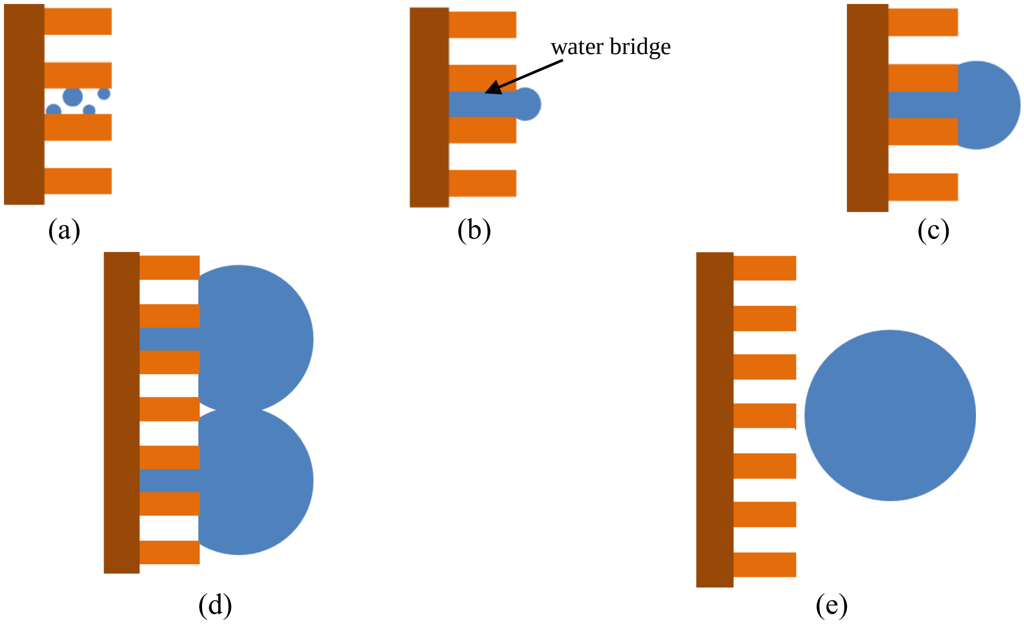

Figure 3. 7 Schematics of the droplet growth-coalescence-jump off process under small subcooling on nanowired surfaces. (a) Condensate in discrete nanowire gaps. (b) Condensate accumulating and growing out of the nanowire tips. (c) The droplet grows only on the tips of nanowires as partially-wetting Cassie state droplet without interaction with neighboring droplets or condensate. (d) Coalescence of two partial Cassie state droplets. (e)The coalesced droplet jumping off from the surface.

extended outline of the structure into the liquid as shown in Figure 3.8.[79] The angle can be calculated as

$$cos\alpha = \sqrt{\pi}\sqrt{\varphi}cos\theta_a + (1 - 2\frac{\sqrt{\varphi}}{\sqrt{\pi}}) \tag{3.15}$$

The angle is a function of the solid fraction. Fig. 3.9 shows the relation between the calculated angle and the solid fraction. As we can see from the plot, once the solid fraction is higher than 0.246, α is always larger than 90°. As a consequence, the liquid can never wet down.[79, 80] Since the solid fraction of our nanowired surfaces is ~ 0.282, α is ~ 94°, which means the liquid can't go down from the tips of the nanowires. Therefore, the formation of Wenzel state droplets doesn't result from the wetting down process, which makes enhanced dropwise condensation heat transfer performance possible on our surfaces. When a droplet forms at a certain nucleate site and keeps growing under condensation condition, the temperature at this location is the

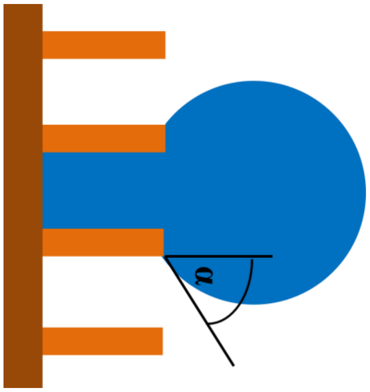

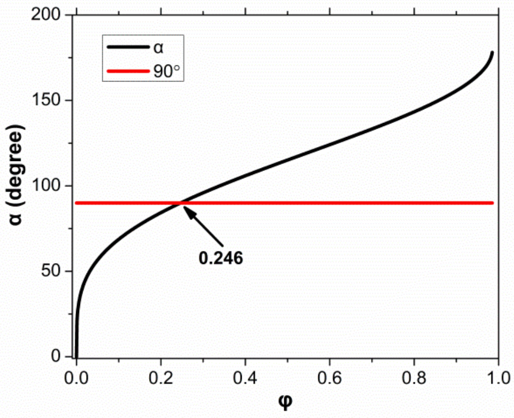

Figure 3. 8 Angle that controls the wetting down movement of the liquid

Figure 3. 9 The relation between the solid fraction and the angle

lowest comparing with the temperature around this location as shown in Figure 3.10. As subcooling further increases, new nucleate sites generate close to the existing nucleate site in the gaps and coalesce with the existing water bridge of the droplet. The water bridge grows, which increases the wetting area beneath the partially wetting Cassie state droplet as shown in Figure 3.11. Once the wetting area is large, the adhesion force increases so that the liquid in the gaps can't be pulled out of the structures. However, coalesced droplet can still jump from the surface with the water bridge remains in the gaps as shown in Figure 3.12. A factor *f* is defined as the ratio between the wetting area and the contact area beneath the droplet. The total surface energy of the two droplets before coalescence is

$$E_{before} = E_{droplet\_1} + E_{droplet\_2} \tag{3.16}$$

The surface energy for a partially wetting droplet consists of the energy from the solid-liquid, solid-gas, and gas-liquid interfaces. The energy from the liquid-vapor (lv) interface, the energy from the liquid-solid interface (sl), and the energy from the solid-vapor (sv) interface are:[81]

$$E_{lv} = \sigma_{lv}A_{lv} = \sigma_{lv}[2\pi(R_1^2 + R_2^2)(1 - cos\theta) + \pi(R_1^2 + R_2^2)sin^2\theta(1 - f)(1 - \varphi)] \tag{3.17}$$

$$E_{sl} = \sigma_{sl}A_{sl} = \sigma_{sl}[\pi(R_1^2 + R_2^2)sin^2\theta fr + \pi(R_1^2 + R_2^2)sin^2\theta(1 - f)\varphi] \tag{3.18}$$

$$E_{sv} = \sigma_{sv}A_{sv} = \sigma_{sv}[A_{total} - \pi(R_1^2 + R_2^2)sin^2\theta fr - \pi(R_1^2 + R_2^2)sin^2\theta(1 - f)\varphi] \tag{3.19}$$

where σ is the interface surface tension, A is the interface area, R is the radius of the droplet before coalescence, θ is the apparent contact angle, A_{total} is an arbitrary control area that contains at least the two droplets, and r is the surface roughness. According to Eq. (3.16), we get the total surface energy before coalescence:

$$\begin{aligned} E_{before} = {} & \sigma_{sv}A_{total} + \sigma_{lv}2\pi(R_1^2 + R_2^2)(1 - cos\theta) \\ & + \sigma_{lv}\pi(R_1^2 + R_2^2)sin^2\theta(1 - f)(1 - \varphi) \\ & + \pi(R_1^2 + R_2^2)sin^2\theta fr(\sigma_{sl} - \sigma_{sv}) + \pi(R_1^2 + R_2^2)sin^2\theta(1 \\ & - f)\varphi(\sigma_{sl} - \sigma_{sv}) \end{aligned} \tag{3.17}$$

Since $\sigma_{sv} - \sigma_{sl} = \sigma_{lv}cos\theta_{intrinsic}$,[82] Eq. (3.17) becomes:

$$\begin{aligned} E_{t\_before} & = E_{lv} + E_{sl} + E_{sv} \\ & = \sigma_{sv}A_{total} + \sigma_{lv}2\pi(R_1^2 + R_2^2)(1 - cos\theta) \\ & + \sigma_{lv}\pi(R_1^2 + R_2^2)sin^2\theta(1 - f)(1 - \varphi) \\ & - \sigma_{lv}cos\theta_{intrinsic}\pi(R_1^2 + R_2^2)sin^2\theta fr \\ & - \sigma_{lv}cos\theta_{intrinsic}\pi(R_1^2 + R_2^2)sin^2\theta(1 - f)\varphi \\ & = \sigma_{sv}A_{total} + \pi\sigma_{lv}(R_1^2 + R_2^2)[2(1 - cos\theta) + sin^2\theta(1 - f)(1 - \varphi) \\ & - sin^2\theta cos\theta_{intrinsic}fr - sin^2\theta cos\theta_{intrinsic}(1 - f)\varphi] \end{aligned} \tag{3.18}$$

After coalescence, the liquid under the two partially-wetting droplets remains in the structure while the liquid on the tips of the structure forms a new droplet as shown in figure 3.12. The energy from the interfaces is[81]

$$E_{lv} = \sigma_{lv}[4\pi R_0^2 + \pi(R_1^2 + R_2^2)sin^2\theta f(1 - \varphi)] \tag{3.19}$$

$$E_{sl} = \sigma_{sl}[\pi(R_1^2 + R_2^2)sin^2\theta fr - \pi(R_1^2 + R_2^2)sin^2\theta f\varphi] \tag{3.20}$$

$$E_{sv} = \sigma_{sv}[A_{total} - \pi(R_1^2 + R_2^2)sin^2\theta fr + \pi(R_1^2 + R_2^2)sin^2\theta f\varphi] \tag{3.21}$$

The total surface energy after coalescence is then:

$$\begin{aligned} E_{after} = \sigma_{sv}A_{total} + \pi\sigma_{lv}[4R_0^2 + (R_1^2 + R_2^2)sin^2\theta f(1 - \varphi - rcos\theta_{intrinsic} \\ + \varphi cos\theta_{intrinsic})] \end{aligned} \tag{3.22}$$

where *R₀* is the radius of the coalesced droplet (sphere):

$$R_0 = [\frac{1}{4}(R_1^3 + R_2^3)(2 - 3cos\theta + cos^3\theta)]^{1/3} \tag{3.23}$$

The coalescence process results in viscous dissipation. The energy dissipated in this process is:[83]

$$E_{dis} = 72\pi\mu\sqrt{\frac{\sigma_{lv}}{\rho_l}}(R_1^{1.5} + R_2^{1.5}) \tag{3.24}$$

where μ and ρ_l are the dynamic viscosity and density of the liquid.

If the coalesced droplet is able to leave the surface, it must have kinetic energy. The kinetic energy results from the energy difference between the total surface energy before and after the coalescence process as shown in Eq. (3.25)

$$\begin{aligned} E_{kinetic} = E_{t\_before} - E_{t_{after}} - E_{dis} = \\ = \pi\sigma_{lv}\{(R_1^2 + R_2^2)[2(1 - cos\theta) + sin^2\theta(1 - f)(1 - \varphi) \\ - sin^2\theta cos\theta_{intrinsic} fr - sin^2\theta cos\theta_{intrinsic}(1 - f)\varphi \\ - sin^2\theta f(1 - \varphi - rcos\theta_{intrinsic} + \varphi cos\theta_{intrinsic})] - 4R_0^2\} \\ - 72\mu\sqrt{\frac{\sigma_{lv}}{\rho_l}}\left(R_1^{1.5} + R_2^{1.5}\right) \end{aligned} \tag{3.25}$$

As long as the kinetic energy is larger than 0, the droplet can jump from the tips since the condensation surface was placed vertically so that gravity doesn't provide extra resistance. By changing the value of *f* and φ, the result for the kinetic energy is shown in Fig. 13. As we can see from the result, the coalesced droplet can jump only when the wetting area is smaller than 2% on our nanowired surfaces. If the solid fraction reduces to 0.1, the coalesced droplet can jump until the wetting area grows to 7%. However, when the solid fraction is 0.3, the coalesced droplet can't jump unless the wetting area is only one or several nanowire gaps' large. Since the coalesced droplet can still jump from the surface but leave the water bridge in the structures, there are less dry area on the surface. The HTC decreases accordingly. Once the wetting area is large enough, the droplet that can't jump from the surface will stay on the surface for a longer time. As

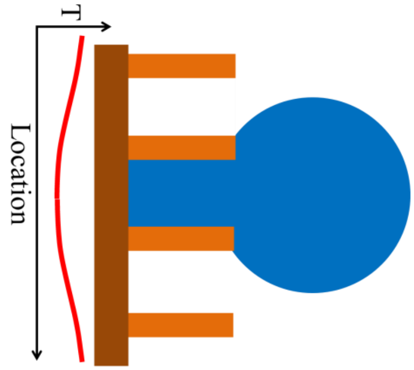

Figure 3. 10 Temperature profile around a droplet

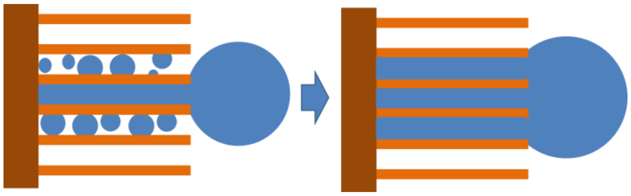

Figure 3. 11 Nucleate sites form around the existing droplet and growing of the water bridge

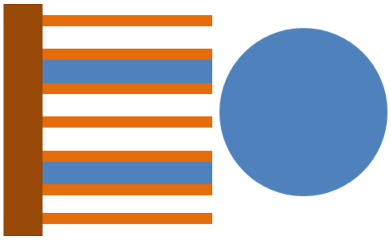

Figure 3. 12 Jumping coalesced droplets with water bridge remaining in the structures

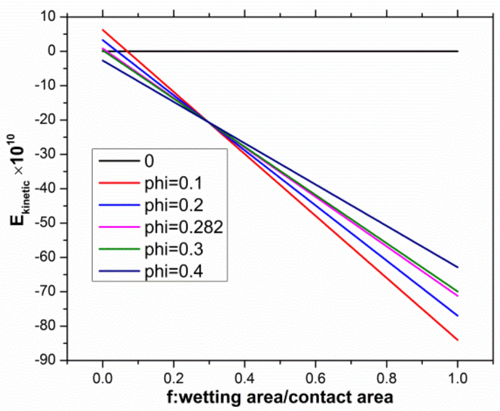

Figure 3. 13 The kinetic energy of the coalesced droplet as a function of solid fraction and wetting area

subcooling increases, more and more nucleate sites form, grow, and coalesce with the droplet on the tips. Finally, Wenzel state droplet forms when the subcooling is ~10 K.[86] On small solid fraction nano-structured hydrophobic surfaces, the coalesced droplet can jump under large wetting area, which can extend the subcooling range for enhanced dropwise condensation heat transfer performance.

As heat flux or subcooling further increases into the third region, although the condensation heat transfer performance has been enhanced, a transition occurs and both HTC and heat flux decrease with the increase of the subcooling. In our experiment, the jumping off removal mode only occurs when ΔT<~15 K on nanowired surface and it is fully diminished when the subcooling further increases to ΔT>~15 K. The gradual reduction of the droplet jumping off results from the transition of the wetting state as subcooling increases.

Under the ~8 K <ΔT< ~15 K subcooling conditions, the brightness of droplets changes from time to time, which reflects the state transition of the droplets and is one of the most remarkable features in this subcooling range, as shown in Video 4 in the supporting information. Taking the 20 μm long nanowired surface for example, Figure 3.6 (d) shows the condensation patterns at the $\Delta T \approx 10$ K subcooling condition. The blue and yellow dashed circles show some cases of the Wenzel droplets and the Cassie droplets, respectively. The droplet sweeping starts to replace the coalescence and jumping off manner to remove the condensate. Some coalesced droplets are jumping off from the surface, while some other coalesced droplets form unstable partially-wetting Cassie states and change from partially-wetting Cassie states to Wenzel states and finally are removed by a sweeping manner.

Figure 3.14 shows the complete process of small Wenzel droplets coalescence as shown in (a) to (b), partially-wetting Cassie state droplet formation as shown in (c), and what's more important, the gradual transition of coalesced droplet from partially-wetting Cassie state to Wenzel state on 20μm nanowired surface as shown in (d). The formation of the small Wenzel state droplets results from the coalescence of the condensate in several neighboring gaps between the nanowires. Based on the arrangement of the nanowires, a unit cell can be defined as the triangular spacing formed by three nanowires. As subcooling increases, the nucleate site density on a surface increases as shown in Eq (3.19)[84]:

$$N_s \propto \Delta T^2 \tag{3.19}$$

Under small subcooling conditions, when nucleation occurs in a unit cell, the subcooling in the surrounding unit cells is smaller than that of the nucleation site as we mentioned above. When the subcooling falls in the moderate range at ~10 K, the nucleate site density increases dramatically. Even a 1 K subcooling can result in more than 1000 nucleate sites in a unit cell as shown in Figure 3.14 (e). The result of the interaction with the condensate in the neighboring cells is the formation of the small Wenzel state droplets as shown in Figure 3.14 (f) since the coalescence of the condensate in the neighboring cells can't release enough energy to overcome the resistance force at the three phase contact line (TPCL) under the large roughness factor of our nanowired structures to shrink the droplet contact line. Even when two neighboring Wenzel droplets are at a large enough distance and are large enough in size, the released energy from the coalescence (Figure 3.14 (g)) couldn't result in the shrinking of the contact line of the coalesced droplet due to the large roughness factor *r*.[85] The state change can only result from the shrinking of the contact area of the coalesced droplet on the tips of the nanowires while the liquid in the gaps of the nanowires remains in the structure as shown in Figure 3.14 (h). New liquid-vapor and solid-vapor interfaces form while the liquid-solid interfaces on the tips of the nanowires disappear during this process. The energy to generate the newly exposed interfaces comes from the energy released from

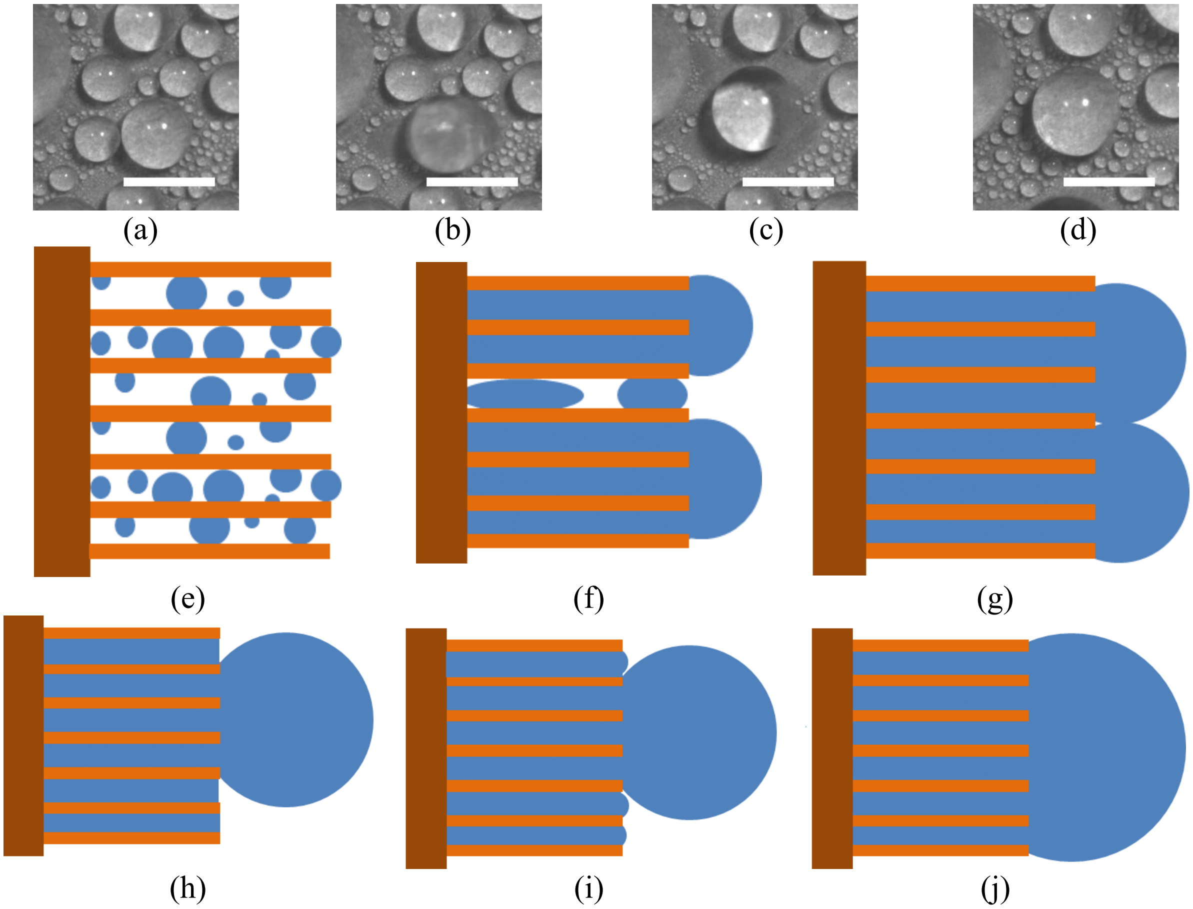

Figure 3. 14 Images and schematics of the process of the Wenzel droplets coalescence and the Cassie to Wenzel state transition after the coalescence at the moderate subcooling on 20 μm long nanowired surface. (a) Two Wenzel droplets before coalescence. (b) Coalescing of two Wenzel droplets. (c) The coalesced droplet first shows Cassie state. (d) The coalesced droplet changes into Wenzel state. (e) Schematic of condensate appears everywhere in the nanowire gaps. (f) Schematic of two Wenzel droplets form and grow. (g) Schematic of the two Wenzel droplets coalescing, which corresponds to Figure 3.8 (a). (h) Schematic of the coalesced droplet shows Cassie state due to a shrink of the contact area and the condensate remains in the gaps of the nanowires, which corresponds to Figure 3.8 (b). (i) Schematic of the condensate in the gaps and the coalesced droplet grow, which corresponds to Figure 3.8(c). (j) Schematic of the coalesced droplet coalesces with the condensate growing out of the gaps and forms a Wenzel state droplet, which corresponds to Figure 3.8 (d). The scale bar is 500 μm for all these images.

the shape transformation of the coalesced droplet. Take the coalescence process shown in Figure 3.14 (a)-(d) as an example. The Gibbs energy needed for new interfaces is

$$\Delta E = \pi\sigma_{lv}(R_0^2 sin\theta_0^2 - R_f^2 sin\theta_f^2)[\varphi cos\theta_{intrinsic} + (1-\varphi)] \qquad (3.20)$$

where R_0 and R_f are the radii of the coalesced droplet at its initial and final states, θ_0 and θ_f are the apparent contact angle of the coalesced droplet at its initial and final states. The released energy between the initial and final states of the coalesced droplet is:[85]

$$\pi\sigma_{lv}\left[2R_f^2\left(1-cos\theta_f\right)-R_f^2 sin\theta_f^2 cos\theta_f\right]+\Delta E=E_0 \tag{3.21}$$

E_0 is the total energy of the newly formed coalesced droplet and can be expressed as:

$$\begin{aligned} E_0 = \pi\sigma_{lv}[2(R_1^2+R_2^2)(1-cos\theta_E)-(R_1^2+R_2^2)sin^2\theta_E cos\theta_E) \\ -72\pi\mu\sqrt{\sigma_{lv}/\rho_w\,(R_1^3+R_2^3)}] \end{aligned} \tag{3.22}$$

The result shows that the contact area of the coalesced droplet on the tips of the nanowires shrinks ~ 60% and the apparent contact angle at the final state is ~ 125°. The contact angle is smaller than the equilibrium contact angle of ~141°, which means the coalesced droplet is in unstable partially-wetting Cassie state and can’t leave the surface. If the length or the solid fraction of the nanowires changes, the surface energy distribution changes accordingly. As long as the initial contact angle of the coalesced droplet is larger than the equilibrium contact angle, based on the surface energy minimization principal, the coalesced droplet can take advantage of the released energy to further shrink the contact area with the structures so that coalescence induced jumping might occur. Otherwise, if the initial contact angle is smaller than the equilibrium contact angle, the contact angle of the coalesced droplet will end up with the equilibrium contact angle. Calculation has been carried out based on Eq. (3.20)-(3.22) with the length and the solid fraction of the nanowires as variables. The results have been shown in Figure 3.15 (a) and (b). The initial contact angle of the coalesced droplet increases with the decrease of the nanowire length. However, even when the nanowires are as short as 1 μm, the initial contact angle is still way lower than the equilibrium contact angle. As the solid fraction increases, the initial contact has very limited increase and is way lower than the equilibrium contact angle. Thus, once Wenzel state droplet appears on the condensation surfaces, coalescence induced jumping can’t occur any more. As the condensation process continues, the liquid that remains in the gaps of the nanowires grows out of the tips of the nanowires and, in the meantime, the unstable partially-wetting Cassie state droplet also transforms towards its equilibrium state as shown in Figure 3.14 (i). Once the liquid growing out of the nanowire tips and contacts with the droplet above it, the release energy can’t generate new interfaces and the droplet thus changes into Wenzel state again as shown in Figure 3.14 (j). The droplets in Wenzel state can only be removed by a sweeping manner. As long as the droplets before coalescence are in Wenzel state, the contact angle of the coalesced droplet will never exceed the equilibrium contact angle no matter what are the heights and solid fractions of the surface structures. According to Rose’s study,[86] once the smallest viable droplet radius reaches 2 nm, the nucleation sites saturate at some locations on the flat surface. Compared with ~2 nm radius nucleation site, the nanowires in our structures can be regarded as flat surface so that Rose’s standard holds for our structured surfaces. Once the nucleation site saturate on the surface, Wenzel state droplets form inevitably. Transition thus occurs consequently. Since the transition doesn’t occur suddenly on the entire surface, the

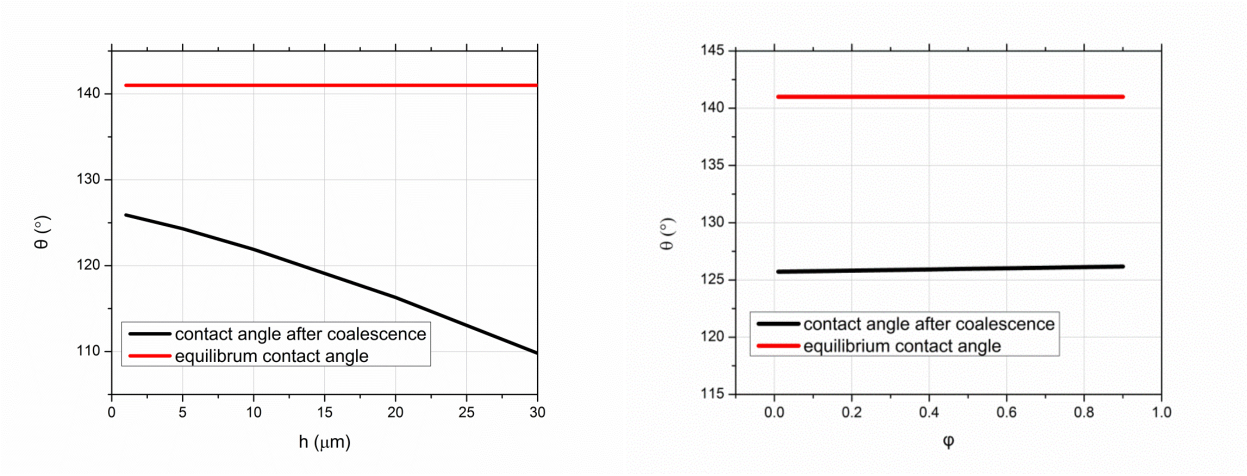

a b

Figure 3. 15 Initial contact angle of the coalesced droplet as a function of (a) the length and (b) the solid fraction of the nanowires

condensation heat transfer performance degrades gradually as the transition progresses with the increase of the subcooling.

When transition ends at ΔT~15 K, the condensation heat transfer performance is the same on all four surfaces. This is the flooding region. In Figure 3.6 (e), the typical large subcooling condition is selected to be $\Delta T \approx 27$ K. The image shows that stable Wenzel droplets cover the surfaces under this subcooling and the droplet sweeping is the only manner to remove the condensate as shown in the purple circle. The droplets' growth, coalescence and the sweeping removal on nanowired surface is similar to that on the smooth surface under the similar large subcooling, as shown in Figure 3.6 (a). Due to the Wenzel wetting state of the droplets, the nanowire structures are filled by condensate. There is a nanowire-condensate mixed layer between the bottom of the droplets and the substrate. This layer can be regarded as an effective thermal resistance which is the result of the thermal resistance of the nanowires and the condensate in parallel. Due to the high effective thermal conductivity of the nanowires, only 0.08 K temperature drop can result from the mixed layer for the 20 μm long nanowired surface at the 150 kW/m^2 heat flux condition. Therefore, the thermal resistance resulting from the nanowire structure is only a minor factor, especially for the large subcooling condition. Since all the nanowires are flooded, the heat transfer occurs mainly at the liquid-vapor interface. Therefore the condensation heat transfer performance is similar on all surfaces including nanowired surfaces and the smooth surface due to the similar droplet growth, coalescence and departure on nanowired surface and the smooth surface.

Chapter 4 Pool Boiling Heat Transfer Enhancement

4.1 Sample characterizations

A plain Cu surface with nominal surface roughness of 450 nm was prepared by polishing 0.8 mm thick Cu sheet with a 2000-grit sand paper and tested for pool-boiling heat transfer as the reference. Two micropillared Cu surfaces as shown in Figure 4.1(a) and (b) with 20 μm × 20 μm pillars at a pitch of 100 μm and a height of 14 μm (as shown in Figure 4.1(a)) and 45 μm × 45 μm at a pitch of 200 μm and a height of 32 μm (as shown in Figure 4.1(b)) were fabricated. The two Cu nanowired surfaces with a length of 4.7 μm and 27 μm were fabricated through a two-step porous anodic alumina (PAA) template-assisted electrodeposition method. As shown in Figure 4.1(c) and (d), most of the 4.7 μm long Cu nanowires are standing alone while the 27 μm long Cu nanowires accumulate together to form nanowire bundles. The average gap size in the 4.7 μm long Cu nanowire arrays is 200 nm. A wide range of size of gaps from 600 nm to 4 μm exists between the nanowire bundles in the 27 μm long Cu nanowire arrays. An even wider range of cavities is shown in the inserted image in Figure 4.1(d) due to the uneven lengths of the nanowires. As shown in Figure 4.1(e) and (f), the hierarchical nano/microstructured surface has micropyramids made of Cu nanowires with a height of about 33 μm and a pitch of 100 μm. The nanowires in the valley between micropyramids with a height of about 16μm form tightly tangled bundles with an average effective diameter of 9 μm and an average gap size of 2 μm, which owns abundant active nucleation sites ranging from 600 nm to 6 μm throughout the superheat range in the test.

Due to the capillary force generated by the structures on the surface, the contact angle on the structured surface changes with the propagation of the vapor-liquid-solid three phase contact line. The static contact angle is finally achieved until the viscous force balances with the capillary force.[87] This dynamic process provides not only the contact angle but also the liquid spreading

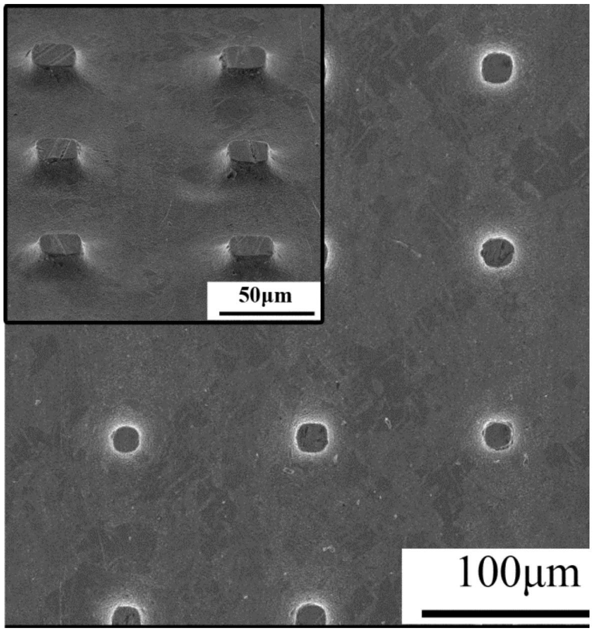
50µm
100µm

a

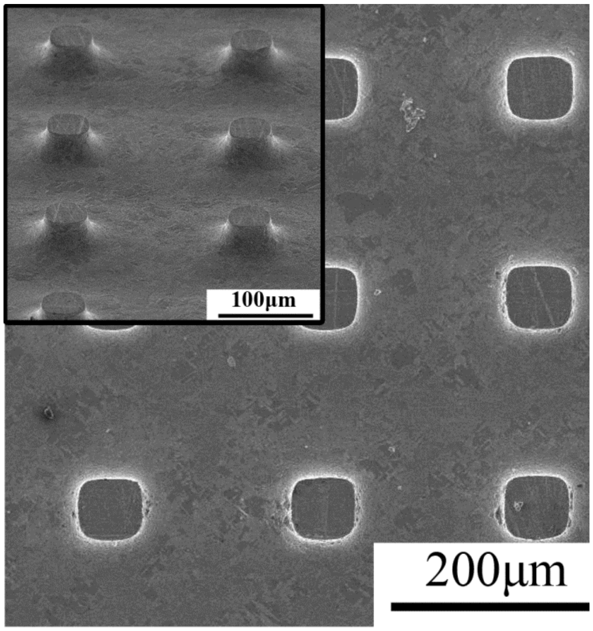
100µm
200µm

b

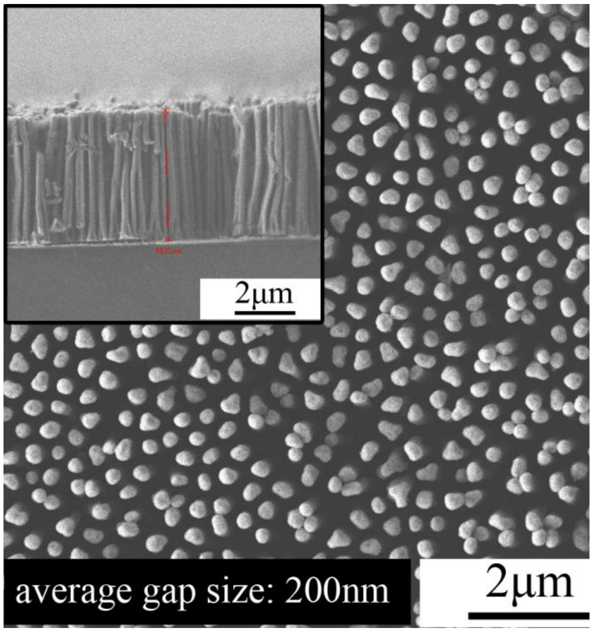
2µm
average gap size: 200nm
2µm

c

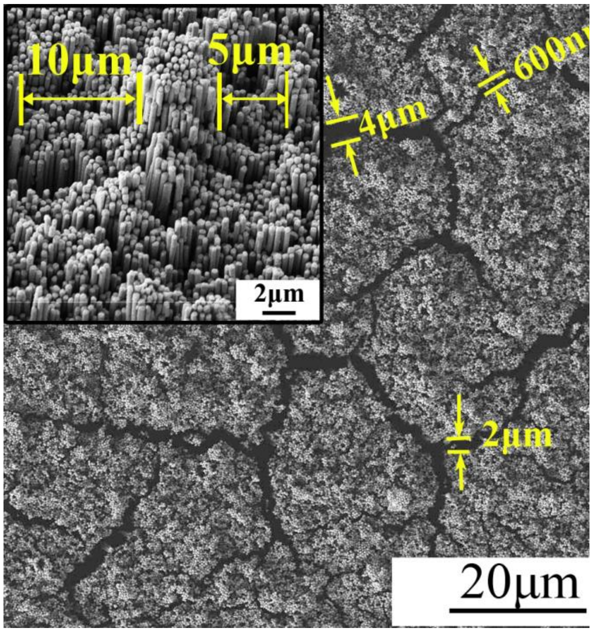
10µm
5µm
2µm
4µm
600n
2µm
20µm

d

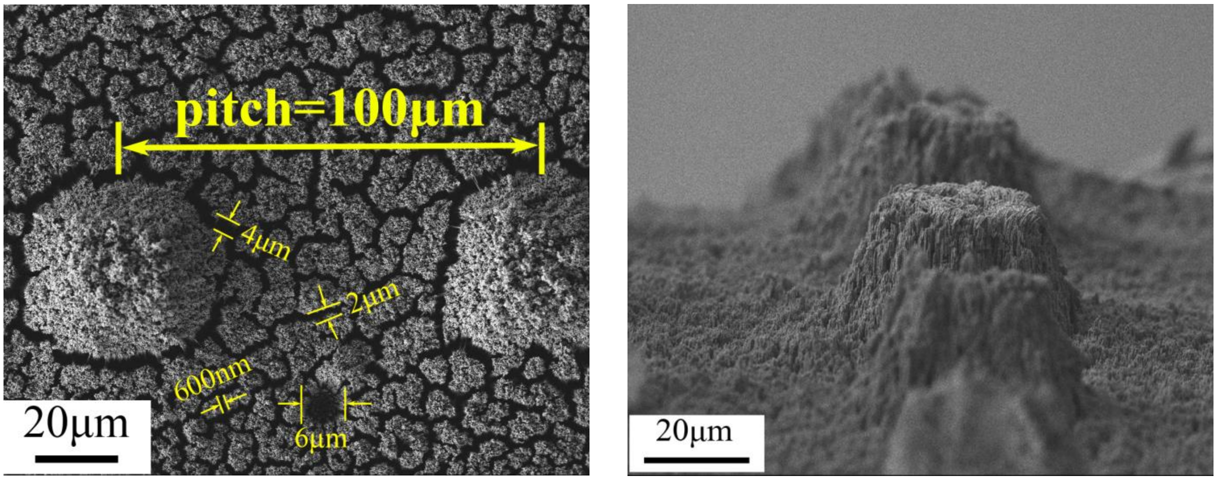

e f

Figure 4. 1 Surface morphology of the as-obtained samples . (a) top view Scanning-Electron-Microscope (SEM) image of the 20μm×20μm micropillared Cu surface and the inset is the tilted view SEM image. (b) top view SEM image of the 45μm×45μm micropillared Cu surface and the inset is the tilted view SEM image. (c) top view SEM image of the 4.7μm long Cu nanowired surface and the inset is the cross-section view. (d) top view SEM image of the 27μm long Cu nanowired surface with a wide spectrum of gaps and the inserted image is the tilted angle view. (e) top view and (f) side view SEM photos of the hierarchical structured surface.

or wicking performance of the structured surfaces. The recording of this dynamic process is helpful to extra useful information to understand the characterizations of the structured surfaces.

The contact angles on the testing surfaces are measured before the heat transfer experiments by sessile drop method with a high speed camera under room temperature and atmospheric pressure. The testing system as shown in Figure 4.2 consists of a high speed camera working at 1000 frame per second (fps), a syringe that can deliver 0.5—25 μL water droplet, a micro-translation stage for the sample, a ground glass light diffuser, and a 250 W halogen lamp that can provide enough light for the camera under high speed shooting condition.

The tip of the syringe is kept 4 mm above the testing surface to eliminate the effect of the different kinetic energy of the water droplet which can result in impact on the spreading behavior of the liquid on the surface.[88] 10 to 11 μL DI water is used to realize the dynamic process. The amount of the DI water is chosen based on the bond number of the droplet so that gravity won't affect the shape of the droplet on the surface. The diameter of the 11 μL DI water droplet is ~ 2.7 mm. Based on the free falling body movement of the droplet after leaving the tip of the syringe, the velocity of the droplet before contacting with the surface is ~0.16 m/s. Thus the bond number of the droplet can be calculated as:

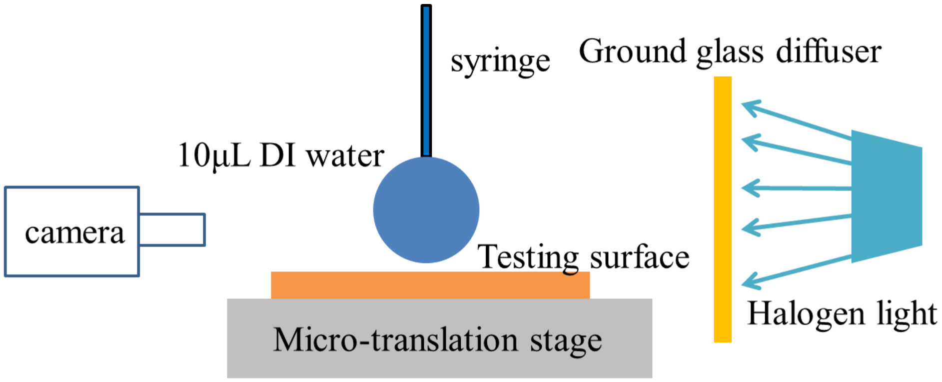

Figure 4. 2 Schematic of the contact angle testing system

$$Bo = \frac{\rho_w g D^2}{\sigma} \tag{4.1}$$

where ρ_w is the density of water, σ is the surface tension of the water, g is the gravitational acceleration, and D is the diameter of the droplet. In our study, $Bo \approx 0.9 < 1$ so that gravity has no effect on the shape of the water on the surface which is a sphere cap (part of a sphere).[89] Whether the liquid spreading on the structured surface is driven by the capillary force depends on two dimensionless numbers which are the Weber number (*We*) and the Ohnesorge number (*Oh*):

$$We = \frac{\rho_w D U^2}{\sigma} \tag{4.2}$$

$$Oh = \frac{\eta}{\sqrt{D\sigma\rho_w}} \tag{4.3}$$

where U is the speed of the droplet right before contact, η is the dynamic viscosity of water. In this study, $We \approx 0.91 < 1$ and $Oh \approx 0.002 \ll 1$. The liquid spreading after the droplet contacting with the surface can be regarded as almost inviscid and capillarity driven flow.[90] Therefore, the information about liquid spreading on the structured surface can be obtained.

The liquid spreading performance on the structured surface is represented by the volume rate of water sucked by the structure under capillary force. The calculation of the water volume sucked by the structure can be realized by subtracting the volume of the water sphere cap on the surface from the initial volume of the water droplet before contact. The volume of the water sphere cap as shown in Figure 4.3 is

$$V_{sc} = \frac{1}{3}\pi R_{sc}^3(2 - 3cos\theta + cos^3\theta) \tag{4.4}$$

where R_{sc} is the radius of sphere cap and θ is the contact angle of the sphere cap. R_{sc} can be calculated based on the contact angle and the length of the contact line

$$R_{sc} = \frac{b}{2sin\theta} \tag{4.5}$$

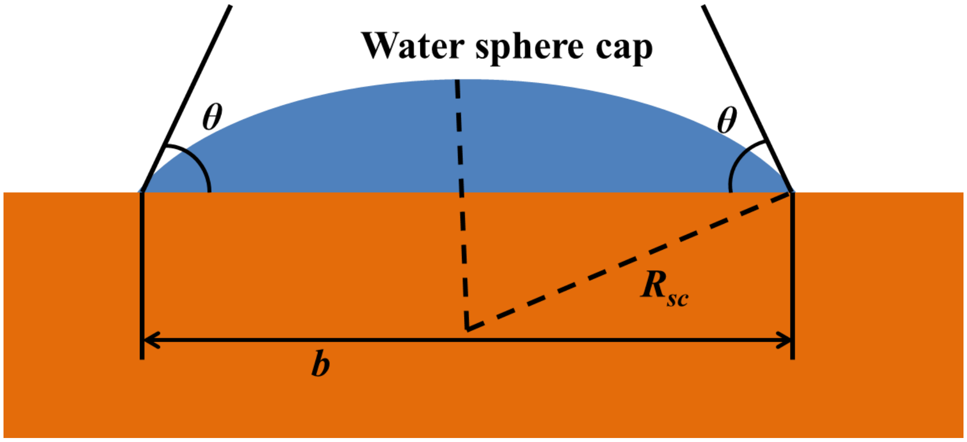

Figure 4. 3 Schematic of the contact angle, contact line, and the radius of the water sphere cap

Once the water droplet is realized onto the structured surface, the contact angle decreases from 180° at the beginning of the contact until the static contact angle is achieved. A typical series of photos of this dynamic process from the recording of the high speed camera is shown in Figure 4.4. As we can see from the process, at the beginning of the contact, the shape of the liquid on the surface is not sphere cap and the outline of the liquid can’t be obtained. Due to the oscillation of the outline of the water sphere cap resulted from the kinetic energy and the surface tension of the water droplet, the volume of the water sphere cap can’t be measured. The fluctuation of the dynamic contact angle in Figure 4.5 is the result of the oscillation. Since

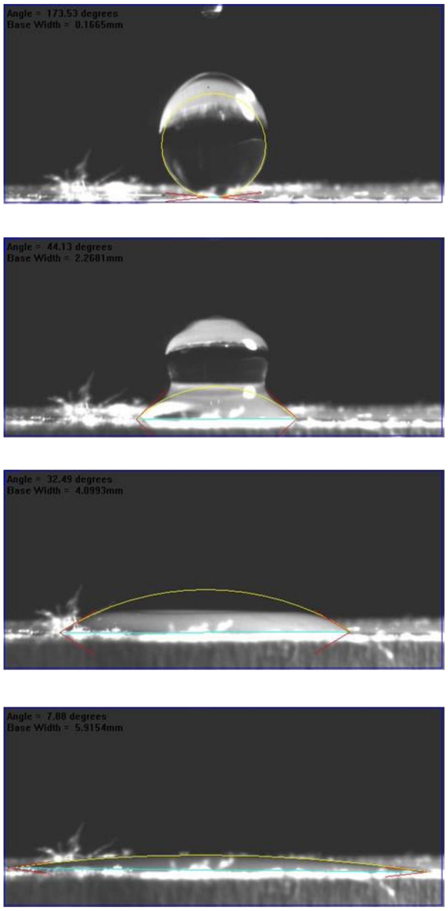

Figure 4. 4 Dynamic process of a water droplet contacting with structured surface

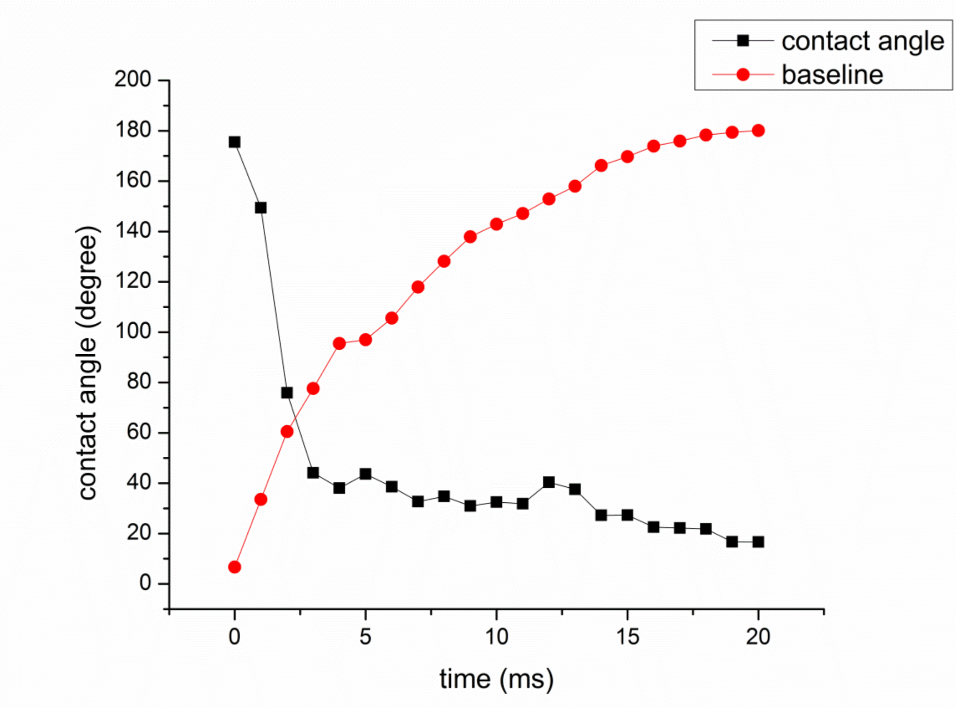

Figure 4. 5 Relation between time and contact angle or the length of the contact line

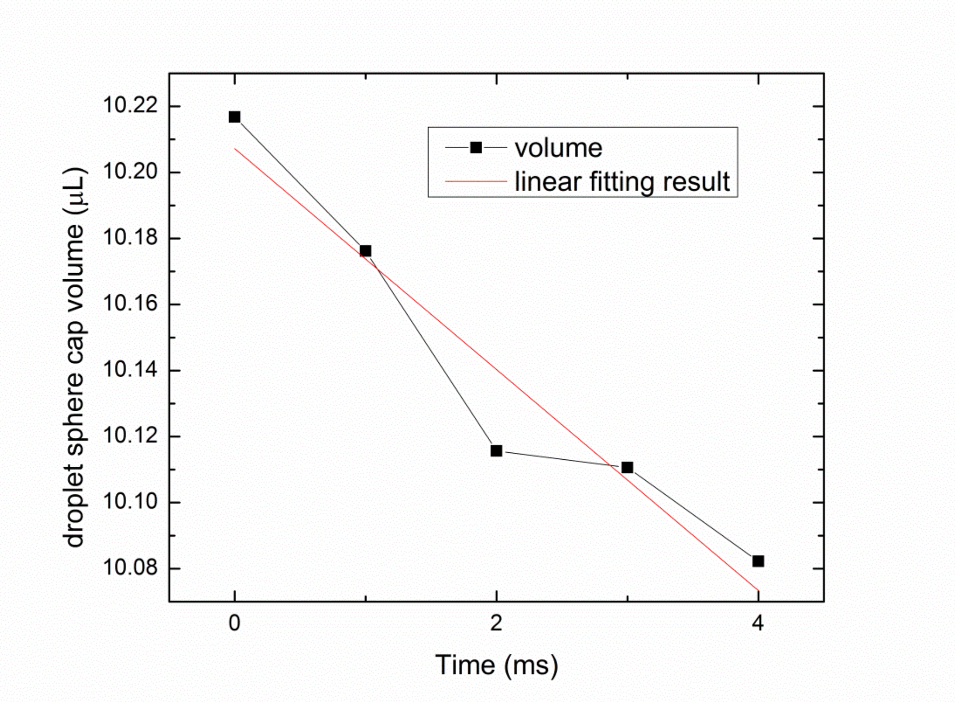

Figure 4. 6 Relation between time and volume and linear fitting result

viscous diffusion exists, the oscillation is underdamped oscillation. The time scale for the decay is[90]

$$\tau = \frac{0.035D^2}{\nu} \tag{4.6}$$

where ν is the kinematic viscosity. The oscillation damps away after ~ 250 ms in our study. What's more important, the length of the contact line stops changing after ~20 ms as shown in Figure 4.5, which coincides with the conclusion from ref 90 on smooth surface. Although the length of the contact line stops changing, the contact angle keeps deceasing after that time point, which indicates that from then on the reduction of the sphere cap volume is the only result of the liquid spreading resulted from the capillary force. Therefore, the volume changing rate resulted from the capillary force can be calculated by using the points after 250 ms. The length of the contact line is calculated by comparing the length of the contact line in the photos with the width of the syringe which is 0.55 mm in the photos. Since the time scale for bubble generation before departure is ~ 5 ms,[33] the volume changing rate is obtained by linear fitting the time-volume relation in a 5 ms range as shown in Figure 4.6. The results of the static contact angles and the liquid spreading performance which is the volume changing rate on our testing samples are listed in Table 4.1 and 4.2, respectively.

Table 4.1. Contact angle measurement results

plain Cu surface	89.5°
20μm×20μm Cu micropillared surface	23.4°
45μm×45μm Cu micropillared surface	31°
surface with 4.7μm long Cu nanowires	28.7°
surface with 27μm long Cu nanowires	18.6°
nanowire/micropillared hierarchical structured surface	5.1°

Table 4.2. Water spreading performance on different structured surfaces

20μm×20μm Cu micropillared surface	43.73 μL/s

45µm×45µm Cu micropillared surface	33.47 µL/s
surface with 4.7µm long Cu nanowires	16.02 µL/s
surface with 27µm long Cu nanowires	26.94 µL/s
nanowire/micropillared hierarchical structured surface	48.61 µL/s

4.2 Testing system and data reduction

4.2.1 Testing system

The pool boiling heat transfer experiments were conducted in an open system using steady state method. Figure 4.7 (a) shows the schematics of the pool boiling testing system which was adapted from reference 91. An aluminum vessel with a diameter of 19 cm and a depth of 22 cm holds deionized (DI) water with two guard-heaters outside to keep the DI water saturated. Two thermocouples, TC4 and TC5, were placed about 5mm above the boiling surface to monitor the saturated temperature of the DI water. A non-porous ceramic was mounted in the vessel as the thermal insulation material. An oxygen-free Cu bar with 8mm×8mm square top surface was used to conduct heat from the Cu cylinder at the bottom to the sample on the top. The 0.8 mm thick heat transfer surfaces prepared as described in Supporting Information section1 were cut into 8 mm × 8 mm squares and then soldered onto the top of the Cu bar. A photo of the assembly of the sample is shown in Figure 4.7 (b).Three K-type thermocouples, TC1, TC2, and TC3, were soldered into the center of the Cu bar for the temperature and the heat flux measurements. TC1 was placed 1 mm below the top surface of the Cu bar and the distance between each two adjacent thermocouples was 8 mm. Heat was provided by the main heater which was clamped to the Cu cylinder.

The steady state measurement method[92, 93] was used to test the pool boiling performance of all the samples under atmospheric pressure. The DI water was boiled for at least two hours to remove the dissolved gas in the water before it was added to the vessel. During the testing, the DI water was kept saturated. Heat supplied to the sample started from around 1 W/cm^2 and was increased until CHF was reached. The increment of heat supplied was around 20 W/cm^2 at the beginning and about 5 W/cm^2 when it was close to the CHF. When the temperature fluctuation of TC1 in a 10-minute period was not greater than 0.2 °C under a given heat flux, we regarded this as one steady state and recorded the temperatures for a 3-minue period using an Agilent 34980A data acquisition system (more than 200 data points were recorded to take an average).

4.2.2 Data reduction

The temperature differences between the adjacent thermocouples are similar to each other in all tests. A typical relation between the temperature differences and the heat flux from the boiling heat transfer experiment on the surface with 27μm long Cu nanowires is shown in Figure 4.8.

Thus, the heat loss from the Cu bar through the insulating ceramics is negligible and one-dimensional heat conduction can be used to calculate the heat flux and the surface temperature.

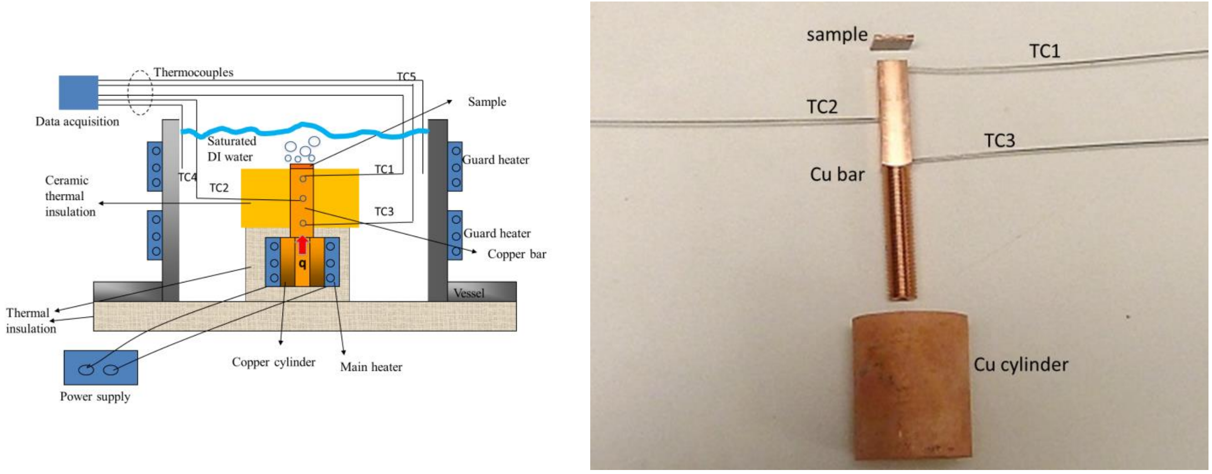

a b

Figure 4. 7 (a) Schematic of the open system for pool boiling measurement and (b) photo of the assembly of the sample

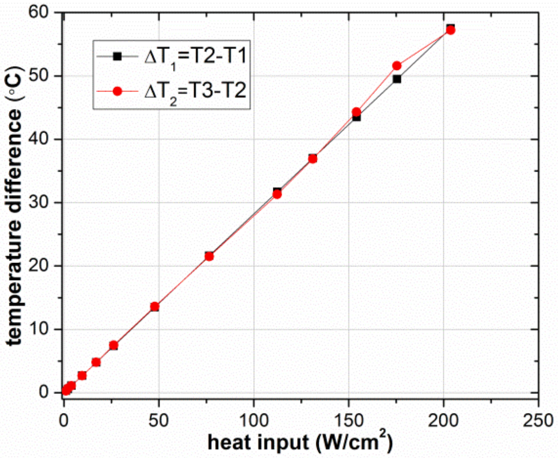

Figure 4. 8 A typical relation between the temperature differences and the heat flux on the surface with 27μm long Cu nanowires

The heat flux q'' conducted by the Cu bar is

$$q'' = K_{Cu}(T_{TC2} - T_{TC1})/t_{TC} \tag{4.7}$$

In Eq. 4.7, K_{Cu} is the thermal conductivity of the oxygen-free Cu, with a value of 401 W/m K, and t_{TC} is the distance between two neighboring thermocouples in the Cu bar.

The surface temperature is then extrapolated by the one dimensional heat conduction model using T1 and the heat flux in the Cu bar. Since all the Cu samples were soldered onto the top of the Cu bar, an interface thermal resistance was introduced by the solder layer. We have repeatedly calibrated the interface thermal resistance to obtain a value of R_{ITR}=0.085825 *K/W*, which has been taken into account when obtaining the surface temperature of the sample.

The wall temperature T_w can be calculated as

$$T_W = T_{TC1} - q''(t_{sTC1}/K_{Cu} + R_{ITR}) \tag{4.8}$$

The heat transfer coefficient h_{eff} then can be calculated as

$$h_{eff} = q''/(T_W - T_{sat}) \tag{4.9}$$

In Eq. 4.8 and Eq. 4.9, t_{sTC1} is the total thickness between the top surface of the sample and TC1, and T_{sat} is the saturated temperature of the DI water.

We have employed the error propagation method to estimate the uncertainty of the experiment. All three equations can be written in the form of $y=f(x_i)$. The error (when only first order items of Taylor expansion are considered) then can be expressed as

$$\sigma^2(y) = \sum_{i=1}^{n} (\frac{\partial f}{\partial x_i})^2 \sigma_{x_i}^2 + 2\sum_{i=1}^{n-1} \sum_{j=i+1}^{n} \frac{\partial f}{\partial x_i}\frac{\partial f}{\partial x_j} \sigma_{x_i}\sigma_{x_j}\rho_{i,j} \tag{4.10}$$

where $\rho_{i,j}$ is the correlation coefficient between x_i and x_j. We assumed that all the variables in Eq. 4.7—Eq. 4.9 were correlated, which means $\rho_{i,j}=1$, so that the errors obtained were all at their maximum values. The equation for error calculation transformed into

$$\sigma_{max}(y) = \sum_{i=1}^{n} \left|\frac{\partial f}{\partial x_i}\right| \sigma_{x_i} \tag{4.11}$$

Based on Eq. 4.11 the uncertainties of the superheat, the heat flux, and the heat transfer coefficient are expressed as

$$\sigma_{max}(T_W - T_{sat}) = \sigma(T_{sat}) + \sigma(T_{TC1}) + \left(\frac{t_{sTC1}}{K_{cu}} + R_{ITR}\right)\sigma(q'') + \frac{q''}{K_{Cu}}\sigma(t_{sTC1}) \tag{4.12}$$

$$\sigma_{max}(q'') = \frac{K_{Cu}}{t_{TC}^2}(T_{TC2} - T_{TC1})\sigma(t_{TC}) + \frac{K_{Cu}}{t_{TC}}\sigma(T_{TC2}) + \frac{K_{Cu}}{t_{TC}}\sigma(T_{TC1}) \tag{4.13}$$

$$\sigma_{max}(h_{eff}) = \frac{1}{T_W - T_{sat}}\sigma(q'') + \frac{q''}{(T_W - T_{sat})^2}\sigma(T_W) + \frac{q''}{(T_W - T_{sat})^2}\sigma(T_{sat}) \tag{4.14}$$

The uncertainty of the temperature is ±0.2 °C, which was estimated from the largest temperature fluctuation of the measurement of the temperature during the steady state. The uncertainties of the thickness measurement and the positioning of the thermocouples were 0.005 mm, and 0.005 mm respectively, which were estimated from the accuracy of the caliper. The uncertainties of the superheat, the heat flux, and the HTC can be calculated accordingly under each heat input and be presented in the boiling curves and the relations between heat flux and HTC.

4.3 Testing results

Figure 4.9 shows the pool boiling curves (heat flux q v.s. superheat T_w-T_{sat}) on the hierarchical structured surface, two micropillared surfaces, and two nanowired surfaces in comparison with that on plain surface. The CHFs on the hierarchical structured surface, the 20 μm×20 μm micropillared surface, the 45 μm×45 μm micropillared surface, the 4.7 μm long nanowired surface, and the 27 μm long nanowired surface are 248.8 W/cm^2, 234 W/cm^2, 195.6 W/cm^2, 161.9 W/cm^2, and 203.7 W/cm^2 respectively while the CHF on the plain surface is 140.3W/cm^2. As expected the hierarchical structured surface has the best enhancement in terms of CHF which is ~ 77% higher than that on the flat surface. However, the micro structured surfaces have better CHF enhancement than that of the nanowired surfaces, which is unexpected before the experiments. Figure 4.10 (a) and (b) compare the relation between the CHF and the contact angles and the relation between the CHF and the water spreading speed. Figure 4.10 (a) shows that the relation between the CHF and the contact angle is not monotonic, as described in Kandlikar's model[47] when the contact angle is smaller than 30°. Apparently, contact angle is not

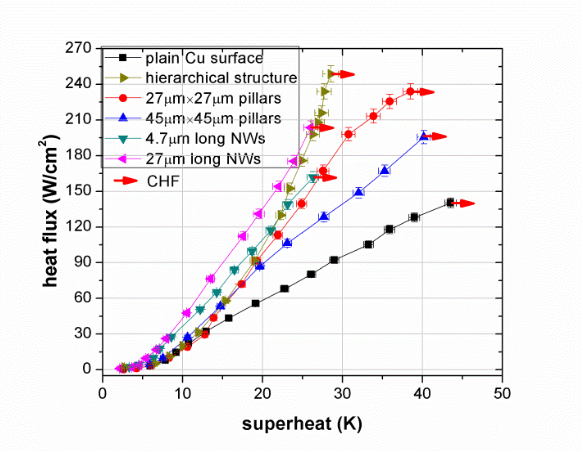

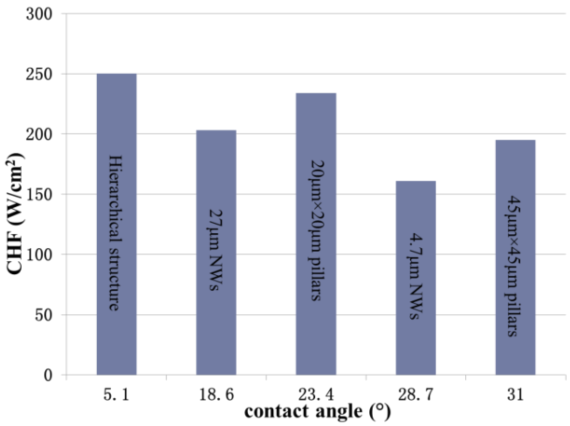

Figure 4. 9 Pool boiling curves on all the structured surfaces in comparison w/ that of the plain Cu surface.

Figure 4. 10 (a) Relation between contact angle and CHF

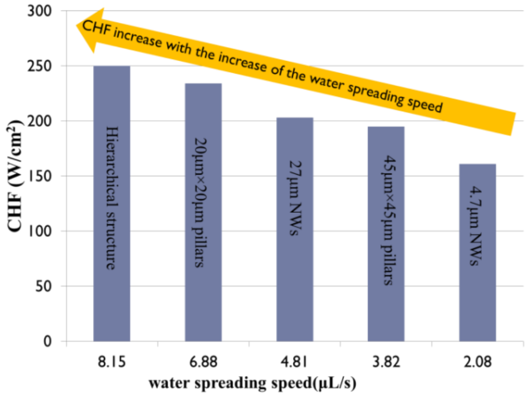

Figure 4. 10 (b) Relation between water spreading and CHF

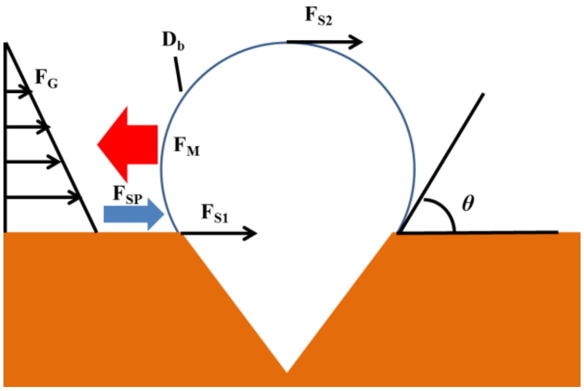

Figure 4. 11 Force analysis on the vapor-liquid interface of a bubble

the only factor influencing the CHF. Figure 4.10 (b) shows that the CHF changes with the water spreading speed monotonically.

4.4 Discussions

It is reasonable to assume that the mechanism for the CHF to occur is still the force balance on the bubble interface but the heat flux is tuned by the liquid spreading. Ahn[51] proposed to add the spreading effect to Kandlikar's model to modify the CHF prediction as shown in the following equation:

$$q''_{CHF} = q''_{CHF\_Kandlikar} + q''_{spreading}$$

$$= sh_{fg}\rho_g^{1/2}\left(\frac{1+cos\theta}{16}\right)[\frac{2}{\pi}+\frac{\pi}{4}(1 + cos\theta)cos\varphi]^{1/2}[\sigma g(\rho_l-\rho_g)]^{1/4} + \frac{d\Phi}{dt}\frac{\rho_l h_{fg}}{A_{heating\_surface}} \tag{4.15}$$

where h_{fg} is the latent heat of water, ρ_g and ρ_l are the density of the water vapor and the water, θ is the apparent contact angle, φ is the angle of the heating surface with respect to the horizontal plane, σ is the surface tension, Φ is the volume of the water that spreads into the structures, $A_{heating\_surface}$

is the area of the heating surface, and s is a coefficient by fitting the experiment data. Since the liquid spreading plays an important role in pool boiling heat transfer and determining the CHF, the wettability effect on CHF will be attenuated when the contact angle is smaller on structured surfaces. $d\Phi/dt$ represents the water spreading speed. Eq. 4.15 mentioned above introduced the effect of liquid spreading and showed that the predicted data could match the experimental data. However, Eq. 4.15 didn't explain how the liquid spreading affects the CHF fundamentally. Since Kandlikar's model was based on the force analysis on the vapor-liquid interface of a bubble before CHF, the liquid spreading that delays the CHF must apply certain force onto the interface. The capillary force drives the liquid to flow to the bubble. The liquid flow imposes resistance force on the interface to prevent the interface from spreading out. Thus, the force from the liquid spreading works the same way as the surface tension to hold the interface against the moment resulted from the vaporization. To introduce the effect of liquid spreading, a force analysis is given as shown in Figure 4.11. The force balance on the vapor-liquid interface of a bubble is

$$F_M = F_{S1} + F_{S2} + F_G + F_{SP} \tag{4.16}$$

where F_M resulted from the change in moment as vapor leaves the interface is the driving force for the interface to expand, F_{S1} and F_{S2} are the surface tension, F_G is the force due to gravity, and F_{SP} is the force imposed by liquid spreading. Since the liquid spreading or the liquid volume changing rate is known from the spreading tests, F_{SP} can be deducted as

$$F_{SP} = \dot{m}v = \rho_l \frac{d\Phi}{dt} v \tag{4.17}$$

where $\dot{m}$ is the liquid mass flow rate, v is the liquid spreading speed or the speed of the liquid front, and ρ_l is the liquid density. When a liquid droplet contacts a structured surface, the liquid spreads radically.[94] The liquid spreading speed that is related to the volume change can be expressed as:

$$v = \frac{2}{\pi h D}\frac{d\Phi}{dt} \tag{4.18}$$

where h is the height of the structure and D is the diameter of the liquid front. Plug Eq. (4.18) into Eq. (4.17) and set the diameter in Eq. (4.18) as the effective diameter of the bubble, the force generated by liquid spreading is

$$F_{SP} = \rho_l \frac{d\Phi}{dt}\frac{2}{\pi h D}\frac{d\Phi}{dt} = \frac{2\rho_l}{\pi h D}(\frac{d\Phi}{dt})^2 \tag{4.19}$$

Based on Kandlikar's analysis[47] and the bubble geometry, the force generated from the vaporization, the surface tensions, and the gravity force can be expressed as:

$$F_M = (\frac{q_I''}{h_{fg}})^2 \frac{1}{\rho_v} H_b \tag{4.20}$$

$$F_{S1} = \sigma_{lv} cos\theta \tag{4.21}$$

$$F_{S2} = \sigma_{lv} \tag{4.22}$$

$$F_G = \frac{1}{2} g(\rho_l - \rho_v) H_b^2 \tag{4.23}$$

where h_{fg} is the latent heat, ρ_v is the vapor density, g is the gravitational acceleration, q_I'' is the heat flux on the interface, and H_b is the height of the bubble which can be expressed as

$$H_b = \frac{D_b}{2}(1 + cos\theta) \tag{4.24}$$

D_b is the effective diameter of the bubble and was set to be

$$D_b = \pi[\frac{\sigma_{lv}}{g(\rho_l - \rho_v)}]^{1/2} \tag{4.25}$$

Plug Eq. (4.19) and Eq. (4.21)-(4.25) into Eq. (4.20), we get

$$
\begin{aligned}
q_I'' &= h_{fg}[\frac{\rho_v}{H_b}\sigma_{lv}(1+cos\theta)+\frac{1}{2}\rho_v g(\rho_l-\rho_v)H_b+\frac{\rho_l\rho_v}{\pi h D_b H_b}(\frac{d\Phi}{dt})^2]^{1/2} \\
&= h_{fg}\rho_v^{1/2}[\frac{2}{\pi}+\frac{\pi}{4}(1+cos\theta) \\
&+ \rho_l\sqrt{\frac{g(\rho_l-\rho_v)}{\sigma_{lv}^3}}\frac{1}{1+cos\theta}\frac{2}{\pi^3 h}(\frac{d\Phi}{dt})^2]^{1/2}[\sigma_{lv}g(\rho_l-\rho_v)]^{1/4}
\end{aligned}
\qquad (4.26)
$$

Thus the CHF can be calculated as:

$$
\begin{aligned}
q_{CHF}'' &= \frac{(1+cos\theta)}{16}q_I'' \\
&= \frac{(1+cos\theta)}{16}h_{fg}\rho_v^{1/2}[\frac{2}{\pi}+\frac{\pi}{4}(1+cos\theta) \\
&+ \rho_l\sqrt{\frac{g(\rho_l-\rho_v)}{\sigma_{lv}^3}}\frac{1}{1+cos\theta}\frac{2}{\pi^3 h}s(\frac{d\Phi}{dt})^2]^{1/2}[\sigma_{lv}g(\rho_l-\rho_v)]^{1/4}
\end{aligned}
\qquad (4.27)
$$

Since the real height of the liquid front is not known, a coefficient *s* is added to the liquid spreading item. The coefficient can be obtained by fitting the experiment data with Eq. (4.27).

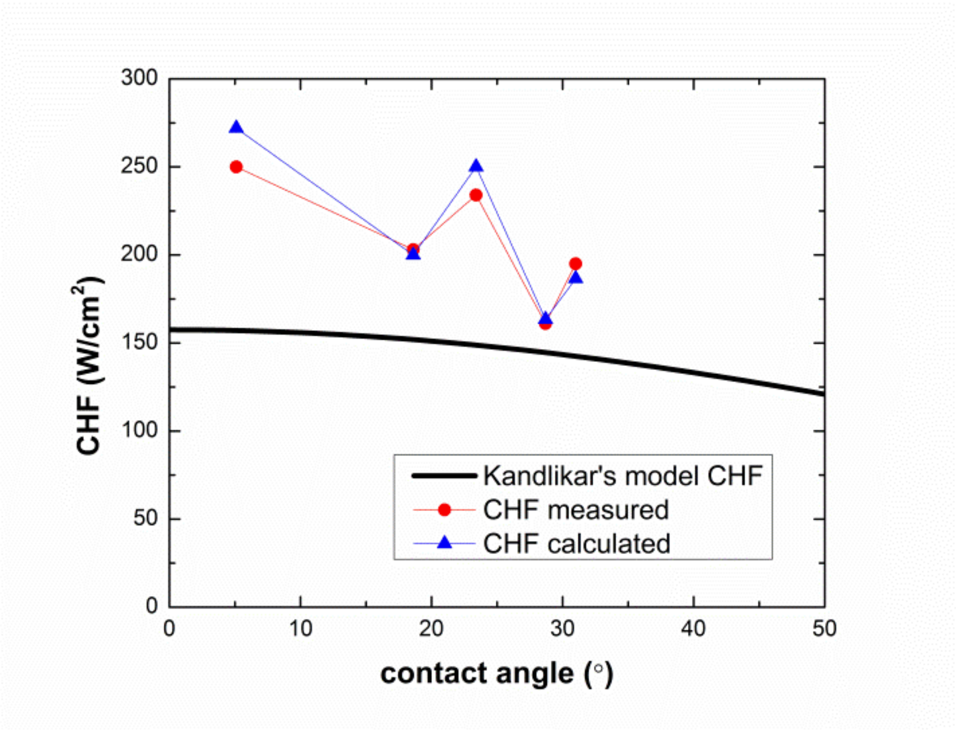

Figure 4. 12 Comparison of model predictions and experiment data

The CHFs have been calculated based on the modified model (Eq. 4.27) with our tested spreading speed and the contact angles and compared with Kandlikar's model, as shown in Figure 4.12. The modified model clearly predicts the trend of the CHF with the change of the contact angles and the spreading speed in our tests. With this non-monotonic relation and a wider range of contact angles, the effect of liquid spreading on CHF is well clarified. Small contact angle together with fast liquid spreading deliver the highest CHF on the hierarchical structured surface.

The HTC in pool boiling is closely related to the superheat level, the specific surface structures, and surface conditions (contact angle *etc*.). In general, researches have been focused on the relation between the heat flux and bubble dynamics such as the bubble release frequency and the bubble departure diameters.[49, 50] The previous study of bubble dynamics highly depends on the observation of the boiling process with high speed camera. However, due to the relation between the water supply and the bubble dynamics, the heat flux can be also estimated by studying the liquid spreading and heating process without the help of a high speed camera. Kim[49] reviewed the heat transfer modes in pool boiling. The most important two heat transfer modes are the intensive evaporation (latent heat) at the micro-layer region which is a liquid layer about 10^{-7}~10^{-8} m[50] thick underneath the bubble close to the three phase line and the liquid superheating process (sensible heat) at an active nucleate site as shown in Figure 4.13. Heat dissipated from the heated solid surface first heats the liquid from the saturated temperature to a superheated level before CHF occurs and then further heats the superheated liquid to superheated vapor by evaporation. The heated and evaporated liquid mass comes from the liquid delivered by the surface structures to the active nucleate sites. The liquid spreading speed on the surface is therefore directly related to the heat flux at an active nucleate site. The heat flow at one active nucleate site based on the evaporation is

$$q''_{evp} = \dot{m}h_{fg} = \rho_l \frac{d\Phi}{dt} h_{fg} \tag{4.28}$$

where $\dot{m}$ is the water mass flow rate to the active nucleate site. The heat absorbed by the liquid to be heated to a certain superheat level is

$$q''_{superheat} = \dot{m}C_p \Delta T_{sat} = \rho_l \frac{d\Phi}{dt} C_p \Delta T \tag{4.29}$$

where C_p is the specific heat of water and ΔT is the superheat that is the difference between the temperature of the heated surface and the saturated water T_{sat}. The total heat flux on a surface is:

$$q'' = N_a(q''_{evp} + q''_{superheat}) = N_a \rho_l \frac{d\Phi}{dt} (h_{fg} + C_p \Delta T) \tag{4.30}$$

where Na is the active nucleate site density. The active nucleate site density Na is determined by the surface structure, the superheat, and influenced by the contact angle. [95,96] The active nucleate site density is proportional to the inverse of the square of the critical cavity mouth radius R as:

$$Na \sim R^{-2} \tag{4.31}$$

where the critical cavity mouth radius R is proportional to the inverse of the square of the superheat ΔT [97] as:

$$R = \frac{2\sigma T_{sat}}{\rho_g h_{fg} \Delta T} \tag{4.32}$$

Substituting Eq.(4.32) into Eq. (4.31), the active nucleate site density is proportional to the square of the superheat as:

$$Na \sim C_1 \Delta T^2 \tag{4.33}$$

C_1 is a constant and chosen to be 0.034.[98] Substituting Eq.(4.33) into Eq. (4.30), the heat flux that includes the effect of the liquid spreading is then:

$$q'' = N_a \rho \frac{d\Phi}{dt} \left(h_{fg} + C_p \Delta T\right) = 0.034 \Delta T^2 \rho \frac{d\Phi}{dt} \left(h_{fg} + C_p \Delta T\right) \tag{4.34}$$

Since the active nucleate site density relation is based on plain surface, a coefficient k is presented in the heat flux equation to correct the active nucleate site density due to the existence of the surface structures. The heat flux on a structured surface is then

$$q'' = k(0.034\Delta T^2)\rho\frac{d\Phi}{dt}\left(h_{fg} + C_p\Delta T\right) \tag{4.35}$$

To identify the coefficient k, the possible nucleate sites on different structured surfaces were analyzed. In micropillared surfaces, the bubbles usually form at the root of the micropillars and there is likely only one bubble around one micropillar.[99] Thus the ratio between the micropillar size and the pitch 20 μm/100 μm =0.2 for the 20 μm × 20 μm pillars and 45 μm/200 μm=0.225 for the 45 μm × 45 μm pillars are reasonable coefficients of the micropillared surfaces. Based on classic thermal dynamics theory,[100, 101] it is difficult for nano gaps to form bubbles under the superheat range in this study. Micro cavities are the possible nucleate sites. The 4.7 μm long nanowire arrays have standing alone nanowires and nano gaps between nanowires. Since the uniform nanowires grew conformably on the substrate, the surface covered by standing alone nanowire arrays preserved the surface topology of the substrate so that the micro cavities on the substrate are the possible nucleate sites. Then it is reasonable to use 1 as the coefficient k of the 4.7 μm nanowire arrays covered surface. Since the nanowires agglomerate to form micro size nanowire bundles when the nanowires are long enough, it is important to figure out where the potential nucleate sites might form before estimating the coefficients for the 27 μm long nanowire arrays and the hierarchical structured surfaces. The cavities that could be activated have to fulfill two criterions. Firstly, the cavities have to be able to trap vapor so that bubbles can form based on the accumulation of vapor. Secondly, the cavities that could trap air have to reach a certain size to be activated. The contact angle 18.6° on 27 μm long nanowired Cu surface is larger than the maximum cavity mouth angle of 8.5° on the surface, which indicates that part of the micro-gaps between the nanowire bundles are able to trap air/vapor. The significant amount of micro gaps on the 27 μm long Cu nanowired surface ranges between 600 nm to 10 μm in size and can be activated in the superheat range of tests from 0 to 5°C. Treating the nanowire bundles as micropillars, the coefficient for the 27 μm long nanowired surface is 13 μm (average bundle size) /17 μm (average pitch) =0.76. The effective contact angle on the hierarchical structure is 5.1° while the average cavity mouth angle on the nanowired Cu surface in the valley of the hierarchical structure is 7.2°. Therefore, only limited number of micro gaps in the valley can trap air/vapor to serve as nucleate sites. Thus most of the bubbles are likely to generate at the roots of the nanowire-micro-pyramids, which indicates that micro structures dominate the pool boiling dynamics. However, the coefficient for the hierarchical structured surface should be larger than that for the 20 μm × 20 μm micropillared surface since the micro-pyramids are made of nanowires that contain more cavities and there are still possible sites in the valley. Assume that the coefficient *k* for the hierarchical structured surface is twice of that of the 20 μm × 20 μm micropillared surface. Therefore, k=0.2×2=0.4.

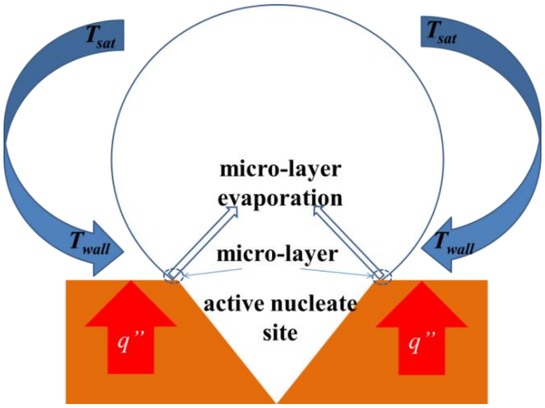

Figure 4. 13 Two main heat transfer modes, micro-layer evaporation and water superheated process, at an active nucleate site

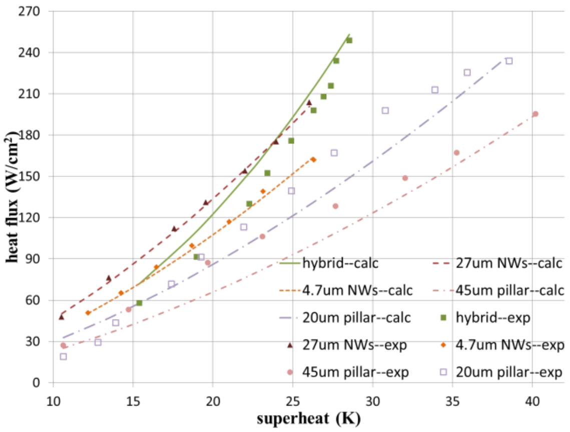

Figure 4. 14 Experiment and model predicted boiling curve comparison on five different structured surface

When the superheat is not high enough, the nucleate boiling is not in the fully developed boiling regime so that the bubbles generated at one active nucleate site don't form vapor columns. There exists a waiting time after the departure of a bubble and before the formation of a new bubble. Thus, liquid can reach the active nucleate site from above the site before the formation of the vapor column. Another coefficient describing the distribution of the liquid amount reaching the nucleate site is needed. Since the development regime is related to the superheat, it is reasonable to use the ratio between the superheat at CHF and the superheat as a coefficient. The heat flux-superheat relation thus becomes

$$q'' = k(0.034\Delta T^2)\rho \frac{d\Phi}{dt}\left(h_{fg} + C_p\Delta T\right)\frac{\Delta T_{CHF}}{\Delta T} \tag{4.36}$$

Figure 4.14 shows the experiment and the model predicted relations between the heat flux and the superheat. The superheat is chosen to be larger than 10°C to make sure all the data is in the nucleate boiling regime. The model predicted curves match the experiment results from the nanowire based structured surfaces well while deviate from those from the micropillared surfaces. From the comparison in the figure it is clear that the predictions match the experimental data well at the largest superheat. The predictions for the micropillared surfaces are not as good as those of the nanowired surfaces and the hierarchical surface. According to the fabrication processes of the two nanowired surfaces and the hierarchical structured surface, the nanowires grew conformably on the surfaces. The nanowire based surfaces therefore reserved the substrates' topology, especially when there were no nanowire bundles. The nucleate sites on uniform well-arranged micropillared surfaces, on the other hand, have less substrate topology information reserved. Since the active nucleate site density relation used in this study came from plain surface which has random distribution of nucleate sites, the predictions for the surfaces with nanowires match the experiment data better compared to those for uniform well-arranged micro structured surfaces.

When the heat flux approaches CHF, the predicted data matches the experiment data well on all the testing surfaces. When the heat flux is close to the CHF, vapor columns form due to the intensive generation of the vapor bubbles. The waiting period in a bubble cycle is missing and the re-wetting of the active nucleate site is fully accomplished by the liquid spreading resulted from the capillary force. No liquid can reach the active nucleate site from above the site after bubble departure. Thus Eq. 4.36 describes all the possible heat transfer paths so that the predicted data matches the experiment data well.

Chapter 5 Thermal Ground Plane Heat Transfer Enhancement

5.1 Sample Characterizations

The patterned Cu nanowire array wicking structure with square nanowire bundles and micro-scale gaps are shown in Figure 5.1. Two patterned Cu nanowire array wicking structures with nanowire bundle sizes (*p*) of 70 μm and 50 μm and gap sizes (*s*) of 45 μm and 65 μm were fabricated. The height of the nanowire bundles of two wicking structures were kept the same at 60 μm as shown in Figure 5.1. The shape corners from the mask were well reserved. Due to the roughness of the patterned PAA template, gaps formed and left space for electrolyte solution to penetrate. Unwanted Cu grains of ~ 1 μm size therefore deposited outside the patterns on the Cu sheet. Since the Cu grains were grown outside the patterns and small in size, the heat transfer performance won't be influenced.

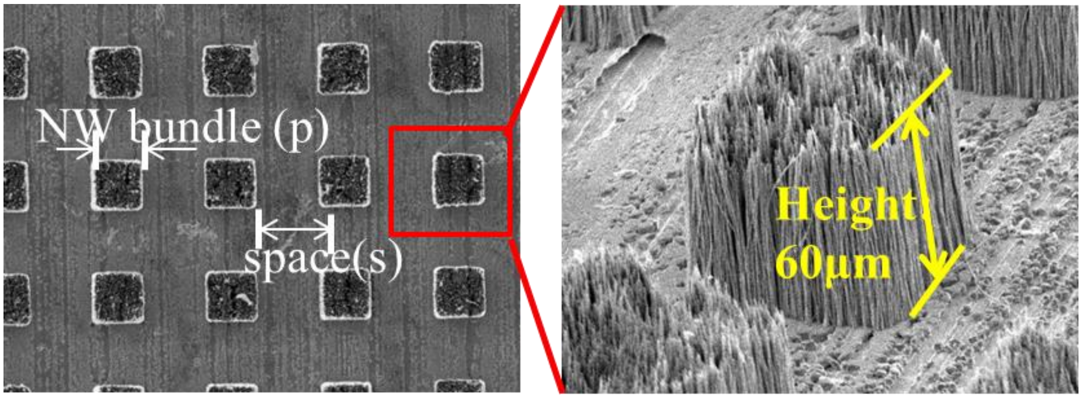

Figure 5. 1 SEM photos of the top and tilted view of the wicking structure

5.2 Testing system and data reduction

5.2.1 Testing system

The 200 μm thick Cu sheet with wicking structures was cut to 4 cm × 4 cm square with 3 cm × 3 cm structured area. The 5 mm wide edges were used for sealing purpose. A 1 mm thick and 5 mm wide Cu frame with a 1 mm diameter Cu tube was used to define the thickness of the vapor core. A sandwich structure was built to form a temporary TGP testing fixture. The sandwich structure consists of the alignment of the wicking structure, a 50 μm thick silicone washer, the 1 mm thick Cu frame, another 50 μm thick silicone washer, and a 3 mm thick glass plate with 1 mm diameter stainless steel spacers on one side. Two stainless steel frames with 16 screws were used to clamp the TGP. By tightening the screws, pressure was applied to the TGP and the vapor chamber was sealed. The TGP was pumped down to ~2×10^{-6} torr vacuum level for ~ 24 h and charged with degassed DI water which was boiled for more than 2 h from the Cu tube on the Cu frame.

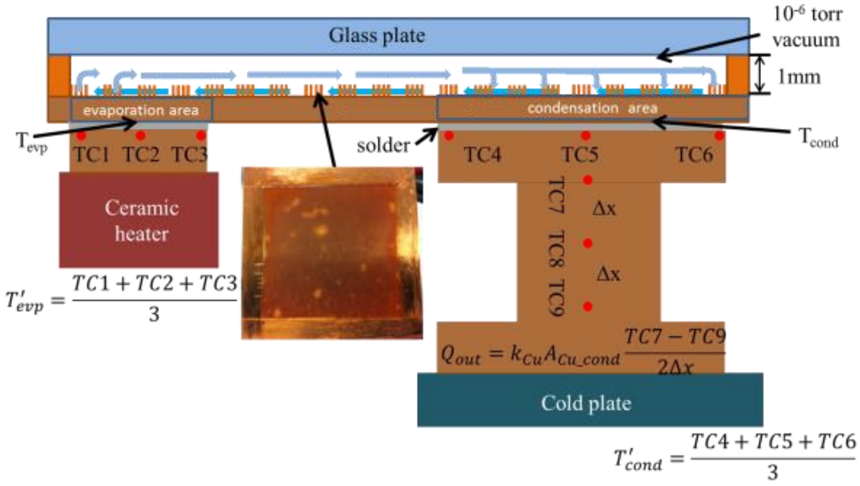

Figure 5. 2 The schematic of the testing system

The parameters to characterize the heat transfer performance of the TGP are the heat flux transferred by the TGP and the average temperature difference between the evaporation side and the condensation side. A testing system was built to measure the two parameters as shown in Figure 5.2. Two Cu blocks with thermocouples embedded were soldered onto the back side of the wicking structure. The two Cu blocks were placed at the two corners of a diagonal. The 5 mm × 5 mm × 5 mm Cu block was connected to an 8 mm × 8 mm ceramic heater (Watlow Inc.) with MX-4 thermal paste to provide uniform heat to the evaporation area and the other "I" shaped Cu block that has 2 cm × 2 cm contact area with the wicking structure was connected to a cold plate with MX-4 thermal paste to extract heat. The temperature of the cold plate was kept at 10 °C. The cold plate was powered by a circulator bath (HAAKE Phoenix II, Thermo ELECTRON Corp.) which is capable to remove as much as 500 W heat flow. The heat input was calculated by the product of the voltage and current from the heater power supply. The heat output was calculated from the thermocouple readings through one-dimensional heat conduction relation. The two Cu blocks were insulated with shaped glass fiber while the whole system was insulated with micro-fiber materials to reduce convective heat loss.

5.2.2 Data reduction

The thermocouples to measure the temperature of the evaporation side (TC1, TC2, and TC3) and the condensation side (TC4, TC5, and TC6) were embedded on the surfaces of the two Cu blocks that contact with the TGP along a diagonal. The average temperature of the evaporation side and the condensation side is calculated as:

$$T'_{evp} = \frac{TC1 + TC2 + TC3}{3} \tag{5.1}$$

$$T'_{cond} = \frac{TC4 + TC5 + TC6}{3} \tag{5.2}$$

It is quite clear that the average temperature calculated directly from the measured data don't reflect the real temperature of the TGP. The thermal resistance from the solder layer needs to be calibrated.

The thermocouples to measure the heat output (TC7, TC8, and TC9) were embedded into the center of the middle section of the condenser Cu block. The thickness of the 2 cm×2 cm section of the "I" shaped Cu block is 5 mm. The length of the middle section is 3 cm and the cross-section area of the middle section is 1 cm^2. TC7 is 1 cm away from the top surface while TC9 is 1 cm away from the bottom surface. The 1 cm distance guarantees the heat flux passing through our measurement locations is one-dimensional. The distances between TC7-TC8 and TC8-TC9 are Δx=1 cm. The output heat flux is calculated as:

$$Q_{out} = k_{Cu} A_{Cu\_cond} \frac{TC7 - TC9}{2\Delta x} \tag{5.3}$$

To test the performance of the insulation and calibrate the thermal resistance resulted from the solder layer, the system was first used to test a 1 mm thick Cu reference sample. The comparison between heat input and heat output is shown in Figure 5.3. The blue line is the result for perfect insulation case and the red squares are the results from the experimental measurement. The heat output is mostly ~ 95% of the heat input while the highest heat loss is ~7% under the largest heat input. Due to the convective heat loss, the heat flux calculated from the condensation side is used as the heat flux that can be transferred exclusively by the TGP. The average temperature difference between the evaporation and condensation sides was calculated based on the measured temperature on the Cu block surfaces by taking the thermal resistance of the solder layers into account. To obtain this information, a finite element model was built to simulate the temperature distribution of the testing system with 1mm thick Cu reference sample. The inputs for the simulation are shown in the inset of Figure 5.4. Heat input, heat output, and the convective heat transfer coefficients which indicate the heat loss from the testing system on all the surfaces. The heat input and heat output were directly imported to the model from the experiment data. The convective heat transfer coefficients were calculated based on the measured temperature on the surfaces from the experiment. With the temperature measured on the surface, the Rayleigh numbers on the surfaces can be calculated as:[102]

$$Ra = \frac{g\beta(T_s - T_\infty)\delta^3}{\nu^2} Pr \tag{5.4}$$

where g is the gravitational acceleration, δ,is the characteristic length of the surface geometry, β, ν, *and* Pr are the coefficient of volume expansion, the kinematics viscosity, and the Prandtl number of air, respectively. The convective heat transfer coefficients are calculated as:

$$h = \frac{k}{L}(0.68 + \frac{0.67Ra^{1/4}}{(1 + (0.492/Pr)^{9/16})^{4/9}}) \tag{5.5}$$

where k is the thermal conductivity of air and L is the characteristic length of the surfaces. The calculated convective heat transfer coefficients are shown in Figure 5.4. Although the Cu block on the condensation side was insulated, there was still heat loss due to the large surface area and a temperature that is lower than the room temperature. Since the same kind of solder ribbon was used and the reflow soldering technique was employed on both the evaporation side and the

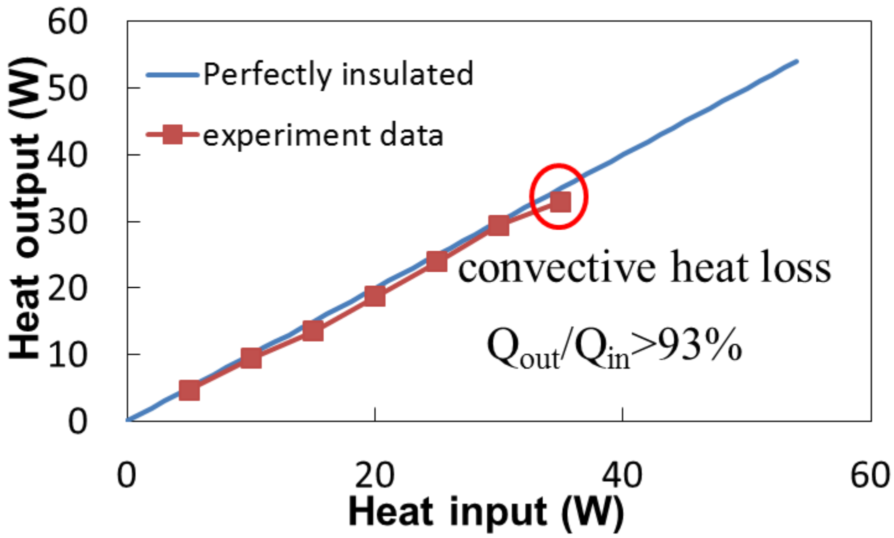

Figure 5. 3 Heat loss testing result of the system

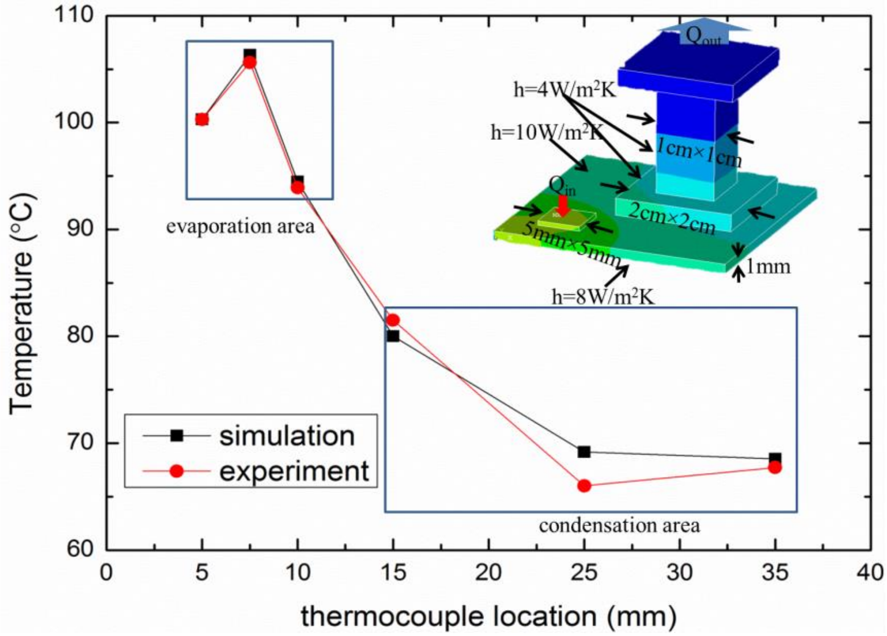

Figure 5. 4 Comparison of FEA model and experiment data of the temperature at the thermocouple locations. The inset is the FEA model and boundary conditions.

condensation side, the two solder layers were set to the same thickness. The thermal conductivity of the solder is 20 W/m·K from the manufacture's technique specifications. The thermal resistances of the solder layers were adjusted by changing the thickness of the solder layers in the simulation. With the adjustment of the thickness of the solder layers, the simulated temperature finally matched the measured temperature on the Cu block surfaces at the thermocouple locations as shown in Figure 5.4. Thus, the thermal resistances of the solder layers were determined and can be used to extrapolate the average temperature of the evaporation side and the condensation side on the TGP surface by one-dimensional heat conduction relation:

$$T_{evp} = T'_{evp} - Q_{in}R_{evp} \tag{5.6}$$

$$T_{cond} = T'_{cond} + Q_{out}R_{cond} \tag{5.7}$$

The temperature difference between the evaporation side and the condensation side thus is

$$\Delta T = T_{evp-}T_{cond} \tag{5.8}$$

With Eq. (5.3) and (5.8), we obtained the two parameters to characterize the heat transfer performance of our TGP.

5.3 Testing results

The heat transfer performance of the TGPs with two different wicking structures is shown in Figure 5.5. The x-axis is the heat flux transferred by the TGPs and the y-axis is the average temperature difference between the evaporation side and the condensation side of the TGP surface. The red line is the testing result of the Cu reference sample while the light blue dash line is the result from the simulation on a Cu reference sample. The two lines are close to each other, which indicates that the thermal resistance from the simulation can be used to calculate the average temperature difference between the evaporation and the condensation sides on the TGP surfaces. Since the temperature on the evaporation side or the heated side was larger than 120 °C under 50 W/cm^2 on the Cu reference sample, the experiment was terminated. Therefore, the heat transfer performance on the Cu reference sample didn't span the whole heat flux range.

The heat transfer performance of both TGPs is better than that of the Cu reference sample since as the heat flux increases, the temperature difference of the TGPs is much smaller than that of the Cu reference sample. In low heat flux region, the temperature difference increases with the increase of the heat flux. This is the start-up stage of the TGPs. Then the temperature difference keeps almost the same at ~30°C in the heat flux range of ~40W/cm^2 to ~140W/cm^2, which is a typical characteristic of heat pipes due to the nature of the phase change heat transfer. The further increase of the heat flux results in dry-out of the evaporation section. The maximum heat fluxes before dry-out are~160W/cm^2 on the TGP with 70μm nanowire bundles and ~200W/cm^2 on the TGP with 50μm nanowire bundles. The ratio between these two maximum heat fluxes is 198/156=1.26. As we know, the maximum heat flux is limited by the wicking performance and is proportional to the ratio between the permeability and the effective pore radius of the wicking structures, K/R_{eff}. The K/R_{eff} can be obtained from the wicking performance measurement. Analysis and measurement of the wicking performance of the patterned nanowire array wicking structures are necessary.

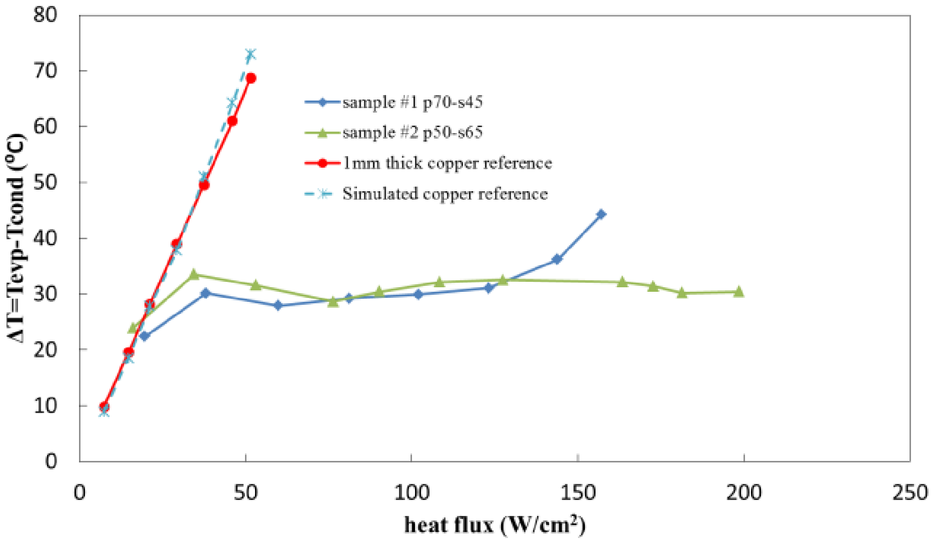

Figure 5. 5 The heat transfer performance of copper reference and two TGPs

5.4 Discussions

When the liquid flows within the patterned nanowire array wicking structures, there are two time scales as shown in Figure 5.6.

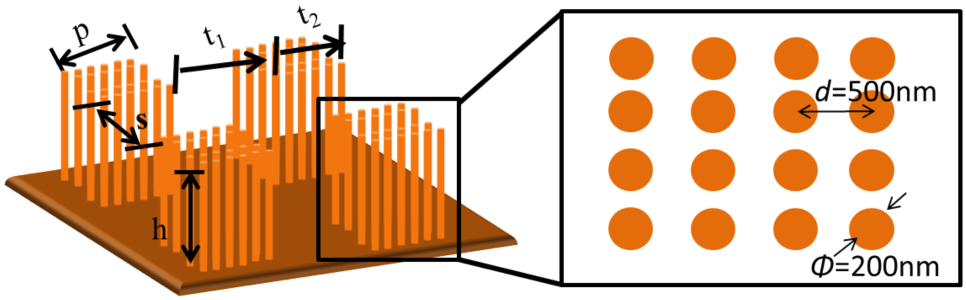

Figure 5. 6 Liquid flow within the patterned nanowire array wicking structure

t_1 is the time for liquid to flow from one nanowire bundle to the adjacent one through the micro scale gap while t_2 is the time for liquid to flow from one edge of the nanowire bundle to the other within the nanowire bundle. t_1 is determine by the size of the gap s, the height h and the size of the nanowire bundle p

$$t_1 \sim \frac{s^2}{[h^2 p/(p+s)^2]} \tag{5.9}$$

while t_2 is determined by the size of the nanowire bundle, the diameter Φ and the pitch d of the nanowire.[87]

$$t_2 \sim \frac{p^2}{\Phi \ln(d/\Phi)} \tag{5.10}$$

Based on our calculation, $t_2/t_1 \sim p/\Phi \sim 100$. Therefore, $t2$ dominates and is about two orders larger than t_1, which means liquid flows faster on the wicking structure with smaller nanowire bundle size. The wicking performance on patterned nanowire array wicking structure with 50µm nanowire bundles is better.

A capillary rise experiment has been carried out on the patterned nanowire array wicking structures. High-speed camera was used to record the propagation of the wicking front at 500fps.

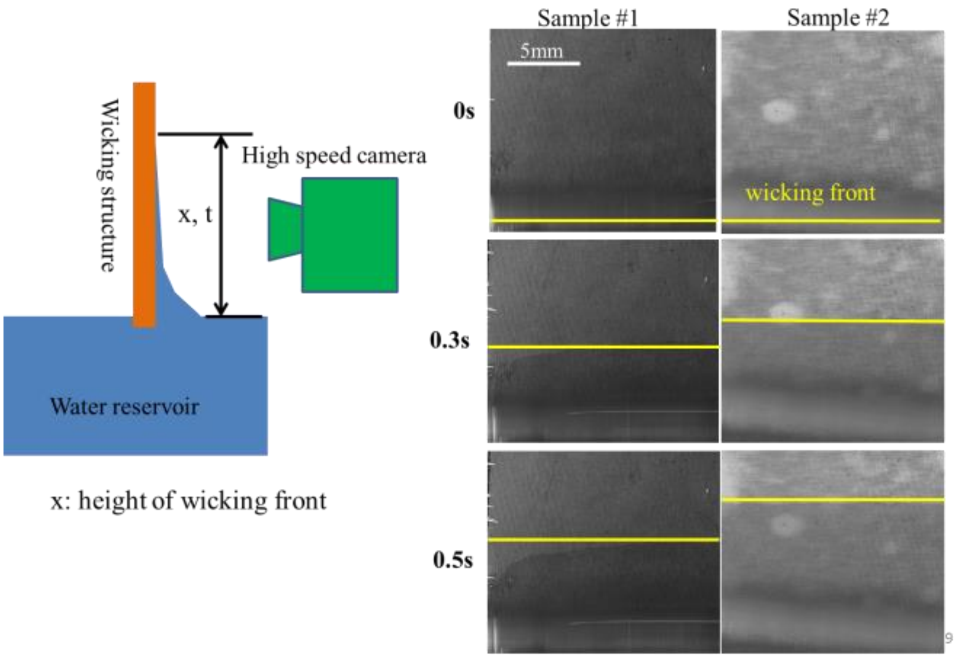

Figure 5. 7 Schematic of the capillary rise experiment and the wicking performance of the two wicking structures.

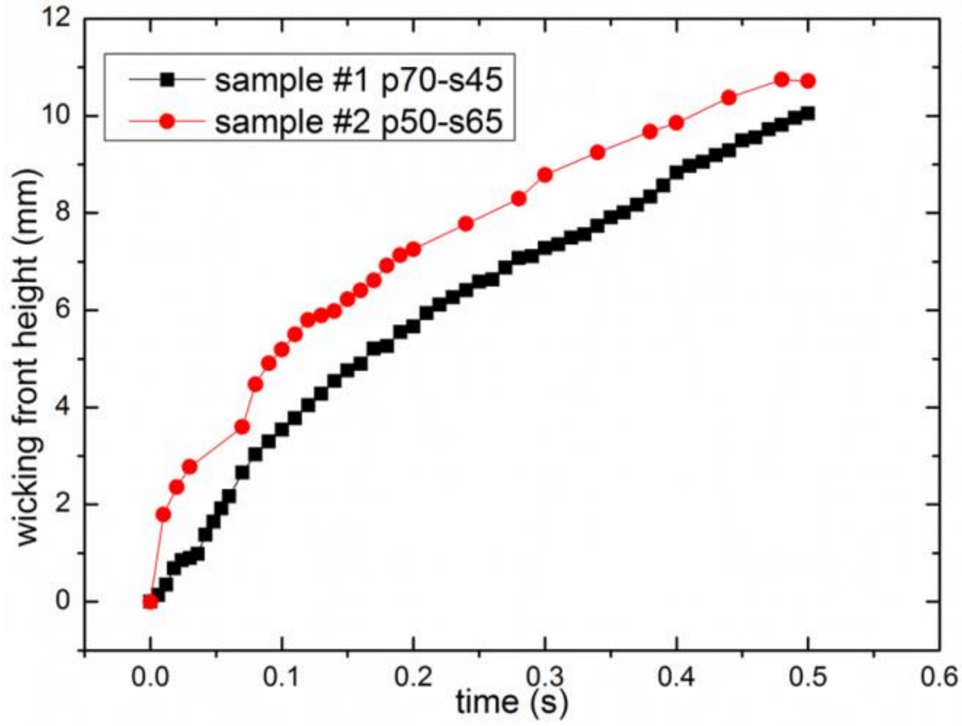

Figure 5. 8 Detailed relation between the height of the wicking front and time on two different wicking structures.

Figure 5.7 shows the propagation of the wicking front on two patterned nanowire array structures at different time. Although water flew across the entire structured area on both wicking structures after long enough time, the wicking front on structure with 50μm nanowire bundle moves faster, which confirms the analysis above. Figure 5.8 shows the detailed relation between time and the height of the wicking front. The relation between time and the height of the wicking front is described as Eq. 5.11.

$$x^2 \sim K/R_{eff} \cdot t/\varepsilon \qquad (5.11)$$

where ε is the porosity of the nanowire bundle since the time consumed during the liquid propagation occurs mainly within the nanowire bundles.

By fitting the data with Eq. 5.11, the K/R_{eff} can be extracted. The coverage of the nanowires in the nanowire bundles on two structures is ~50% based on the SEM images. The ratio between the two K/R_{eff} that indicates the maximum heat flux ratio is 1.14, which matches the experimental measured result well and is only 10% lower. The possible reason is that the water charging amount is right to saturate the wicking structure with 50μm nanowire bundles which is too much for the wicking structure with 70μm nanowire bundles. This will result in flooding in the condensation area, and thus a lower maximum heat flux than expected. Therefore, the ratio from experiment is larger.

Chapter 6 Summary and Future Work

The phase change heat transfer performance was greatly enhanced with Cu nanowire based structures in our study. The movement of the three phase contact line has been proved to play an important role in the phase change heat transfer enhancement. The CHF on the nanowire/micropillar hierarchical structured surface is more than 70% higher than that on the smooth surface. When the contact angle is smaller than 30°, the effect of wettability (contact angle) on CHF attenuates while the effect of liquid spreading becomes important. The liquid spreads on the surface due to the capillary force and the flow resistance resulted from the structures. By carefully design and choose the structure, liquid can be pumped to the active nucleate site under extremely high heat flux so that the CHF is delayed. The HTC on the SAM coated hydrophobic nanowired surface is more than four times higher than that on the smooth surface at its maximum value and the occurrence of the Wenzel state droplets has been delayed to ~ 10 K. The pull-out movement and shrinking of the contact line guarantees a high HTC with the jumping removal mode. The carefully chosen solid fraction of the nanowire keeps the contact line short to delay the occurrence of the Wenzel state droplets. The maximum heat flux transferred by the TGP with patterned nanowire array wicking structure reached 200 W/cm^2. Better wicking performance provides better liquid feeding to the heated area so that the higher heat flux can be transferred by the TGP before dry out occurs. The wicking performance is the movement of the three phase contact line which is heavily influenced by the nanostructures on the surfaces.

6.1 Summary for dropwise condensation enhancement

A condensation chamber had been built for dropwise condensation chamber under limited NCG condition. Dropwise condensation experiments were conducted on SAM coated hydrophobic smooth surface and three hydrophobic nanowired surfaces with lengths from 10 μm to 30 μm. The condensation heat transfer performance on the 10 µm to 30µm long nanowired surfaces has similar trend and is better than that on the smooth surface for a subcooling range from ~0.3 K to ~15 K. A transition occurs on the 10 µm to 30µm long nanowired surfaces at ~8 K while the condensation heat transfer curve on the smooth surface grows smoothly. As subcooling further increases, the condensation heat transfer performance on all the surfaces is almost the same.

The images recorded with the condensation process show that as the subcooling increases the droplet states can gradually change from Cassie or partially-wetting Cassie state to steady Wenzel state and the droplet removal mode can gradually change from coalescence induced jumping off to sweeping on the 10 µm to 30µm long nanowired surfaces while only sweeping removal mode exist on smooth surface. When the partially-wetting Cassie state is the only wetting state and the jumping-off is the only removing mode on the nanowired surfaces, the dropwise condensation heat transfer performance was enhanced. In contrast, once Wenzel state droplets and sweeping removal mode appeared on the surface, the heat transfer performance started to degrade. As soon as the Wenzel state droplets and sweeping removal are the only state and removing mode on the surfaces, the heat transfer performance were all the same on all the surfaces. The occurrence of the Wenzel state droplet has been confirmed as the failure of the dropwise condensation enhancement.

The nanowired surfaces in this study are Cassie stable surfaces due to the hydrophobic coating and the nanostructures. Calculation shows that once the droplet grows out of the tips of the structures the condensate can’t wet downward into the structures. The appearance of the Wenzel state droplets can only be the result of the increasing condensation intensity. Under small subcooling, the nucleation of the droplets occurs on discrete locations which results in enough time for droplets in partial wetted Cassie state to grow before interaction with the neighboring condensate. The released energy from droplets coalescence can easily overcome the resistance at the contact line and result in jumping off of the coalesced droplet from the surface. The high heat transfer rate of the partial wetted Cassie droplets and the fast jumping off removal mode makes the heat transfer performance on the nanowired surfaces better than that on smooth surface. As subcooling increases, condensate in neighboring nanowire gaps interacts with each other due to the increase of the nucleate site density to increase the wetting area beneath a droplet. The HTC enhancement starts to decrease. Although the condensate droplets are still able to jump from the surface after coalescence, the liquid bridges remain in the structures. As a consequence, the dry area for re-nucleation reduces, which results in the decrease of the HTC. As subcooling further increases, the liquid bridge grows larger and coalescence induced jumping can't occur. The coalesced droplet experiences temporary shrinking of the contact line. Due to the fast growth of condensate in the nanowire gaps, the coalesced droplets will change to Wenzel state. A model based on the surface energy conservation has been developed to calculate this process and explain the reason why the occurrence of the Wenzel state droplets can be delayed on our structures. An optimum range of solid fraction has been calculated. When the solid fraction falls in this range, the occurrence of the Wenzel state droplet can be delay and enhanced dropwise condensation can be realized for a long subcooling range. When the surface is fully covered with Wenzel state droplets under high subcooling condition, droplets can only be removed by sweeping. The same droplet wetting state and the same removal mode result in the same heat transfer performance on all the surfaces.

The existence of the nanowires on the surface makes the partial wetting Cassie state droplets and jumping off removal mode possible so that the dropwise condensation heat transfer performance on nanowired surface is enhanced compared to that on smooth surface. The carefully chosen solid fraction of the nanowired surfaces can sustain enhanced dropwise condensation in a large range of subcooling.

6.2 Summary for pool boiling

In summary, we have systematically studied the liquid spreading and pool boiling heat transfer performances on Cu micropillared surfaces, Cu nanowired surfaces and a hierarchical nanowire/micropillar structured Cu surface. Samples with contact angles spanning from 5 to 30° and non-monotonic contact angle-liquid spreading relation was successfully realized. A heat transfer performance testing system has been built. A dynamic contact angle testing system with high speed camera has also been built to measure the static contact angle and the dynamic liquid spreading process. The liquid spreading speed has been accurately extracted from the dynamic liquid spreading process. The CHF on the nanowire/micropillar hierarchical is the highest among all the testing surfaces. In general, the CHF on the micropillar surfaces is better than that on the nanowire surfaces although the contact angles on the nanowire surfaces are smaller than those on the micropillar surfaces while the HTC on the nanowire surfaces is better than that on the micropillar surfaces. With the smallest contact angle and the fastest liquid spreading speed, the nanowire/micropillar hierarchical surface presents the best boiling heat transfer performance. The CHF data from the experiments has been compared with a modified CHF model that considers the influence the effect of the liquid spreading. The well agreement between the modified CHF model and the experiment data indicates the importance of the liquid spreading on CHF with the non-monotonic contact angle-liquid spreading relation. A heat flux-superheat relation including the effect of liquid spreading was built based on the two main heat transfer modes at an active nucleate site. The effect of surface structure on active nucleate site density was analyzed in detail and included in the coefficient *k*. The predictions of the heat flux-superheat relation match the experimental data of the surfaces with nanowired surfaces and the hierarchical surface well, while derivate from the experimental data of the surfaces with micropillars. Besides, when the heat flux is close the CHF, all the predicted data matches the experimental data. The liquid replenishment to an active nucleate site is from both the top of a bubble and the structures under capillary force. When the heat flux is close to the CHF, the liquid replenishment is only from the structures. That explains why the predicted data matches the experimental data when the heat flux is close to the CHF.

6.3 Summary for TGP

A MEMS/nano fabrication procedure has been developed to fabrication patterned PAA template. Two patterned nanowire array wicking structures were successfully fabricated with patterned PAA template assisted electro-deposition method. A testing system to measure the wicking performance has been built with a high speed camera to measure the wicking performance of the patterned nanowire array wicking structures. Analysis about the liquid transportation behavior has been carried out and the dominant factor influencing the wicking performance has been determined. The measured wicking performance on the wicking structures confirmed the analysis. The key factor affecting the maximum heat flux has been extracted from the wicking performance measurements. The heat transfer measurement shows that the TGP with patterned nanowire array wicking structures have superior heat transfer performance than that of copper sheet with the same dimensions. The ratio between the two maximum heat flux from the experiment matches the predicted value from the wicking performance measurements. A 200W/cm^2 maximum heat flux was realized from the TGP equipped with patterned nanowire array wicking structure with 1 mm thick vapor space, which indicates the potential for TGP to remove even higher heat flux with patterned nanowire array wicking structures.

6.4 Future work

The fabrication process of the SAM coated hydrophobic nanowire surface still suffers from two major problems although the fabrication process is easy to realize. When the nanowire is not long enough (<15 μm), the coverage of the nanowires deviates from the porosity of the PAA template. The roughness mismatch between the target surface and the PAA is the reason. This limits length range of the investigation of dropwise condensation performance and results in heat transfer performance degradation on short nanowire surfaces. The second problem is the SAM coating process. In our current study, the sample was coated by immersing into the coating solution. The nano scale gap within the nanowires and the agglomeration of the nanowires prevent the solution from penetrating into the nanowire structures and applying uniform reaction. Therefore, the coating quality is not as stable as expected, which results in large error in the experiments. To solve the first problem, the roughness and the rigidity of the PAA needs to be improved so that the template can attach to the substrate more conformably. Atomic-layer-deposition (ALD) has been applied to coat surfaces conformably no matter how complex the surface structures are and is a promising approach to solve the coating problem we met when reasonable and stable coating material is chosen.

Although the optimum solid fraction range has been calculated and the dropwise condensation heat transfer enhancement has been realized under extended subcooling range, the occurrence of the Wenzel state droplets is still inevitable when the nucleate site saturates on the condensation surface. This saturation cannot be avoided just by structure design. To remove the condensate effectively before it interacts with the adjacent condensate and keep part of the surface dry for re-nucleation are the solution to further delay the occurrence of the Wenzel state droplets. Hydrophilic/Hydrophobic hybrid coating on nano structured surfaces has the potential to realize what has been mentioned above. The hydrophilic surface serves as nucleate sites at pre-defined locations while the hydrophobic surface makes the highly effective jumping removal manner possible. It is possible that the condensate on the surface is attracted to the large droplets on the hydrophilic surface area so that there is always dry area for re-nucleation. The challenges in this kind of study are the design of the hydrophobic/hydrophilic hybrid patterns, the choosing of the base nano structures, and methods to realize the fabrication process.

The liquid spreading has been proven to play an important role for pool boiling enhancement in terms of CHF and HTC. The modified model that incorporates the effect of the liquid spreading matches the experiment data well. However, a coefficient was employed in the model from data fitting. Although the coefficient which is smaller than 1 shows that when structure presents on the surface the effect of the contact angle is attenuated, how does the liquid spreading influence the CHF in a mechanistic point of view has been explained yet. The original model was deducted from the force field applied at the liquid-vapor interface of a bubble. When structures present on the surface, the liquid spreading provides one more force onto the liquid-vapor interface. The challenge is that it is difficult to determine the area where the force resulted from the liquid spreading is applied on. Besides, when the liquid spreading performance is measured, it is also difficult to obtain the thickness of the wicking front which is directly related to the area needed to calculate the area where the force is applied on. Once the wicking front thickness is determined, the force resulted from the liquid spreading can be applied into the model. In addition, the force resulted from the liquid spreading is from the capillary force generated by the surface structures. Once the relation between the structures and the capillary force can be obtained, the effect of the surface structures can be involved into the model directly.

The heat transfer measurements show that the TGP with patterned nanowire array wicking structures can deliver very high maximum heat flux. Two patterns with different dimensions of nanowire bundles and micro gaps have been tested in our study. This study shows that the wicking performance plays an important role in the maximum heat flux and proposes the method to predict the maximum heat flux from the wicking performance. Apparently, more patterns are needed to provide solid evidence to our conclusions. As a parametric study in the future, the working fluid charging amount needs to be optimized to obtain more accurate measuring results for every single wicking structure. The dimensions of the patterned nanowire array need more studies since they not only influence the wicking performance but also the shape of the menisci. The shape of the menisci determines the efficiency of the evaporative heat transfer. The height of the nanowires is another important parameter to study. The shape of the menisci and the thermal resistance resulted from the bulk water in the menisci are affected by the height of the nanowires. The thickness of the vapor core is also important to determine the heat transfer performance of the TGP. When the thickness of the vapor core is thin enough, the friction at the liquid-vapor interface may result in early dry out. All the heat transfer performance was measured in a temporary testing fixture. To make the TGP usable in real world, a reliable process needs to be developed to assemble a real device. The reliability of the TGP device is then needed to be investigated.

References

---

(1) Dimitrakopoulos, D.; Higdon, J. J. L. On the gravitational displacement of three-dimensional fluid droplets from inclined solid surfaces. *J. Fluid Mech.* **1999,** *395*,181-209.
(2) Bang, I. C.; Jeong, J. H. Nanotechnology for advanced nuclear thermal-hydraulics and safety: boiling and condensation. *Nucl. Eng. Technol.* **2011,** *43*, 217-242.

(3) Lara, J. R.; Holtzapple, M. T. Experimental investigation of dropwise condensation on hydrophobic heat exchangers part i: dimpled-sheets. *Desalination* **2011,** *278*, 165-172.

(4) Lara, J. R.; Holtzapple, M. T. Experimental investigation of dropwise condensation on hydrophobic heat exchangers. part ii: effect of coatings and surface geometry. *Desalination* **2011,** *280*, 363-369.

(5) Kandlikar, S. G. A roadmap for implementing minichannels in refrigeration and air-conditioning systems - current status and future directions. *Heat Transfer Eng.* **2007,** *28*, 973-985.

(6) Rykaczewski, K.; Scott, J. H. J.; Rajauria, S.; Chinn, J.; Chinn, A. M.; Jones, W. Three dimensional aspects of droplet coalescence during dropwise condensation on superhydrophobic surfaces. *Soft Matter* **2011,** *7*, 8749-8752.

(7) Anderson, D. M.; Gupta, M. K.; Voevodin, A. A.; Hunter, C. N.; Putnam, S. A.; Tsukruk, V. V.; Fedorov, A. G. Using amphiphilic nanostructures to enable long-range ensemble coalescence and surface rejuvenation in dropwise condensation. *ACS Nano* **2012,** *6*, 3262-3268.

(8) Bok, H. M.; Shin, T. Y.; Park, S. Designer binary nanostructures toward water slipping superhydrophobic surfaces. *Chem. Mater.* **2008,** *20*, 2247-2251.

(9) Dorrer, C.; Ruhe, J. Wetting of silicon nanograss: from superhydrophilic to superhydrophobic surfaces. *Advanced Materials* **2008,** *20*, 159-163.

(10) Lau, K. K. S.; Bico, J.; Teo, K. B. K.; Chhowalla, M.; Amaratunga, G. A. J.; Milne, W. I.; McKinley, G. H.; Gleason, K. K. Superhydrophobic carbon nanotube forests. *Nano Lett.* **2003,** *3*, 1701-1705.

(11) Miljkovic, N.; Enright, R.; Wang, E. N., Effect of droplet morphology on growth dynamics and heat transfer during condensation on superhydrophobic nanostructured surfaces. *ACS Nano* **2012,** *6*, 1776-1785.

(12) Rykaczewski, K.; Chinn, J.; Walker, M. L.; Scott, J. H. J.; Chinn, A.; Jones, W. Dynamics of nanoparticle self-assembly into superhydrophobic liquid marbles during water condensation. *ACS Nano* **2011,** *5*, 9746-9754.

---

(13) Rykaczewski, K.; Scott, J. H. J. Methodology for imaging nano-to-microscale water condensation dynamics on complex nanostructures. *ACS Nano* **2011,** *5*, 5962-5968.

(14) Ma, X. H.; Wang, S. F.; Lan, Z.; Peng, B. L.; Ma, H. B.; Cheng, P. Wetting mode evolution of steam dropwise condensation on superhydrophobic surface in the presence of noncondensable gas. *J. Heat Trans.-T. ASME* **2012,** *134*, 021501.

(15) Chen, C. H.; Cai, Q. J.; Tsai, C. L.; Chen, C. L.; Xiong, G. Y.; Yu, Y.; Ren, Z. F. Dropwise condensation on superhydrophobic surfaces with two-tier roughness. *Appl. Phys. Lett.* **2007,** *90,* 173108.

(16) Boreyko, J. B.; Chen, C. H. Self-propelled dropwise condensate on superhydrophobic surfaces. *Phys. Rev. Lett.* **2009,** *103*, 184501.

(17) Chen, X. M.; Wu, J.; Ma, R. Y.; Hua, M.; Koratkar, N.; Yao, S. H.; Wang, Z. K. Nanograssed micropyramidal architectures for continuous dropwise condensation. *Adv. Funct. Mater.* **2011,** *21*, 4617-4623.

(18) Cheng, Y. T.; Rodak, D. E.; Angelopoulos, A.; Gacek, T. Microscopic observations of condensation of water on lotus leaves. *Appl. Phys. Lett.* **2005,** *87*, 194112.

(19) Cassie, A. B. D.; Baxter, S. Wettability of porous surfaces. *T. Faraday Soc.* **1944,** *40,* 546-550.

(20) Wenzel, R. N. Resistance of solid surfaces to wetting by water. *Ind. Eng. Chem.* **1936,** *28*, 988-994.

(21) Bico, J.; Tordeux, C.; Quere, D. Rough wetting. *Europhys. Lett.* **2001,** *55*, 214-220.

(22) Lafuma, A.; Quere, D. Superhydrophobic states. *Nat. Mater.* **2003,** *2*, 457-460.

(23) Kumar, V.; Sridhar, S.; Errington, J. R. Monte carlo simulation strategies for computing the wetting properties of fluids at geometrically rough surfaces. *J. Chem. Phys.* **2011,** *135*, 184702.

(24) Miljkovic, N.; Enright, R.; Nam, Y.; Lopez, K.; Dou, N.; Sack, J.; Wang, E. N. Jumping-droplet-enhanced condensation on scalable superhydrophobic nanostructured surfaces *Nano Lett.* **2013,***13*, 179-187

(25) Gao, F.; Viry, L.; Maugey, M.; Poulin, P.; Mano, N. Engineering hybrid nanotube wires for high-power biofuel cells. *Nat. Commun.* **2010,** *1,* 1-7.

(26) Yang, L.; Choi, Y. M.; Qin, W.; Chen, H.; Blinn, K.; Liu, M.; Bai, J.; Tyson, T. A.; Liu, M. Promotion of water-mediated carbon removal by nanostructured barium oxide/nickel interfaces in solid oxide fuel cells. *Nat. Commun*. **2010,** *2,* 357-366.

---

(27) Fernandez, J. E. Materials for aesthetic, energy-feeicient, and self-diagnostic buildings. *Science* **2007,** *315,* 1807-1810.

(28) Xiong, F.; Liao, A. D.; Estrada, D.; Pop, E. Low-power switching of phase-change materials with carbon nanotube electrodes. *Science* **2011,** *332,* 568-570.

(29) Jesorka, A.; Orwar, O. Nanofluidics: neirth shaken nor stirred. *Nature Nanotech.* **2012,** *7,* 6-7.

(30) Liter, S. G.; Kaviany, M. Pool-boiling CHF enhancement by modulated porous-layer coating: theory and experiment. *Int. J. Heat Mass Transfer* **2001,** *44,* 4287-4311.

(31) Li, C. H.; Li, T.; Hodgins, P.; Hunter, C. N.; Voevodin, A. A.; Jones, J. G.; Peterson, G. P. Comparison study of liquid replenishing impacts on critical heat flux and heat transfer coefficient of nucleate pool boiling on multiscale modulated porous structures. *Int. J. Heat Mass Transfer* **2011,** *54,* 3146-3155.

(32) Bain, C. D. Drip painting on a hot canvas. *Nature Nanotech*. **2007,** *2,* 344-345.

(33) Li, C.; Wang, Z.; Wang, P. I.; Peles, Y.; Koratkar, N.; Peterson, G. P. Nanostructured copper interfaxes for enhanced boiling. *Small* **2008,** *4,* 1084-1088.

(34) Kim, H.; Truong, B.; Buongiorno, J.; Hu, L. W. On the effect of surface roughness height, wettability, and nanoporosity on Leidenfrost phenomena. *Appl. Phys. Lett.* **2011,** *98,* 083121.

(35) Chen, R.; Lu, M. C.; Srinivasan, V.; Wang, Z. J.; Cho, H. H.; Majumdar, A. Nanowires for enhanced boiling heat transfer. *Nano Lett.* **2009,** *9,* 548-553.

(36) Miller, W. J.; Gebhar, B.; Wright, N.T. Effects of boiling history on a microconfigured surface in a dielectric liquid. *Int. Commun. Heat Mass* **1990,** *17,* 389-398.

(37) Mori, S.; Okuyama, K. Enhancement of the critical heat flux in saturated pool boiling using honeycomb porous media. *Int. J. Multiphase Flow* **2009,** *35,* 946-951.

(38) Linke, H.; Aleman, B. J.; Melling, L. D.; Taormina, M. J.; Francis, M. J.; Dow-Hygelund, C. C.; Narayanan, V.; Taylor, R. P.; Stout, A. Self-propelled Leidenfrost droplets. *Phys.Rev. Lett.* **2006,** *96,* 154502.

(39) Dhir, V. K.; Liaw, S. P. Framework for a unified model for nucleate and transition pool boiling. *J. Heat Transfer* **1989,** *111,* 739-746.

(40) Haramura, Y.; Katto, Y. New hydrodynamic model of critical heat flux applicable widely to both pool and forced convection boiling on submerged bodies in saturated liquids. *Int. J. Heat Mass Transfer* **1983,** *26,* 389-399.

(41) Cooper, M. G.; Lloyd, A. J. P. The microlayer in nucleate pool boiling. *Int. J. Heat Mass Transfer* **1969,** *12,* 895-913.

(42) Zuber, N. *Hydrodynamic Aspects of Boiling Heat Transfer;* AEC Report AECU-4439, June **1959**.

(43) Feng, B.; Weaver, K.; Peterson, G. P. Enhancement of critical heat flux in pool boiling using atomic layer deposition of alumina. *Appl. Phys. Lett.* **2012,** *100,* 053120.

(44) Rohsenow, W. M. A method of correlating heat transfer data for surface boiling of liquids. *Trans. of ASME* **1962,** *84,* 969-976.

(45) Tien, C. L. A hydrodynamic model for nucleate pool boiling. *Int. J. Heat Mass Transfer* **1962,** *5,* 533-540.

(46) Chu, K.-H.; Ryan, C. E.; Wang, E. N. Structured surfaces for enhanced pool boiling heat transfer. *Appl. Phys. Lett.* **2012,** *100,* 241603.

(47) Kandlikar, S. G. A theoretical model to predict pool boiling CHF incorporating effects of contact angle and orientation. *J. Heat Transfer* **2001,** *123,* 1071-1079.

(48) Mikic, B. B.; Rohsenow, W. M. A new correlation of pool boiling data including the effect of heating surface characteristics. *J. Heat Transfer* **1969,** *91,* 245-250.

(49) Kim, J. Review of nucleate pool boiling bubble heat transfer mechanisms. *Int. J. Multiphase Flow* **2009,** *35,* 1067-1076.

(50) Yagov, V. V. Generic features and puzzles of nucleate boiling. *Int. J. Heat Mass Transfer* **2009,** *52,* 5241-5249.

(51) Ahn, H. S., Jo, H. J., Kang, S. H., Kim, M. H. Effect of liquid spreading due to nano/microstructures on the critical heat flux during pool boiling. *Appl. Phys. Lett.* **2011,** *98,* 071908.

(52) Dhir, V. K. Boiling heat transfer. *Annu. Rev. Fluid Mech.* **1998,** *30,* 365-401.

(53) Mahajan, R.; Chiu, C. P.; Chrysler, G. Cooling a microprocessor chip. *Proceedings of the IEEE* **2006,** *94,* 1476-1486.

(54) Reay, D.; McGlen, R.; Kew, P. Heat Pipes—Theory, Design and Applications 5th Edition. Butterworth-Heinemann: Waltham, MA, 2006.

(55) Moore, G. E. Cramming more components onto integrated circuits. *Proceedings of the IEEE* **1965,** *86,* 82-85.

(56) Ma, H. B.; Lofgreen, K. P.; Peterson, G. P. An Experimental Investigation of a High Flux Heat Pipe Heat Sink. *J. Electron. Packag.* **2005,** *128,* 18-22.

---

(57) Cao, Y.; Gao, M. Wickless Network Heat Pipes for High flux Spreading Applications. *Int. J. Heat Mass Trans.* **2002,** *45,* 2539-2547.

(58) Christensen, A.; Graham, S. Thermal Effects in Packaging High Power Light Emitting Diode Arrays. *Appl. Therm. Eng.* **2009,** *29,* 364-371.

(59) Lu, X. Y.; Hua, T. C.; Wang, Y. P. Thermal Analysis of High Power LED Package with Heat Pipe Heat Sink. *Microelectron. J.* **2011,** *42,* 1257-1262.

(60) Yang, X.; Yan, Y. Y.; Mullen, D. Recent Developments of Lightweight, High Performance Heat Pipes. *Appl. Therm. Eng.* **2012,** *33-34,* 1-14.

(61) Khrustalev, D.; Faghri, A. Estimation of the Maximum Heat Flux in the Inverted Meniscus Type Evaporator of a Flat Miniature Heat Pipe. *Int. J. Heat Mass Trans.* **1996,** *39,* 1899-1909.

(62) Launay, S.; Sartre, V.; Lallemand, M. Experimental Study on Silicon Micro-Heat Pipe Arrays. *Appl. Therm. Eng.* **2004,** *24,* 233-243.

(63) Wang, Y.; Peterson, G. P. Investigation of a Novel Flat Heat Pipe. *J. Heat Transfer* **2005,** *127,* 165-170.

(64) Lin, L. C.; Ponnappan, R.; Leland, J. High Performance Miniature Heat Pipe. *Int. J. Heat Mass Trans.* **2002,** *45,* 3131-3142.

(65) Peterson, G. P. Overview of Micro Heat Pipe Research and Development. *Appl. Mech. Rev.* **1992,** *45,* 175-189.

(66) Liou, J. H.; Chang, C. W.; Chao, C.; Wong, S. C. Visualization and Thermal Resistance Measurement for the Sintered Mesh-Wick Evaporator in Operating Flat-Plate Heat Pipes. *Int. J. Heat Mass Trans.* **2010,** *53,* 1498-1506.

(67) Peter, H. J. de Bock. *et al*. Development and Experimental Validation of a Micro/Nano Thermal Ground Plane. *Proceedings of the ASME/JSME 2011 8th Thermal Engineering Joint Conference.* **2011,** Honolulu, Hawaii, USA.

(68) Cai, Q.; Chen, C. L. Design and Test of Carbon Nanotube Biwick Structure for High-Heat-Flux Phase Change Heat Transfer. *J. Heat Transfer* **2010,** *132,* 052403.

(69) Nam, Y.; Sharratt, S.; Byon, C.; Kim, S. J.; Ju, Y. S. Fabrication and Characterization of the Capillary Performance of Superhydrophilic Cu Micropost Arrays. *J. Microelectromech. S.* **2010,** *19,* 581-588.

(70) Nam, Y.; Sharratt, S.; Cha, G.; Ju, Y. S. Characterization and Modeling of the Heat Transfer Performance of Nanostructured Cu Micropost Wicks. *J Heat Transfer* **2011,** *133,* 101502.

---

(71) Taberna, P. L.; Mitra, S.; Pozot, P.; Simon, P.; Tarascon, J. -M. High rate capabilities Fe_3O_4-based Cu nano-architectured electrodes for lithium-ion battery applications. *Nature Mater.* **2006**, *5*, 567-573.

(72) Miao, T.; Wang, W.; Lee, S. H.; Lee, Y. C.; Yang, R. G. Enhancing Ni-Sn nanowire lithium-ion anode performance by tailoring active/inactive material interfaces. *J. Power Source* **2011**, *196*, 10207-10212.

(73) Quere, D. Wetting and roughness. *Annu. Rev. Mater. Res.* **2008,** *38*, 71-99.

(74) Chung, B. J.; Kim, M. C.; Ahmadinejad, M. Film-wise and drop-wise condensation of steam on short inclined plates. *J. Mech. Sci. Technol.* **2007,** *22,* 127-133.

(75) Glicksma.L. R.; Hunt, A. W. Numerical simulation of dropwise condensation. *Int. J. Heat Mass Trans.***1972,** *15*, 2251-2269.

(76) Rose, J. W., Dropwise condensation theory and experiment: a review. *P. I. Mech. Eng. A-J Pow.***2002,** *216*, 115-128.

(77) Kim, S.; Kim, K. J., Dropwise condensation modeling suitable for superhydrophobic surfaces. *J. Heat. Trans.-T. ASME***2011,** *133,* 081502.

(78) Miljkovic, N.;Enright, R.; Wang, E. N. Modeling and optimization of superhydrophobic condensation. *J. Heat Trans.***2013,** *135,* 111004-111018.

(79) Enright, R.; Miljkovic, N.; Al-Obeidi, A.; Thompson, C. V.; Wang, E. N. Condensation on superhydrophobic surfaces: the role of local energy barriers and structure length scale. *Langmuir* **2012,** *28,* 14424-14432.

(80) Toth, T.; Ferraro, D.; Chiarello, E.; Pierno, M.; Mistura, G.; Bissacco, G.; Semprebon, C. Suspension of water droplets on individual pillars. *Langmuir* **2011,** *27,* 4742-4748.

(81) Marmur, A. Wetting on hydrophobic Rougn Surfaces: To be heterogeneous or not to be? *Langmuir.* **2003,** *19*, 8343-8348.

(82) Chow, T. S. Wetting of rough surfaces. *J. Phys.: Condens Mat.* **1998,** *10,* L445-L451.

(83) Wang, F.; Yang, F.; Zhao, Y. Size effect on the coalescence-induced self-propelled droplets. *Appl. Phys. Lett.* **2011,** *98*, 053112.

(84) Rose, J. W. Further aspects of dropwise condensation theory. *Int. J. Heat Mass Trans.* **1976,** *19*, 1363-1370.

(85) Liu, T. Q.; Sun, W.; Sun, X. Y.; Ai, H. R. Mechanism study of condensed drops jumping on super-hydrophobic surfaces. *Colloids Surf. A* **2012,** *414*, 366-374.

---

(86) Stylianou, S. A.; Rose, J. W. Drop-To-Filmwise Condensation Transition: Heat Transfer Measurements for Ethanediol. *Int. J. Heat Mass Transfer,* **1983,** *26*, 747-760.

(87) Ishino, C., Reyssat, M., Reyssat, E., Okumura, K., Quere, D. Wicking within forests of micropillars. *Europhys. Lett.,* **2007.** *79*, 56005.

(88) Rioboo, R., Marengo, M., Tropea, C. Time evolution of liquid drop impact onto solid, dry surfaces. *Exp. Fluids* **2002,** *33*, 112-124.

(89) Son, Y., Kim, C., Yang, D. H. Ahn, D. J. Spreading of an inkjet droplet on a solid surface with a controlled contact angle at low weber and Reynolds numbers. *Langmuir,* **2008,** *24,* 2900-2907.

(90) Schiaffino, S., Sonin, A. A. Molten droplet deposition and solidification at low Weber numbers. *Phys. Fluids,* **1997,** *9,* 3172-3187.

(91) Li, C., Peterson, G. P. Parametric Study of Pool Boiling on Horizontal Highly Conductive Microporous Coated Surfaces. *J. Heat Transfer* **2007**, *129*, 1465-1475.

(92) Li, C.; Peterson, G. P. Evaporation/boiling in thin capillary wicks (I)—wick thickness effects. *J. Heat Transfer* **2006,** *128*, 1312-1319.

(93) Li, C.; Peterson, G. P. Evaporation/boiling in thin capillary wicks (II)—effects of volumetric porosity and mesh size. *J. Heat Transfer* **2006,** *128,* 1320-1328.

(94) Fan, J. –G.; Dyer, D.; Zhang, G.; Zhao, Y.-P. Nanocarpet effect: pattern formation during the wetting of vertically aligned nanorod arrays. *Nano. Lett.* **2004,** *4,* 2133-2138.

(95) Wang, C. H., Dhir, V. K. Effect of Surface Wettability on Active Nucleation Site Density During Pool Boiling of Water on a Vertical Surface. *J. Heat Transfer* **1993,** *115*, 659-669.

(96)Wang, C. H., Dhir, V. K. On the Gas Entrapment and Nucleation Site Density During Pool Boiling of Saturated Water. *J. Heat Transfer* **1993,** *115,* 670-679.

(97) Carey, V. P. *Liquid-Vapor Phase-Change Phenomena* Hemisphere: Washington, DC, 1992.

(98) Dhir, V. K. Mechanistic Prediction of Nucleate Boiling Heat Transfer--Achievable or a Hopeless Task? *J. Heat Transfer* **2006,** *128,* 1-12.

(99) Wei, J. J., Honda, H. Effects of fin geometry on boiling heat transfer from silicon chips with micro-pin-fins immersed in FC-72. *Int. J. Heat Mass Trans.* **2003,** *46,* 4059-4070.

(100) Bankoff, S. G.; mikesell, R. D. Bubble growth rates in highly subcooled nucleate boiling. *Chem. Eng. Prog. Symp. Ser.* **1959,** *55,* 95-102.

---

(101)Bankoff, S. G. Entrapment of Gas in the Spreading of a Liquid over a Rough Surface. *AIChE J.* **1958,** *4*, 24–26.

(102) Incropera, F. P., Dewitt, D. P., Bergman, T. L., Lavine, A. S. *Fundamentals of Heat and Mass Transfer 6th Edition*. John Wiley & Son: Hoboken, NJ, 2006.